UNIVERSIDADE DA BEIRA INTERIOR
Engenharia

Aerodynamic Breakup of a Single Droplet due to a Crossflow

(versão corrigida após defesa)

Gabriel Alexandre da Costa Carrolo

Dissertação para obtenção do Grau de Mestre em
Engenharia Aeronáutica
(Ciclo de estudos integrado)

Orientador: Prof. Doutor André Resende Rodrigues da Silva

Covilhã, Maio de 2019

Acknowledgements

Firstly, I would like to thank my supervisor Assistant Professor André Resende Rodrigues da Silva, for the opportunity given to develop the present work, the belief and mindfulness deposited on me when times seemed most dire and difficult. The availability to openly discuss the matters of this dissertation, whenever needed, was also one of the biggest motivations underlying this publication. Also, thanks to Full Professor Jorge Barata, for giving the opportunity of being a part of this big and great workgroup.

In addition, I would like to extend my deepest thanks to all colleagues and friends that worked by my side in the AEROG - Aeronautics and Astronautics Research Group facilities. To Inês Ferrão and Daniela Ribeiro, a special thanks for all the days spent in the lab tackling and overcoming every obstacle. To André Franco, for being a truly good friend when I needed the most, and Daniel Rodrigues and Cátia Moura for providing me with loads of good disposition and happiness. Not forgetting Leandro Magalhães, that proved to be a valuable colleague helping and suggesting all sorts of methods for the writing and presentation process.

To all my housemates, all the adventures and problems that lead our paths to intertwine were certainly not random. António Costa, Gonçalo Pacheco, Paulo Ferreira, Luís Reis, João Miguel, Hélder Gonçalves and Adriano Brum a big appreciation for shaping the friend and man I am today. A very special thanks to Luís Romeiro, for being the best of friends, and providing me with some of the best stories and adventures in my academic course.

Acknowledgement of LAETA's (Laboratório Associado de Transportes, Energia e Aeronáutica) chance provided in meeting various researchers and professors on the most wide range fields of study available in Portugal. Also thank Lab Technician Mr Rui Paulo for all the help, being a very important piece on the realization of my dissertation.

Thanks to all my family, especially my dad João Carrolo that provided the ability to follow this dream of mine. My grandparents that helped in every way possible, and I'm sure they'll happy for this milestone. To Paulo and Marco Alves, for the inspiration, and my uncles for nurturing, in every way possible, my future. The most important thanks will go to my sister, Raquel Carrolo. You did everything imaginable for me and I will carry every word, thought and action with me, for the rest of my life.

Lastly, but definitely not least: the most heart felt thank you to Filipa Leal Pereira. You helped me overcome some of the biggest obstacles and fears that I faced in my life, and for that, I am forever grateful. Not only that, but also work suggestions that proved to be successful. For all the happiness, love, caring and fun moments you provided, during all this time: Thank You, with all my heart.

Resumo

O presente trabalho experimental incide sobre o estudo do breakup aerodinâmico de combustíveis não convencionais. Este processo refere-se à atomização secundária de uma gota devido a um escoamento cruzado, onde diferentes velocidades deste provocam vários regimes e estruturas de deformação de uma gota de Jet Fuel e misturas deste com HVO (bio combustível vegetal hidro processado).

O uso excessivo de combustíveis fosseis levou o ser humano a encontrar alternativas viáveis e ambientalmente benéficas para o uso em variados tipos de motores e processos de combustão. Com isto, o uso de biocombustíveis tem sido uma das alternativas mais procuradas, e o seu uso no sector aeronáutico e aeroespacial é um exemplo da utilização benéfica destes combustíveis.

O objetivo desta dissertação é visualizar e estudar o comportamento dinâmico de uma gota nos pontos de transição entre regimes, para diferentes velocidades de escoamento cruzado. As gotas, são compostas por: Jet Fuel 100%, Jet Fuel 75% - 25% HVO, Jet Fuel 50% - 50% HVO e H_2O (usado como fluido de referência). Tendo em conta que a legislação em vigor no sector aeronáutico permite uma concentração mínima, de Jet Fuel, de 50% em volume faz com que a escolha das misturas usadas neste estudo tenha um critério mais restrito, e por isso outras misturas não são estudadas.

Para isto, uma instalação experimental foi projetada e construída. Constituída por uma camara de alta velocidade, permitindo a capacidade de visualizar todos os mecanismos inerentes à atomização secundaria de uma gota, acionada com um ”trigger” e com uma exposição e ”frame rate” específicos; uma bomba infusora, que permite o controlo da taxa de inserção de gotas na secção de trabalho através de agulhas de cabeça rasa com dois diâmetros internos diferentes, produzindo gotas do mesmo tamanho para todos os fluidos; retroiluminação através de tiras de led atras de um vidro difusor para uniformizar a luz captada pela camara; um túnel de vento devidamente calibrado para atingir as velocidades necessárias à transição dos respetivos regimes.

Utilizando a literatura existente, é feita uma comparação dos fenómenos e regimes de atomização secundária para este novo grupo de misturas utilizadas. Após o estudo dinâmico destes mecanismos foram tiradas as devidas conclusões quanto à taxa de deformação máxima de uma gota, tendo em conta a caracterização adimensional de tempo e os grupos adimensionais de relevância para este estudo. Foi também apresentada a trajetória das gotas para cada regime e fluido, e proposta uma correlação da evolução do diâmetro máximo quanto ao tempo.

Palavras-chave

Breakup aerodinâmico, Jet Fuel, Bio-combustível, Estudo Experimental, Combustão, Sprays, Escoamento Cruzado, Atomização Secundária

Abstract

The present experimental work focuses on the aerodynamic breakup study of unconventional fuels. This process refers to the secondary atomization of a drop due to a cross-flow, where different velocities cause several regimes and structures appear amidst drop deformation of Jet Fuel mixtures with HVO (hydroprocessed vegetable oil) and water.

The excessive use of fossil fuels has led humans to find viable and environmentally beneficial alternatives for use in various types of engines and combustion processes. With this, the use of biofuels has been one of the most sought after alternatives, and its employment in the aeronautical and aerospace sector is an example of the beneficial use of these fuels.

This dissertation's objective is to visualize and study the dynamic behaviour of a drop at the transition points between regimes, for different crossflow velocities. The drops are composed of: Jet Fuel 100%, Jet Fuel 75% - 25% HVO, Jet Fuel 50% - 50% HVO, and H_2O (used as reference fluid). Considering that present legislation in the aeronautical sector allows a minimum concentration of 50% Jet Fuel in volume makes the choice of mixtures used in this study have a more restricted criterion, and therefore other mixtures are not considered.

For this, an experimental facility is designed and built. Consisting of a high-speed camera, allowing the ability to visualize all the mechanisms inherent to the secondary atomization of a drop, with a specific trigger activation and desired frame rate; an infusion pump, which allows control of the insertion rate of drops into the working section. Through flat-head needles with two different internal diameters, drops of the same size are produced for all fluids; backlighting through led strips behind a diffuser glass help standardize the light captured by the camera; a properly calibrated wind-tunnel to is necessary to reach the desired speeds for regime transitions.

Using the existing literature, a comparison of the phenomena and secondary atomization regimes for this new group of mixtures is made. After the dynamic study of these mechanisms, the conclusions are drawn regarding the maximum deformation rate of a drop, taking into account the dimensionless characterization of time and the dimensionless groups of relevance for this study. Drop trajectory is also presented for each regime and fluid, and a new correlation is proposed for maximum cross stream diameter evolution due to time.

Keywords

Aerodynamic Breakup, Jet Fuel, Bio-Fuel, Experimental Study, Combstion, Sprays, Cross-Flow, Secondary Atomization

Contents

List of Figures

List of Tables

Nomenclature

C_{p_e}	Minimum wall velocity pressure coefficient
C_{p_i}	Maximum wall velocity pressure coefficient
d	Screen diameter
D_{eqe}	Tunnel inlet equivalent diameter
D_{eqi}	Tunnel outlet equivalent diameter
D_0	Initial droplet diameter
D_{max}	Maximum crossstream diameter of the deformed drop
f	Frequency
F_e	Non-dimensional parameter of minimum wall velocity
F_i	Non-dimensional parameter of maximum wall velocity
G_1	First guillotine
G_2	Second guillotine
Δh	Water height on manometer tube
Δh_{ref}	Reference water height on manometer tube
H_1	Tunnel's contraction inlet height
H_2	Tunnel's contraction outlet height
K	Pressure drop coefficient
L	Screen Length
L_T	Total Nozzle Length
Oh	Ohnesorge number
t	Time
$t*$	Characteristic breakup time
$\tilde{u}_2$	Exit velocity non-uniformity
U_r	Relative velocity between droplet and gas in the main flow direction
U_c	Crossflow velocity
U_{d_x}	Drop velocity component in the stream direction
U_{d_y}	Drop velocity component in the cross-stream direction
$U_{\infty,1}$	Tunnel's contraction inlet velocity
$U_{\infty,2}$	Tunnel's contraction outlet velocity
w	Contraction's nozzle width
We	Weber number
$\mathrm{We}_{\mathrm{cr}}$	Critical Weber number
x_0	Distance from virtual origin of a boundary layer to nozzle exit
x_i	Axial coordinate for maximum wall velocity
X	Contraction match point
Z_t	Nozzle point of measurement

Greek Symbols

ε	Non-dimensional characterization of the maximum cross-stream diameter (D_{max}/D_0)
μ	Dynamic viscosity
ν	Kinematic Viscosity
ρ	Density
σ	Surface tension
τ	Non-dimensional characterization of time
τ_{ini}	Non-dimensional characterization of time for the initiation of breakup
τ_{tot}	Non-dimensional characterization of time for total breakup

Acronyms

AC	Alternated Current
CR	Contraction Ratio
DDB	Droplet Deformation and Breakup
DNS	Direct Numerical Simulation
ETAB	Enhanced Taylor Analogy Breakup
fps	Frames per second
HEFA	Hydro-processed Esters and Fatty Acids
HVO	Hydro-processed Vegetable Oil
LED	Light Emitting Diode
NEXBTL	Next Generation Biomass-to-Liquid
TAB	Taylor Analogy Breakup
VOF	Volume of Fluid

Chapter 1

Introduction

The study of motion, deformation and breakup of a single droplet due to a cross-flowed air stream has a big significance for application in many engineering and industrial purposes. As known, combustion efficiency depends mostly on the atomization of fuel droplets produced by spray mechanisms. Therefore, the study of breakup mechanisms and their governing parameters is important. The efficiency of these combustion systems is also a way to reduce fossil fuel emissions from exhaust gases.

Since many of the studies focus on the breakup of water, glycerine mixtures and common diesel droplets, the behaviour of jet fuel mixtures for conditions similar to the present set-up was not found. Albeit, this chapter presents the motivation and objectives underlying the development of the present work, followed by a concise contextualization of other authors' findings.

1.1 Motivation

The increasing use of fossil fuels is leading to their rapid extinction, forcing the human being to adapt and find alternative ways to reduce their usage. In addition, these mixtures are one of the most significant sources of pollution known to man, so the introduction of biofuel in conventional aircraft fuels may have a positive impact on emission reduction.

Current legislation allows the mixture of conventional Jet Fuel with HEFA (Hydroprocessed Esters and Fatty Acids) type alternative fuels. This creates an Alternative Jet Fuel (AJF) which is the final mixture between the usual Jet A-1 with conventional and synthetic blending components (hydrocarbons). This legislation - ASTM D1655 & ASTM D7566 [1–3]- also places a maximum blending ratio of 50% of the alternative fuels, so the present work contains mixtures with a maximum of 50% Biofuel. With this consideration, the fuels utilized can be used in any aircraft nowadays. The biofuel chosen is an Hydro-processed Vegetable Oil (HVO) that is a HEFA type fuel where no animal biomass is involved [3].

The next section will explore the available literature from the governing parameters to breakup mechanisms, and will present thresholds for the study of droplet secondary atomization that are a major guideline for this works' development. Experimental and analytical results will be analysed in order to determine the existence of differences between proposed correlations and the results obtained in this work using a new set of test fluids.

1.2 Objectives

As said, the use of various fluids for the study of secondary atomization on drops with low viscosity is found within the available literature, yet the use of conventional turbine fuels such as Jet A-1, a kerosene-based commercial type of fuel, is not found. Furthermore, the use of these mixed with biofuel is also relevant, as mankind is searching for new and sustainable ways to reduce pollutant emissions.

The main objective is to study the behaviour of small droplets using these fluids when exposed to a crossflow to induce secondary atomization. As known, for different flow velocities various regimes appear and have been clearly identified for other conventional fluids. A new set of mixtures is used to compare results and visualization using the aforementioned fluids. Moreover, image treatment and characterization is done so drop diameter, centroid and velocity can be calculated, enabling the calculation of relevant non-dimensional groups (Weber, Ohnesorge and Reynolds number) and verification of correlations proposed by other others for a variety of regimes. Time intervals at which important structures or atomization events are found are also important to assess the fluid properties' influence on the appearance of such structures. Finally, drop trajectory is determined until the first signs of secondary atomization, as experimental results containing this data was not found.

Once the work is complete, a conclusion can be extracted on whether Jet A-1 and NEXTBTL biofuel behave similarly to other fluids or not. This work will also use water as a reference fluid due to its well known properties. Criteria proposed by a variety of authors along the years is used as comparison models to plot the results obtained.

1.3 Work Structure

The present dissertation is composed of 5 chapters, including the present one providing an overview of the general work order. After the objectives are set, fundamental information is presented in the literature review that is the base of this work and a contextualization of the work done until this point.

In Chapter 2 the relevant non-dimensional groups are introduced and their physical meaning is explained, and the various methods for flow creation of induction are presented since these will directly affect these groups. Time characterization and normalization is found in most studies, while also being influenced by Weber and Ohnesorge numbers. Finally in the review section, drop characterization and regime appearance is thoroughly explained.

Chapter 3 describes the experimental facility. All the components that able the study of drop secondary atomization are presented such as wind tunnel, drop diffuser and image capture, back-lighting and fuel properties.

Results and discussion can be found thoroughly presented in Chapter 4, where the correlations found in the literature are plotted against the obtained results and compared, taking into account the use of different fluids. All the measurements and calculations done in this dissertation are based on other authors propositions for error mitigation and proximity in results.

The final chapter will be a summary of conclusions and proposed future works. The most important considerations are presented suggesting future improvements on the experimental facility and work methodology.

Chapter 2

Literature Review

The aerodynamic breakup of a drop, due to a cross-flowed air stream, is reported in the literature for various flow speeds, mixtures and simple fluids with different properties and using various drop generators, implying a wide variety of diameters. All these parameters have a big impact on the disintegration process of a droplet. Moreover, many authors have presented various thresholds for regime transitions.

The following subsections will thoroughly explain the breakup regimes, as well as its transitions. These will be defined with aid of dimensionless equations presented in the literature, essential for the study of droplet motion in general. This review has its focus on the experimental studies conducted throughout the years. Numerical studies are also relevant for comparison of empirical correlations with the experimental results.

2.1 Droplet Motion Governing Parameters

With the presence of a crossflow the drop experiences since its formation and until secondary atomization is complete, various stages of pressure and velocity gradients which influence its motion and shape. A study of each individual property is hard and time-consuming, so there is a need to group them into dimensionless numbers that simplify the characterization of the drops" motion or deformation. Ref. [4] describes the Weber number - Eq. 2.1 - as the ratio between the inertial forces to surface tension energy, i.e., the relation between the droplet kinetic energy and surface energy:

$$\mathrm{We} = \frac{\rho_g D_0 U_r^2}{\sigma} \quad (2.1)$$

where ρ is the density of the surrounding air, D_0 is the initial drop diameter, U_r is the initial relative velocity between drop and gas in the main flow direction, and σ is the surface tension of the fluid. The Ohnesorge number - Eq. 2.2 - describes the ratio of viscous forces with inertial and surface tension forces:

$$\mathrm{Oh} = \frac{\mu_l}{\sqrt{\rho_l \sigma D_0}} \quad (2.2)$$

with μ being the dynamic viscosity of the fluid. As seen in Eq. 2.2, the Ohnesorge number can be equated relating the Weber and Reynolds numbers - Eq. 2.3 - the ratio between the inertial and viscous forces.

$$\mathrm{Re} = \frac{\rho_g D_0 U_r}{\mu_g} \quad (2.3)$$

When the drop enters a cross-flowed air stream the appearance of aerodynamic resistance forces influence its shape and behaviour [5]. A relation between deformation and drag is needed to determine acceleration, and three main factors that affect overall drag are identified in the literature as geometry, internal circulation and unsteady effects; it is generally assumed that the unsteady effects are negligible. Ref. [6] found that the instantaneous drag coefficient can be approximated by linear interpolation to that of a solid sphere or a disk-like object at equal Reynolds number, meaning that internal circulation effects are minimal.

All these parameters with the aid of drag coefficient values help understand the deformation rate of the droplet that leads to the various regimes. In the next subsection these mechanisms will be explained to better understand the influences of the cross-flow on drop atomization.

2.2 Flow Field

For the study of secondary atomization, various methods enable the induction of a flow field capable of disrupting the droplet to the point of disintegration. Each method differs by the type of aerodynamic loading on the drop.

Firstly, the shock tube experiment provides a uniform step change in relative velocity, with pressurized gas being released into a driven section, developing a shock-wave throughout the tube, Figure 2.1. In a very basic and generalist approach the shock tube experiments consist in a high pressure driver gas retained by a diaphragm that, upon opening, is released creating a shock wave. The gas is compressed and heated to combustion temperatures throughout and the deformation and breakup events can be seen in the observation window.

The shock itself causes minimal to no deformation to the drop, yet the flow behind it eventually leads to breakup. Despite producing a uniform step change when interacting with the drop, the need to reset the experiment after each measurement leads to a low data acquisition rate. In addition, in practical purposes, it rarely experiences these conditions [5–9].

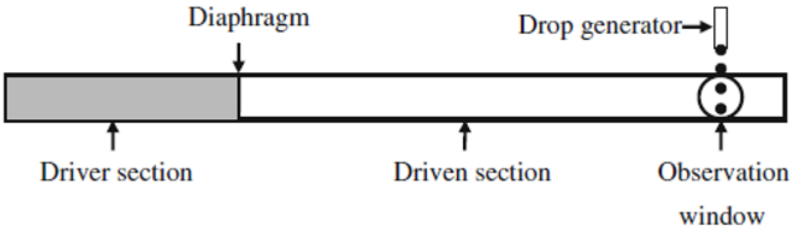

Figure 2.1: Shock tube experiment diagram, adapted from [5].

Secondly, the continuous jet experiments provide a simple and easy to operate experimental set-up with the ability to operate continuously. The nozzle shape is projected to minimize the boundary layer thickness, and to achieve a uniform velocity profile in order to ensure the drop does not experience different velocity gradients in the test sections, Figure 2.2.

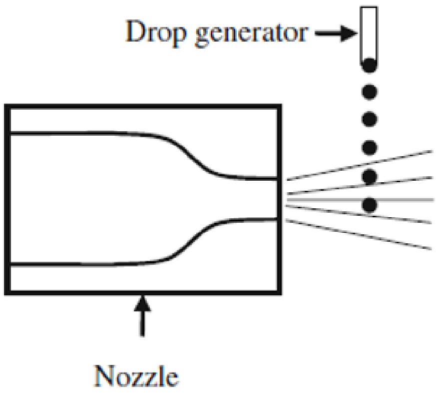

Figure 2.2: Continuous jet diagram, adapted from [5].

Two conditions must be satisfied for this apparatus to be correctly used and provide acceptable results: the time required for the drop to breakup must be low enough for the phenomena to occur in the flow field; the time required for the drop to surpass the boundary layer must be less than the time of initiation of breakup [10].

Finally, the drop tower technique takes advantage of gravity acceleration, with the drops' velocity being slowly incremented. This method is mostly used in atmospheric sciences since the time for total breakup is much higher.

2.3 Breakup Timescale

As for all of the studies that have motion implied, time is of much importance for the breakup phenomena and to comprehend the relation between flow speed and the drop disintegration processes. One can easily say that with flow speed increase, the time needed to fully develop disintegration processes decreases. Yet, for each regime different structures are created and the time needed to complete the secondary atomization might not be the same.

This time-scale is divided into 2 sections: breakup initiation time and total breakup time. The former represents the time needed for each drop to exceed a maximum diameter point and exhibit the creation of breakup structures. For example, in the Bag Breakup regime case this would be the time when the drop demonstrates the first signs of the bag formation. As opposed to this, the total breakup time is when the drop no longer undergoes further atomization, and this time is when the secondary atomization comes to a halt, Figure 2.3.

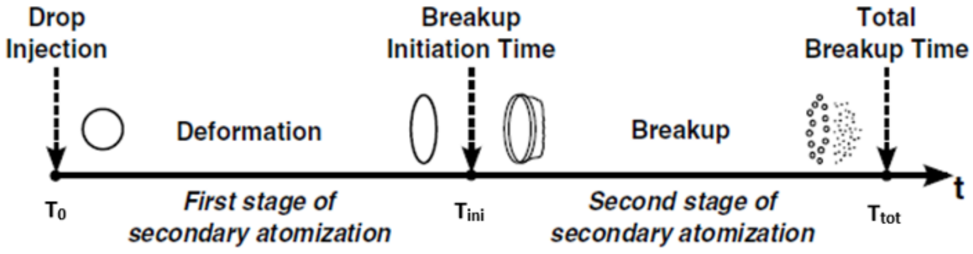

Figure 2.3: Schematic of the timescales involved in the secondary atomization, adapted from [11].

The time intervals, t, present in the study of breakup mechanisms are very small and a characteristic breakup time, t^*, is used to normalize it. This characteristic time takes advantage of the drops' properties and flow speed.

$$t^* = \frac{D_0\left(\frac{\rho_l}{\rho_g}\right)^{0.5}}{U_r} \quad (2.4)$$

$$\tau = \frac{t}{t^*} = \frac{tU_r}{d_0\left(\frac{\rho_l}{\rho_g}\right)^{0.5}} \quad (2.5)$$

For low Ohnesorge numbers, Gel'fand et al. [12], Pilch and Erdman [13] and Hsiang and Faeth [6], found an agreement in breakup initiation at $1.5 < \tau_{\text{ini}} < 2$ using Eqs. 2.6, 2.7 and 2.8 respectively. All three describe a roughly constant variation until $\text{Oh} \approx 0.5$. Further beyond this point the correlations show a steep increase, because of increasing influence of viscosity, and a subsequent distancing between all three and does not show agreement, Figure 2.4a.

$$\tau_{ini} = 1.9(\text{We} - 12)^{-0.25}(1 + 2.2\text{Oh}^{1.6}) \quad (2.6)$$

$$\tau_{ini} = \frac{1.6}{1 - \left(\frac{\text{Oh}}{7}\right)} \quad \text{We} < 10^3, \quad \text{Oh} < 3.5 \quad (2.7)$$

$$\tau_{ini} = 1.4(1 + 1.5\text{Oh}^{0.74}) \quad \text{We} \approx \text{We}_\text{c}, \quad \text{Oh} < 4.0 \quad (2.8)$$

As for the total breakup time the same authors state that $\tau_{\text{tot}} \approx 5.0$ is a reasonable compromise, with the same steep increase being shown, yet beyond higher Oh values. Refs. [6, 12] propose Eq. 2.9 and 2.10 respectively, and these correlations are illustrated in Figure 2.4b.

$$\tau_{tot} = \frac{5}{1 - \left(\frac{Oh}{7}\right)} \quad \text{We} < 10^3, \quad Oh < 3.5 \quad (2.9)$$

$$\tau_{tot} = 4.5(1 + 1.2\text{Oh}^{0.74}) \quad \text{We} \approx \text{We}_\text{c}, \quad \text{Oh} < 0.3 \quad (2.10)$$

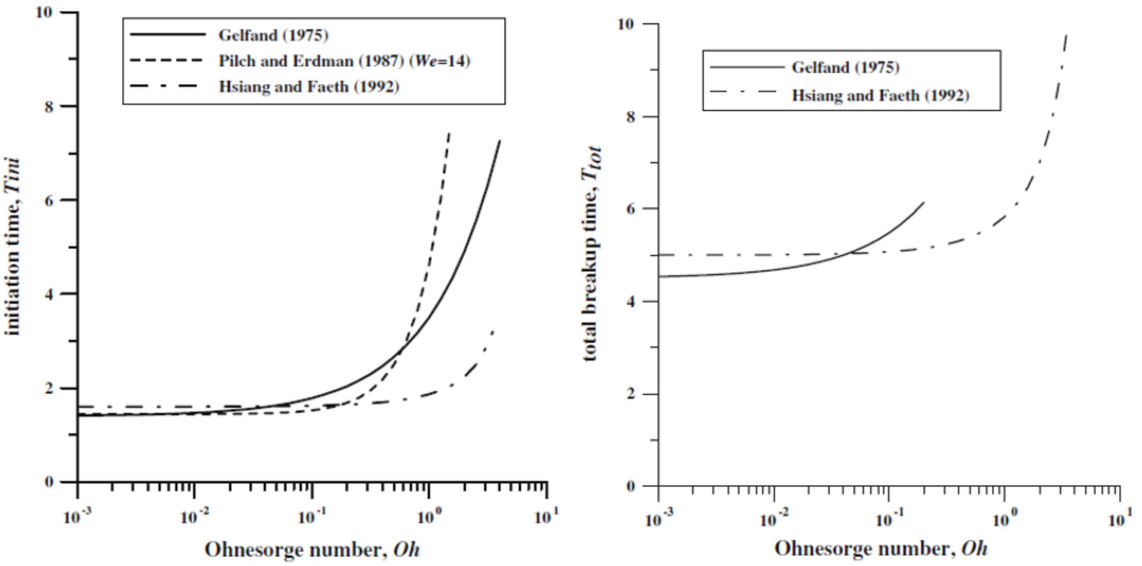

(a) (b)

Figure 2.4: Initiation and Total Breakup times plotted against Oh number, from [5].

For breakup initiation and total times with high Ohnesorge number values, the literature is unable to produce an agreeable correlation for the breakup initiation and total times, and a steep increase is seen in both cases. When plotting initiation and total breakup times against We number, the evidence of an initiation time reduction with the increase of We is seen. Initiation time continues to further decrease as the flow speed and consequently Weber number increase, which is an acceptable compromise [13]. This can be described by means of Eq. 2.6, yet this time varying the Weber number and using the condition of $\mathrm{Oh} < 0.1$, Figure 2.5. Beyond all these comprehensive correlations, the total breakup time shows a very erratic variation with We increase, Eq. 2.11. The same author proposed these equations for the experimental data available and regimes encountered, Figure 2.5. The ranges chosen will be explained due to regime changes and differences, later in this review.

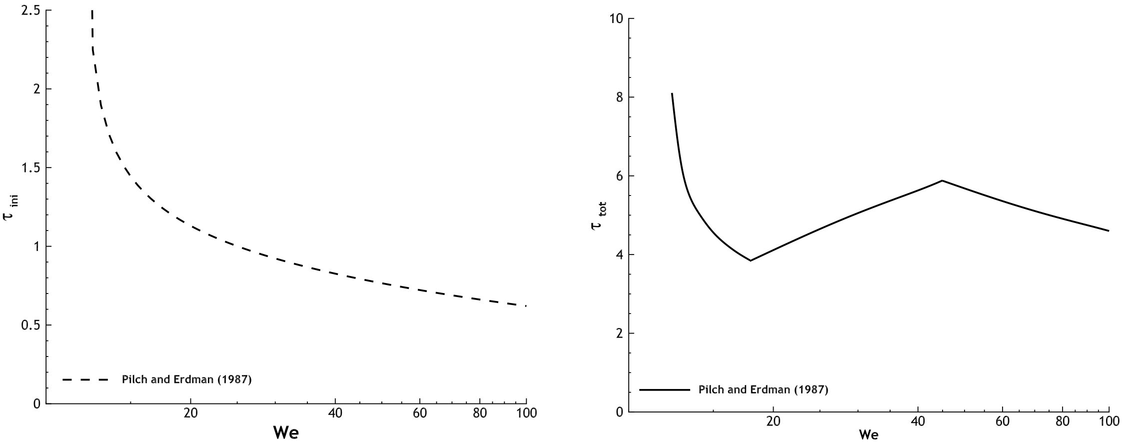

(a) (b)

Figure 2.5: Initiation and Total Breakup times plotted against We - Eqs. 2.6 and 2.11 [13].

$$\tau = \begin{cases} 6(\mathrm{We}-12)^{-0.25}, & 12 < \mathrm{We} \leqslant 18 \\ 2.45(\mathrm{We}-12)^{0.25}, & 18 \leqslant \mathrm{We} \leqslant 45 \\ 14.1(\mathrm{We}-12)^{-0.25}, & 45 \leqslant \mathrm{We} \leqslant 351 \end{cases} \quad (2.11)$$

2.4 Drop Deformation and Trajectory

As the drop enters the flow, due to aerodynamic forces the interaction between liquid and gaseous phase gives way to the earliest stage of secondary atomization: deformation. The continuous jet deforms the droplet into an oblate ellipsoid, Figure 2.6. The unequal static pressure distribution over the drops' surface is responsible for this deformation, where both the rear and forward stagnation points of the drop are at a higher pressure than the rest of the surrounding flow.

For simplification purposes, and using known nomenclature, this deformation ratio, i. e. the ratio between maximum and initial cross stream diameter is henceforth given by $\varepsilon = D_{max}/D_0$. Regardless of the drops real size, when normalized by its initial diameter it produces a more generalized view of the deformation behaviour.

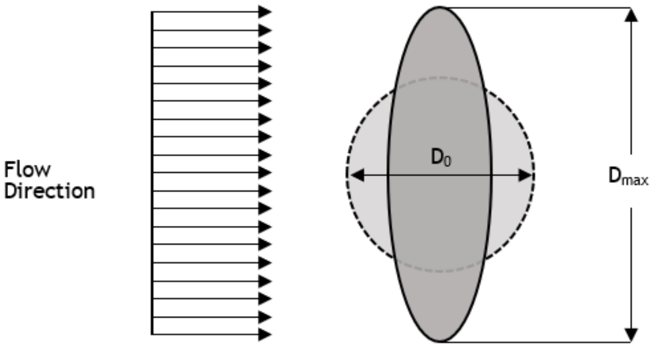

Figure 2.6: Droplet deformation diagram, adapted from [14].

Ref. [6] conducted a series of experimental data analysis considering the forces applied to the drop and stated that, for all regimes, ε fits reasonably well with a linear increase equation when plotted against We, Eq. 2.12.

$$\varepsilon = 1 + 0.19\mathrm{We}^{0.5}, \quad 20 < \mathrm{We} < 80 \quad (2.12)$$

Refs. [15, 16] propose an extension of this matter presenting correlations for a wider range of We number, Eq. 2.13 and 2.14 respectively. Ultimately, when the regimes that lead to secondary atomization start to appear, both these propositions imply a state of stagnation in diameter increase, Figure 2.7a.

$$\varepsilon = 2.2, \quad 20 < \mathrm{We} < 80 \quad (2.13)$$

$$\varepsilon = \frac{2}{1+\exp(-0.0019\mathrm{We}^{2.7})}, \quad 10 < \mathrm{We} < 80 \quad (2.14)$$

When plotting against Oh, the literature proposes a constant threshold, $\varepsilon = 1.75$, where the bag regime starts to occur, e. g. bellow this transition line the maximum diameter of the drops correspond to the Deformation stage, while above there is the visualization of Bag regime occurences [17]. As for other regimes, to the best of the author's knowledge, correlations are not found in the literature, Figure 2.7.

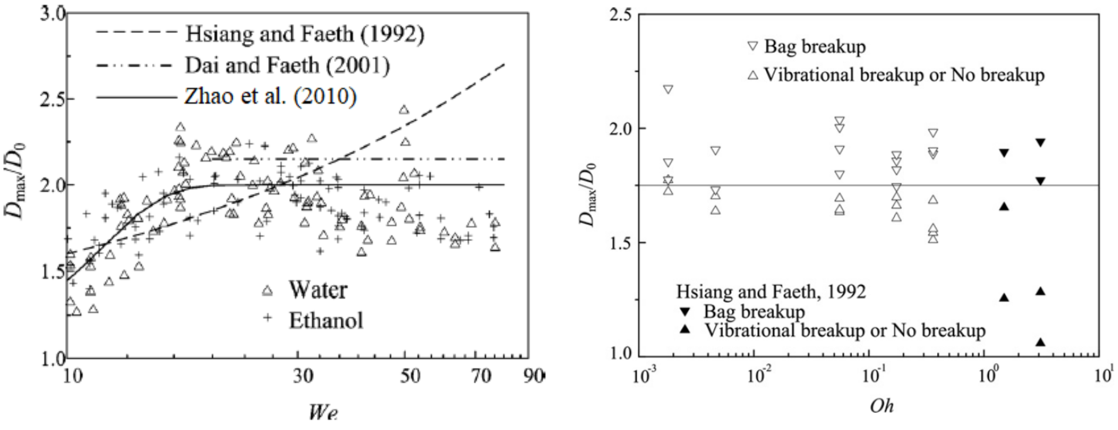

(a) (b)

Figure 2.7: Influence of We and Oh on maximum cross stream diameter [17].

As the aerodynamic loading on the drop is continuous, some authors propose taking into account a temporal evolution of the droplets diameter variation, contrary to [7]. Albeit, these propositions are for specific regimes. Ref. [18] found that for the dual-bag regime deformation should yield Eq. 2.15, while for the bag-plume regime, Ref. [19] proposes Eq. 2.16, Figure 2.8.

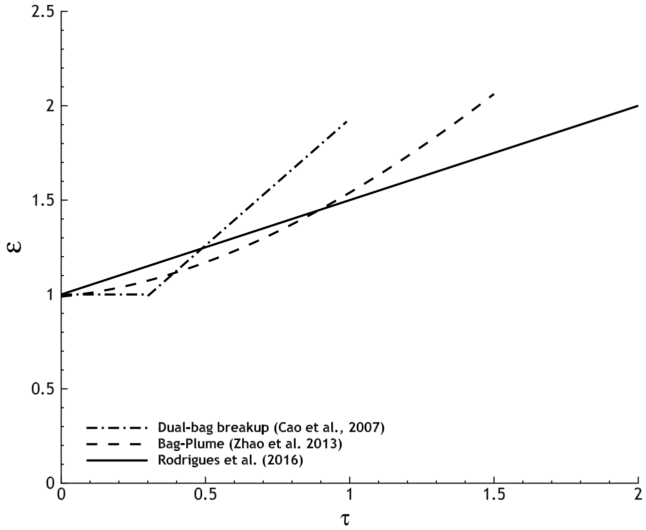

Figure 2.8: Time dependent variation of the maximum cross stream diameter [11, 18, 19].

$$\varepsilon = \begin{cases} 1, & 0 < \tau < 0.30 \\ 0.59 + 1.34\tau, & 0.3 < \tau < 0.99 \end{cases} \quad (2.15)$$

$$\varepsilon = 1 + 0.54\tau^{1.67}, \quad 0 \leqslant \tau \leqslant 1.5 \quad (2.16)$$

Throughout the years the literature presents the droplet trajectory mostly from computational analysis of numerous drops. Very few studies were found to measure the drops trajectories experimentally, nonetheless, it is an important characterization because of the cross-flows' influence.

Ref. [20] compared various computational predicted trajectories and superimposed these on images taken with high-speed cameras. As an example, Figure 2.9 is a representation of the predicted trajectory using a Taylor Analogy Breakup (TAB), deformation based, wave breakup and ref. [21] models compared with the experimental images captured by the author.

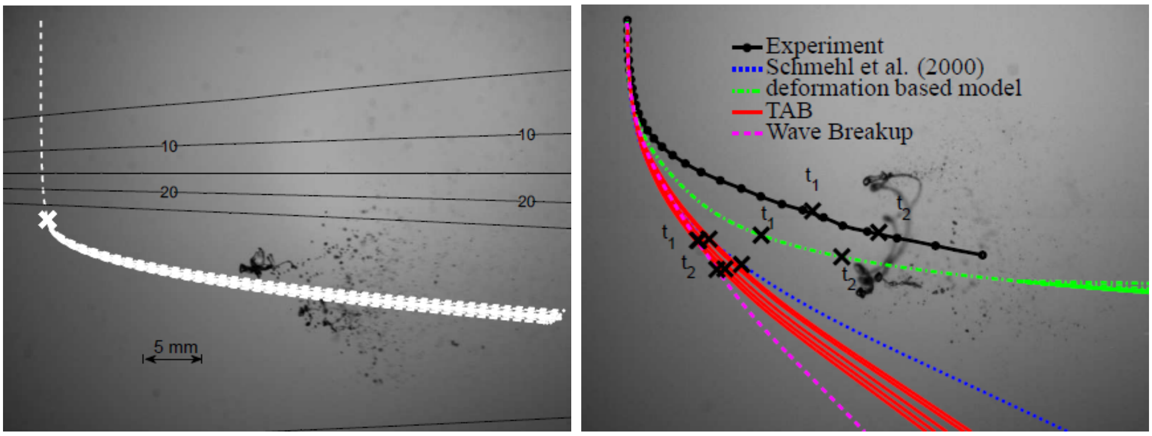

(a) (b)

Figure 2.9: Superposition of computationally predicted deformation and fragmentation process on high-speed camera images [22].

The authors conclude that the initial trajectory during deformation is an important prediction that can be achieved with computational models. Furthermore, the TAB and Deformation based models, that will be explained in later in this chapter, assume the drop as a spheroid enabling a much easier determination of the drag coefficient. Despite assuming the spheroid shape, the maximum cross stream diameter still continues to increase influencing drag even more. It is also stated that breakup times are the main feature in the deformation based and Schmehl et al. [21] models, yet there can be an overestimation of the critical Weber number that must be exceeded, leading to deviations in the trajectories prediction. In some cases, drops experienced secondary atomization even before reaching the stipulated breakup time or exceeding critical deformation. Regardless, all models show some inaccurate trajectory predictions in big velocity gradients or turbulent flows.

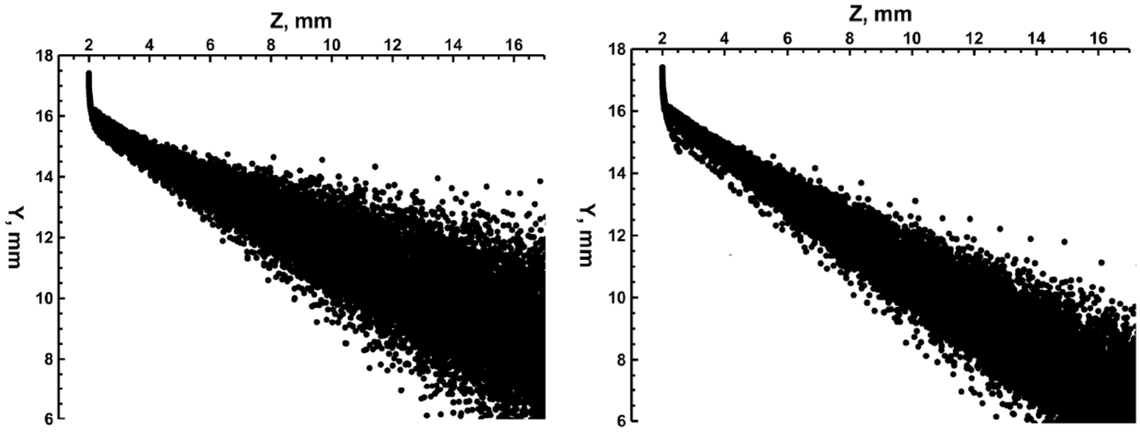

(a) Diesel

(b) Bio-diesel

Figure 2.10: Spray shape and evolution of 1000 drops (taken from [11]).

Ref. [11] present the spray shape and evolution of diesel and biodiesel drops, using an "*in-house*" developed model, Figure 2.10. This model base on experimental consideration is explained later on, yet the trajectory shape seems concordant with the ones predicted before.

2.5 Regime Transition Weber numbers

The variation of relative velocity influences We number's value, thus promoting a change in the breakup mechanisms. Moreover, most of the literature considers $\mathrm{Oh} < 0.1$ implying a state of low viscosity. The average limits of the Weber number for each regime were firstly proposed by [6], except for the shear and catastrophic regimes, later proposed by [13] as shown in Table 1.

Table 2.1: Breakup regimes - Transition We for Newtonian drops with Oh < 0.1.

Regimes	Range
Deformation	$0 < \mathrm{We} < 12$
Bag	$12 < \mathrm{We} < 35$
Multimode	$35 < \mathrm{We} < 80$
Shear	$80 < \mathrm{We} < 350$

It is of paramount importance to refer that, although the fluids used are generally water, n-heptane, glycerine mixtures and ethyl alcohol that vary in density, surface tension, and dynamic viscosity, the transition Weber numbers seems to be approximately the same for all fluids. Taking this into consideration, the regime transition is an important threshold and the point where different structures start to appear, that differ from earlier regimes. It is also seen that within the range of each regime, no significant differences rise from each We variation, thus the assumption that each of these remains unaltered within its range of appearance.

As seen, Table 2.2, throughout the years, different thresholds are proposed for each regime. Authors have come to a certain agreement in this matter, and the use of Dai and Faeth's and Cao et al. [15, 18] limits, is the most common division of regimes due to We variation. One can also notice a slow discrimination of each regime over time, with more definitions being proposed allocating each structure to a slightly defined range, with special attention needed for the division of the Multimode regime into Bag-Plume and Shear-Plume regimes. With this, the adopted thresholds are those of refs. [15, 18] as Table 2.3 illustrates. The shear later gives way to the catastrophic regime, yet as will be explained further in the next subsection, it is not taken into account.

Table 2.2: Transitional Weber numbers found throughout the literature review for Newtonian drops with $\mathrm{Oh} < 0.1$. Table adapted from Kékesi et al. [23].

<table>
<tr><td>Cao et al.
Ref. [18]</td><td colspan="5"></td><td colspan="4">Dual-Bag breakup</td><td colspan="5"></td></tr>
<tr><td>Dai and Faeth
Ref. [15]</td><td colspan="2"></td><td colspan="2">Bag breakup</td><td colspan="4">Bag-Plume breakup</td><td colspan="4">Plume-Shear breakup</td><td colspan="2"></td></tr>
<tr><td>Hsiang, Faeth et al
Refs. [6]-[9]</td><td colspan="2"></td><td colspan="5">Bag breakup</td><td colspan="5">Multimode breakup</td><td colspan="2">Shear breakup</td></tr>
<tr><td>Pilch and Erdman
Ref. [13]</td><td></td><td colspan="9">Bag breakup</td><td colspan="3">Bag-Plume breakup</td><td>Sheet Stripping breakup</td></tr>
<tr><td>Krzeczkowski
Ref. [24]</td><td colspan="4">Bag mechanism</td><td colspan="2">Bag-Plume mechanism</td><td colspan="5">Transition mechanism</td><td colspan="3">Shear/Mass Stripping mechanism</td></tr>
<tr><td rowspan="2"></td><td>10</td><td>12</td><td>13</td><td>15</td><td>18</td><td>28</td><td>30</td><td>35</td><td>40</td><td>41</td><td>50</td><td>63</td><td>80</td><td>100</td></tr>
<tr><td colspan="14">Weber number</td></tr>
</table>

Table 2.3: Transition We, for Newtonian drops, with Oh < 0.1.

Regime	Range
Bag	$12 < \mathrm{We} < 18$
Bag-Plume	$18 < \mathrm{We} < 40$
Shear-Plume	$40 < \mathrm{We} < 80$
Shear	$80 < \mathrm{We} < 350$

This section is important in the analysis of the total breakup time, τ_{tot}. For [6] the bag-plume breakup only appeared for $\mathrm{We} > 40$, as for further works it was seen to occur for $\mathrm{We} > 20$, approximately. This can affect the interpretation of the results and will be accounted for in Chapter 4.

The present work will be the characterization of each regime's first appearance, and the ranges proposed in the literature not only allow an easier search for each of these, but also the comparison from present findings and past results. Once the thresholds are roughly defined, the description of each regime is required and will be done in the next section.

2.6 Breakup Mechanisms

The interval $0 < \mathrm{We} < 12$ is named Vibrational Breakup [6], Figure 2.11. Secondary atomization during this period is not always observed, henceforth this stage will be referred to as Deformation. If the drop oscillates further from its natural frequency it will disintegrate and the drops resulting from this are not as small as for other regimes [25].

Ref. [7] qualitatively described the bag breakup. Divided into four stages, it starts when the aerodynamic forces deform the drop into a disk-like shape (oblate spheroid), the centre of the drop then expands creating a thin bag-like hollow structure attached to a ring of liquid, referred as the toroidal ring; after the deformation phases, breakup proceeds, with the bag structure being the first to experience secondary atomization into a large number of small fragments, followed by the toroidal rings' atomization into a small number of large fragments, Figure 2.12.

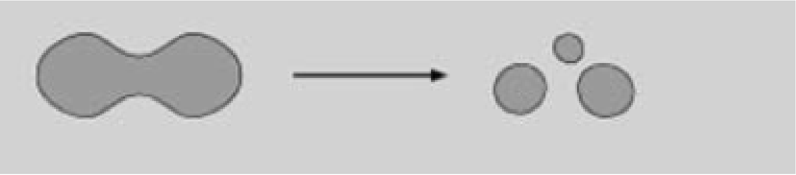

Figure 2.11: Vibrational breakup / Deformation schematics, adapted from [25].

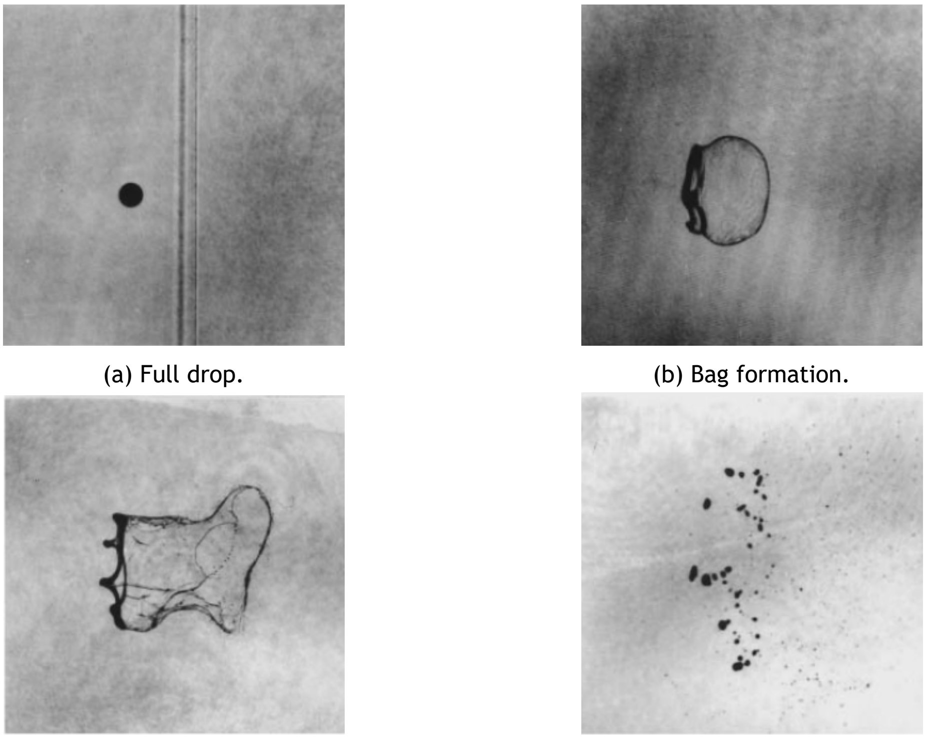

(a) Full drop.

(b) Bag formation.

(c) Bag's secondary atomization.

(d) Toroidal ring atomization.

Figure 2.12: Illustration of typical Bag breakup regime occurrence for low Ohnesorge number drops [15].

The term Multimode is due to several different denominations proposed in the literature by other authors, and so the use of multimode is considered as more extensive [6]. It is also considered to be a transitional stage of secondary atomization. Later others divided the multimode breakup regime into "bag-plume" and "shear-plume", where the former is similar to the bag regime yet there is the formation of a liquid filament within the bag structure [15], Figure 2.13. The latter differs from the bag-plume regime as the bag is not always formed, Figure 2.14. The authors also proposed We transitions ($18 < \mathrm{We} < 40$ for bag-plume and $40 < \mathrm{We} < 80$), highlighting that transition processes are continuous, and it is not possible to strictly define a transition We number, because of the overlap with the bag breakup transition regime [5].

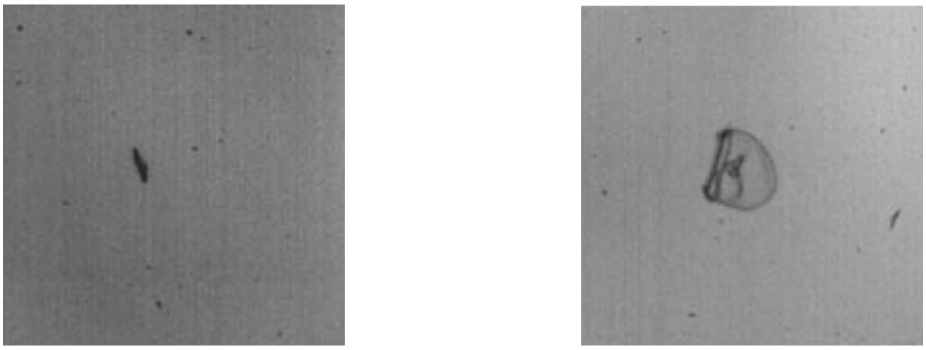

(a) Disk shaped drop. (b) Bag and plume formation.

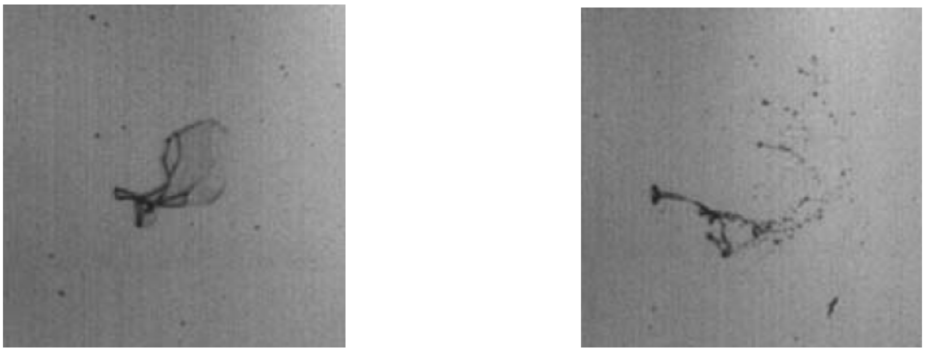

(c) Bag structure atomization. (d) Plume atomization.

Figure 2.13: Illustration of typical Bag-Plume breakup regime occurrence for low Ohnesorge number drops [5].

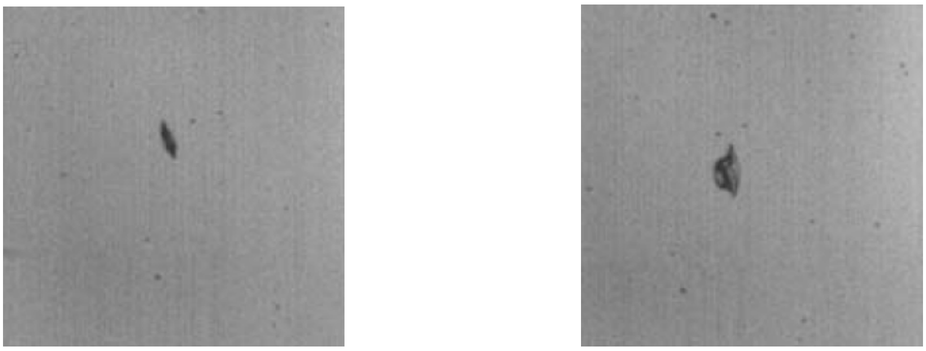

(a) Disk shaped drop. (b) Shearing effect.

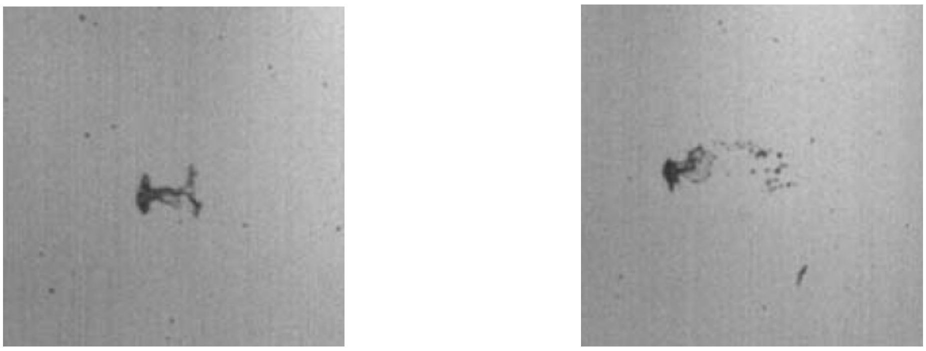

(c) Plume formation. (d) Plume atomization.

Figure 2.14: Illustration of typical Shear-Plume breakup regime occurrence for low Ohnesorge number drops [5].

Furthermore, Cao et al. [18] identified and proposed a new breakup regime, for the same uniform and continuous flow conditions, Figure 2.15. The Dual-Bag breakup was identified by the authors in the range $28 < \mathrm{We} < 41$ and is characterized by the existence of two separate bag formations. The main drop experiences this bag formation, yet the plume is still present. Afterwards, the plume-like structure deforms creating the second bag formation. The time stamps present in the images are merely a chronological information of the structures appearance.

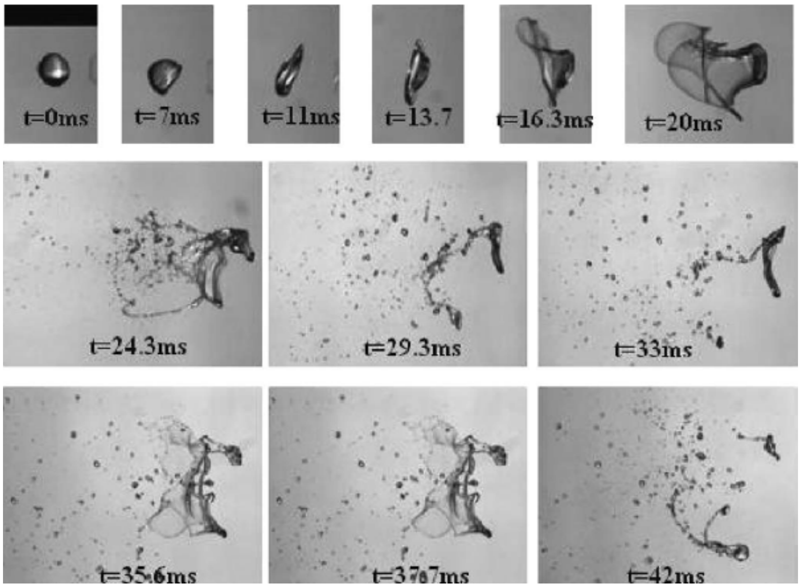

Figure 2.15: Illustration of typical Dual-Bag breakup regime occurrence for low Ohnesorge number drops [18].

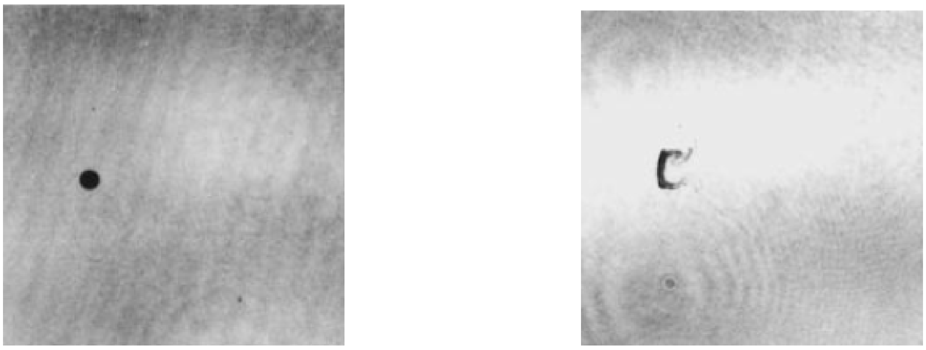

(a) Full drop.

(b) Shearing effect.

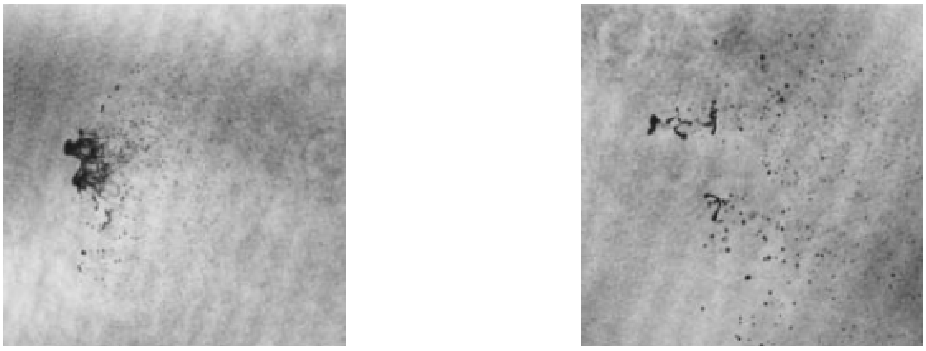

(c) Subsequent shearing.

(d) Fully atomized drop.

Figure 2.16: Illustration of typical Shear breakup regime occurrence for low Ohnesorge number drops [15].

At much higher velocities, the shear breakup regime ensues, [26]. Shear forces from the surrounding flow over the deformed drop form a boundary layer inside its surface, becoming unstable at the periphery and resulting in stripping of mass. Chou et al. [7] noted that drop viscosity increases fragment sizes in shock tube experiments for this regime.

Catastrophic breakup regime sometimes produces liquid fragments that cannot be coupled as drops because of the large number of filaments, depending also in the experiment, hence the name assigned to it, and because of this the catastrophic breakup regime is not considered. Faeth et al. [27] also noted that the velocities and drop sizes involved in typical dense sprays are such that catastrophic breakup is not identified.

The regimes illustrated above are the aim of the current study because of their relevance and application in dense sprays and combustion systems. These were identified for simple fluids, mixtures of glycerine, diesel and bio-diesel. It is known that the surface tension of Jet A-1 fuel is much smaller than these fluids, raising the question of whether they are the same and if there is any shift of the transitional Weber number. Figure 2.17 is an illustration of the transition thresholds presented in the latter subsection and proposed by [9, 28], when accounting Ohnesorge number variation.

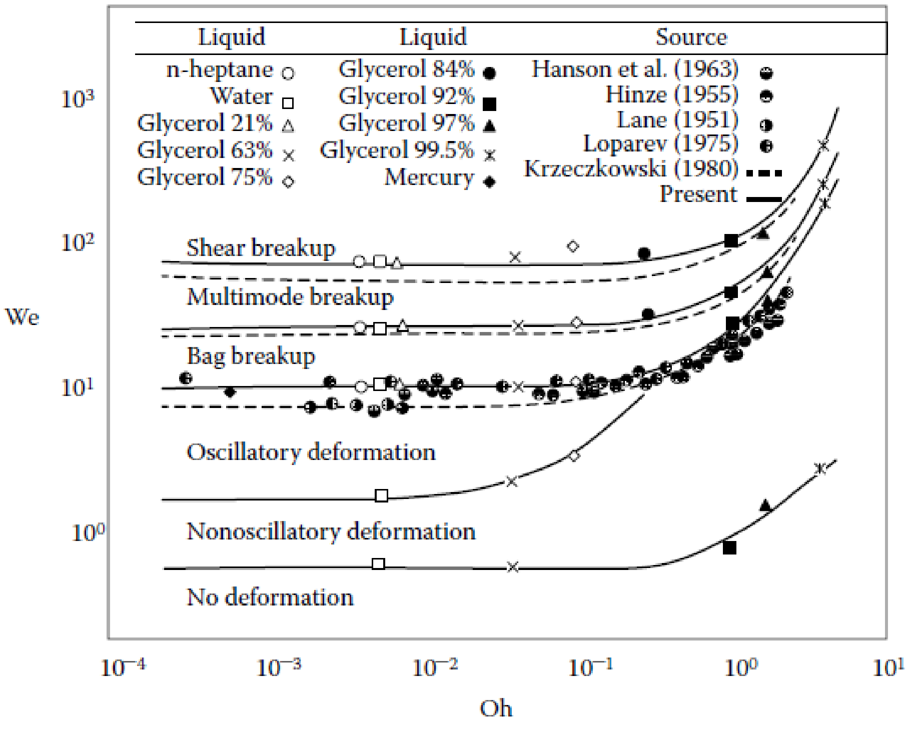

Figure 2.17: Threshold for each regime as proposed by [9].

2.7 Analytical and DNS Approaches

Despite the wide range of modelling efforts throughout the available literature, none is able to accurately predict and describe every stage of secondary atomization [5]. Some use models based on assumed underlying governing physics, while others create entire experimentally determined propositions for secondary atomization study. Nonetheless, the success and shortcomings of these models are used to improve and extend the knowledge of secondary atomization computational resolutions.

The use of the Taylor Analogy Breakup (TAB) model [29], is based on the similarities encountered between drop deformation and a spring-mass system where spring, external and dampening forces are analogous to surface tension, aerodynamic loading and drop viscosity, [30]. The use of the TAB model gave birth to questions regarding initiation and total breakup times, fragment size prediction and even inaccuracies predicting the frontal area of the distorted droplet, leading to incorrect calculations of drag coefficients [31, 32].

Later, the Droplet Deformation and Breakup (DDB) model was presented, where drop deformation was treated by calculating the kinetic and potential forces acting on the drop, equating these with the work done due to the pressure and viscous forces. The assumption that breakup occurs when kinetic and viscous forces are negligible related deformation with We, while mass is conserved and a frontal area is accurately calculated [33]. This method showed some improvements compared to TAB model, but could not predict drop deformation for low We presenting instantaneous breakup [34]. Regardless, both these models are currently used in industrial spay simulations [5]. Furthermore, the aforementioned models suffered improvements, e. g. Enhanced TAB (ETAB) model [35, 36], enabling the prediction of final droplet size and initiation times while resolving the instantaneous breakup problem for low We numbers. The droplet monitoring domain is illustrated in Figure 2.18.

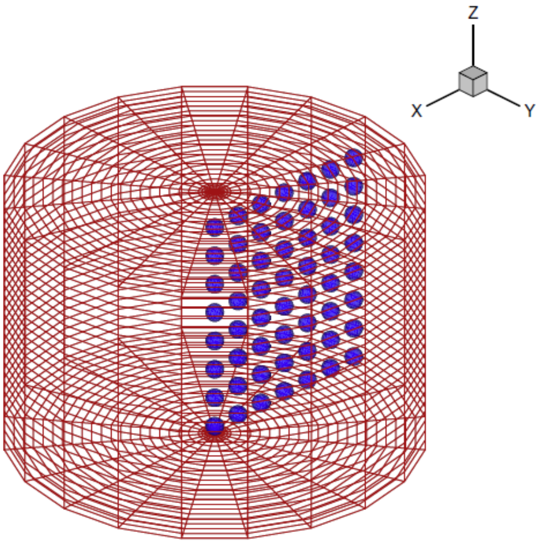

Figure 2.18: Illustration of the computational and monitoring domain where drop information is gathered for ETAB, taken from [36].

Lastly, the use of wave instability models was also considered, although with limited success. Hybrid models have been used by others to predict deformation due to aerodynamic forces and unstable wave growth. Such models are sometimes based in empirical assumptions and take advantage of the available experimental data to build an *in house* breakup model, as is the case of Rodrigues et al. [11]. The nature of these is to validate and close the gap between each model, trying to reach a general consensus enabling an accuracy increase in the numerical breakup prediction formulation.

Direct Numerical Simulation (DNS) approach enables the resolution of drop and ambient flow fields that require solutions to multiphase, unsteady and 3D flows. These methods assume that the fluids are continuous, and the success seems to increase when tracking particles with Lagrangian schemes. Volume of Fluid (VOF) methods seem to present the most widely accepted results, although similar to the analytical approach, more work is needed to further improve the quality of these methods [23, 37–39]. As seen in Figure 2.19, the quality of results using these approaches is more than acceptable, yet the ability to determine daughter droplet diameter and magnitude is still very difficult.

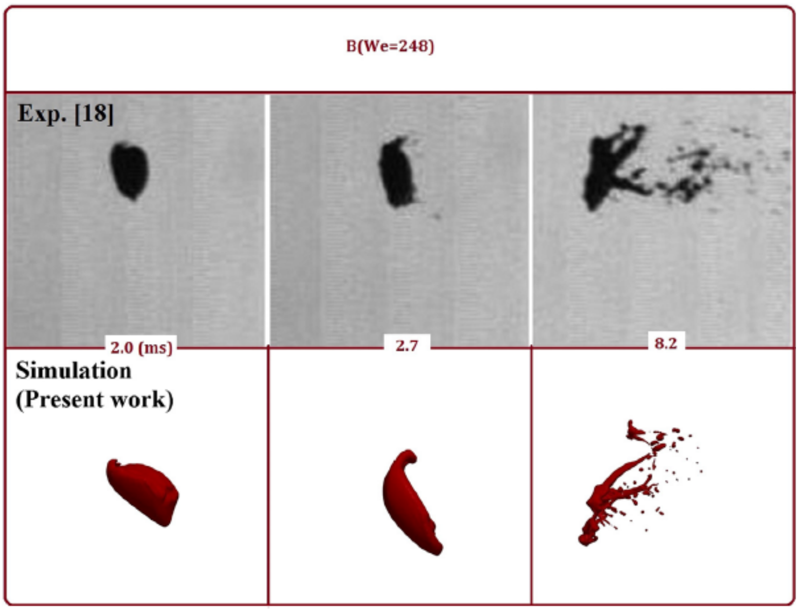

Figure 2.19: Illustration of a DNS approach using the OpenFoam software [37].

Chapter 3

Experimental Apparatus

The construction and validation of the experimental facility is described in this chapter, as well as the methods for drop diameter and velocity determination. The need to achieve velocity profiles' uniformity is of paramount importance to properly visualize the breakup phenomena without inducing unwanted velocity gradients in the main flow region, while also verifying the boundary layer thickness is kept as low as possible. This chapter will also present the main aspects that enable two-phase interaction. The image acquisition and drop injection system are thoroughly described. The fluids and the drop generating needles are specified and thoroughly examined throughout the chapter.

3.1 Experimental Facility

To achieve the necessary flow speed the use of a low-speed wind tunnel in necessary. A $15\,\mathrm{kW}$ ventilator is used to induce the flow through a system of tubes into the tunnel, with an approximate flow rate of $3000\,\mathrm{m^3\,h^{-1}}$. The exit nozzle has a cross section of $200\,\mathrm{mm} \times 40\,\mathrm{mm}$. Because no impact regimes are studied, the test section of the experimental facility has no upper or lower boundaries, to mitigate flow disruptions and for a better work environment. Since visualization of the drops interaction with the air stream is one of the main objectives in this study, two glass screens are equidistantly located on the sides of the wind tunnel outlet, with the furthest one being a diffusion glass used to spread the light evenly, so the captured image is consistent. All of the rigging and facility is properly levelled, so no other forces influence the drop other than gravity, Figure 3.1.

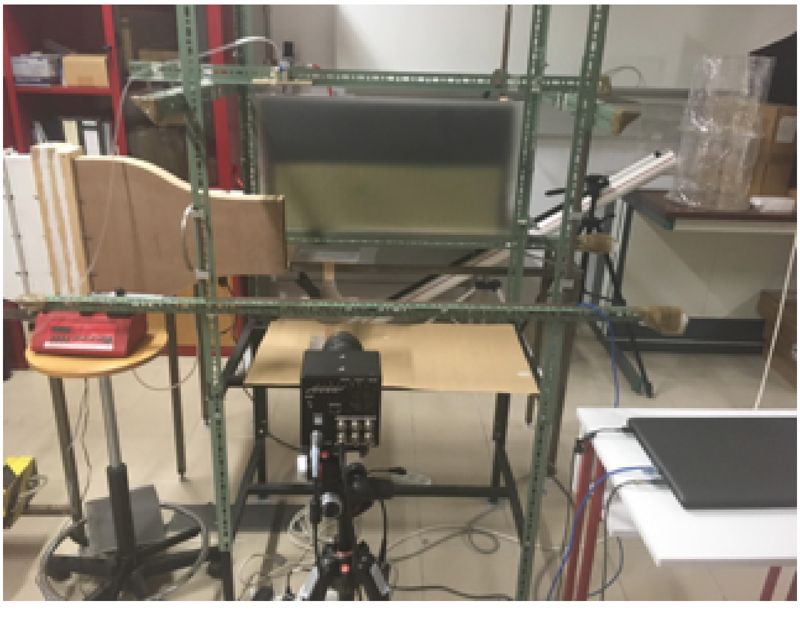

Figure 3.1: Experimental Facility.

3.1.1 Wind Tunnel

The three main components in the wind tunnel construction are Diffuser, Settling Chamber and Contraction. The first two were already existent due to Ref. [40] work and will be briefly presented. A contraction is built in order to achieve the desired velocities and flow for the visualization of different secondary atomization regimes.

Diffuser

The existing diffuser has a length of $335\,\mathrm{mm}$, with a $100\,\mathrm{mm} \times 100\,\mathrm{mm}$ inlet and $400\,\mathrm{mm} \times 40\,\mathrm{mm}$ outlet, meaning the angle of the diffuser is approximately $48.24°$. Typically, the angles of diffusers have a maximum of $15°$ to avoid separation of the flow on the steep angle increases, and since the existing one has a large angle, screens were placed so that the flow doesn't experience this phenomena, [41]. Diffusers are used to decelerate the flow, thereby enabling static pressure recovery allowing the reduction of the driving motor's load.

Settling Chamber

The settling chamber is composed of honeycombs and screens, Figure 3.2. As mentioned before, this component of the wind tunnel was constructed before this study, and the maximization of the overall benefit of this section was verified, as shown in Table 3.1, confirming that the length of the honeycombs is 6 to 8 times bigger than its diameter. Screens were placed to induce a pressure drop proportional to U^2 allowing for a more uniform velocity profile and reducing boundary layer thickness.

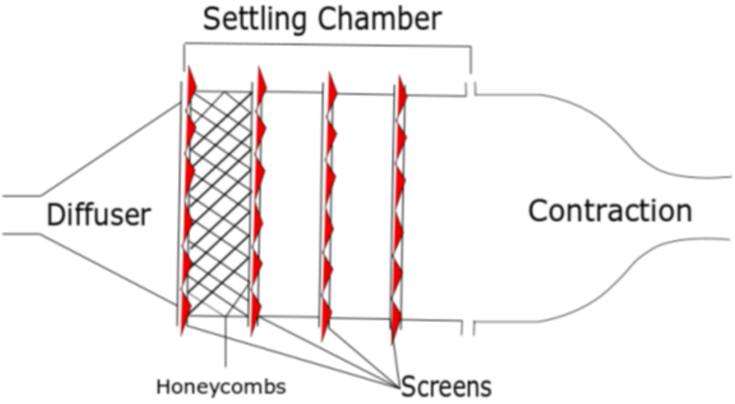

Figure 3.2: Schematic of the Settling Chamber [40].

The spacing of the screens must be enough for the static pressure to fully recover from a perturbation before reaching the next one, and minimum spacing should be the magnitude of the eddy containing the maximum energy [42].

Table 3.1: Settling chambers design parameters [40].

Section Area[mm^2]		400×40
Area[mm]		0.016
Equivalent Diameter[mm]		142.7
Honeycombs	Cell Area[mm]	26.0
	Cell Diameter[mm]	6.0
	Cell Length[mm]	48.0
Screens	d[mm]	0.25
	L[mm]	1.34
	β	0.67
	K	$\approx$ 1.80
Space Between Screens[mm]		30

Table 3.1 demonstrates the design parameters of this section, where K is the pressure drop coefficient.

$$\mathrm{K} = 6.5\left(\frac{1-\beta}{\beta^2}\right)\left(\frac{Ud}{\beta v}\right) \quad (3.1)$$

and β is a relation between screen length and diameter given by:

$$\beta = \left(1 - \frac{d}{L}\right)^2 \quad (3.2)$$

Contraction

Contrary to the diffuser, the contraction is used to accelerate de flow. If the contraction length is big enough it will avoid separation but, in contrast, will increase boundary layer thickness. The design criteria used was that proposed by [43] which states that the shape of the contraction should be a smooth match between two cubic arcs. The main objective is to maintain and guarantee flow uniformity on the exit plane and avoid separation. For this, the Contraction Ratio (CR) is set, and later C_{p_e} and C_{p_i} are obtained so that these criteria could be met:

$$\mathrm{CR} = \frac{A_1}{A_2} \quad (3.3)$$

$$C_{p_i} = 1 - \left(\frac{V_i}{U_{\infty,1}}\right)^2 \quad (3.4)$$

$$C_{p_e} = 1 - \left(\frac{U_{\infty,2}}{V_e}\right)^2 \quad (3.5)$$

where i and e represent the point of minimum and maximum wall velocity, and 1 and 2 the inlet and outlet planes, respectively.

Once C_{p_e} and C_{p_i} are determined one must read the values of F_i and F_e from Morell's graphics, to determine the match point of the two arcs, given by:

$$X = \left[1 + \left(\frac{1}{CR}\right)\left(\frac{F_i}{F_e}\right)^{-1}\right] \quad (3.6)$$

The contour is defined by:

$$\frac{H - H_2}{H_1 - H_2} = 1 - \frac{1}{X^2}\frac{x^3}{L^3} \quad for \quad \frac{x}{L} < X \quad (3.7)$$

$$\frac{H - H_2}{H_1 - H_2} = \frac{1}{(1 - X^2)}\left(1 - \frac{x}{L}\right) \quad for \quad \frac{x}{L} > X \quad (3.8)$$

where H_1 and H_2 are the inlet and outlet height respectively, x is the coordinate and H is the total length of the contraction.

The value of C_{p_i} is calculated using Eq. 3.9.

$$C_{p_i} = 0.7\left(\frac{\frac{x_0}{H_1} + 0.9\frac{x_1}{H_2}}{\frac{s}{H_1}}\right)(10^{-6}Re_x)^{\frac{1}{15}} \quad (3.9)$$

$$Re_x = \frac{U_{\infty,1}}{H_1}\left(\frac{\frac{x_0}{H_1} + 0.9\frac{x_1}{H_2}}{v}\right) = O(10^6) \quad (3.10)$$

According to Stratford's separation criteria for turbulent flow, [44]. The value of s/H_1 is assumed to be 0.13 as proposed by Morell [43], x_0 is the distance from the virtual origin of a boundary layer to nozzle beginning (with $x_0/H_1 = 0.3$ also proposed by Morell) and x_i the axial coordinate for the minimum wall velocity. The remaining correlations are taken from the author's graphics. The exit velocity non-uniformity is given by and it is found to be approximately proportional to C_{p_e} so for practical purposes $\tilde{u}_2 = 0.019C_{p_e}$ is accurate enough to ensure that the exit non-uniformity will not be more than 2%.

$$\tilde{u}_2 = (0.19 \pm 0.001)C_{p_e} \quad (3.11)$$

The last screen should be placed at $0.2\ D_{eq_i}$ (inlet equivalent diameter) after the inlet plane, and $0.4\ D_{eq_e}$ (outlet equivalent diameter) should be added before the exit plane, so that the flow can stabilize. With this, the total nozzle length is given by $L_T = 0.2D_{eqi} + L + 0.4D_{eqe}$, Table 3.2.

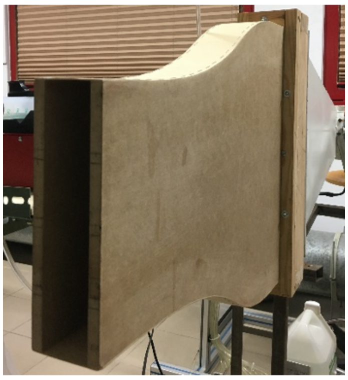

Figure 3.3: Contraction mounted on the wind tunnel.

Table 3.2: Paramenters for contraction design.

Contraction Ratio	2
C_{p_i}	0.284
C_{p_e}	0.058
$\mathrm{H}_1[mm]$	400
$\mathrm{H}_2[mm]$	200
X	0.437
$\mathrm{L}[mm]$	450.40
$\mathrm{L_T} = \text{Total Nozzle Length}[mm]$	519.31
$\text{Width}[mm]$	40

3.1.2 Calibration

The change of any component of the wind tunnel requires the verification of the velocity profiles produced by the flow at the nozzle exit to ensure uniformity. This calibration is divided into several steps to guarantee an efficient and quick verification of the profiles. It is of paramount importance to refer that the air is provided by the ventilator, through a rig that contains three guillotines. One of the guillotines is closed for the entirety of the present work, and the first one, from now on referred as G_1, is fully open since it is the maximum velocity configuration in relation with the guillotine used for the present wind tunnel [45]. Velocity is regulated by the second guillotine, G_2.

Maximum Velocity

The first step is to measure the increase of velocity with the variation of G_2's, aperture. For this, the use of a pitot tube and a U-shaped manometer are essential for the pressure measurements and subsequent velocity determination. G_2 is initially totally closed with the aperture incremented by $0.05\,\mathrm{m}$ between every measurement. After the maximum velocity is achieved with the guillotine opening, the frequency of the ventilator was increased by a factor of $1\,\mathrm{Hz}$ from $25\,\mathrm{Hz}$, minimum frequency, to $45\,\mathrm{Hz}$. The reason for the upper frequency threshold is that the recommended maximum range is $50\,\mathrm{Hz}$ and since the desired velocity is achieved there's no need to push it further and risking damage to the fan or even the driving motor.

The pitot tube connected to the U-shape manometer measures the difference between the total and static pressures Δh with an error of $0.5\mathrm{mm}$. The velocity is calculated using Eq. 3.12 and 3.13.

$$\frac{1}{2} \times \rho_{air} \times U^2 = \rho_{H_2O} \times g \times \Delta h \quad (3.12)$$

$$\Leftrightarrow U = \sqrt{\frac{2 \times \rho_{H_2O} \times \Delta h_1}{\rho_{air}}} \quad (3.13)$$

As seen in Figure 3.4a) a polynomial fit is employed in the present velocity determination, since it accounts for measurement errors and has an acceptable fit throughout the various guillotine positions. This is the combination of the mean values encountered in three different tests performed for this step.

Once the G_2 is fully open, velocity is increased with the aid of the frequency variation, meaning that the operation of the wind tunnel can be continuous and a linear fit can be applied, as seen in Figure 3.4b). Therefore, the variation of velocity can be plotted in terms of Δh_{ref} (static pressure measured through water height in a manometric tube), measured throughout all the $G2$ and frequency variation, to plot Figure 3.5.

The relation between Δh_{ref} and the velocity is of paramount importance for the ability to test specific velocities. Although there is an associated error, as mentioned before, it lays acceptably in the general point distribution, allowing a close estimation of the velocity.

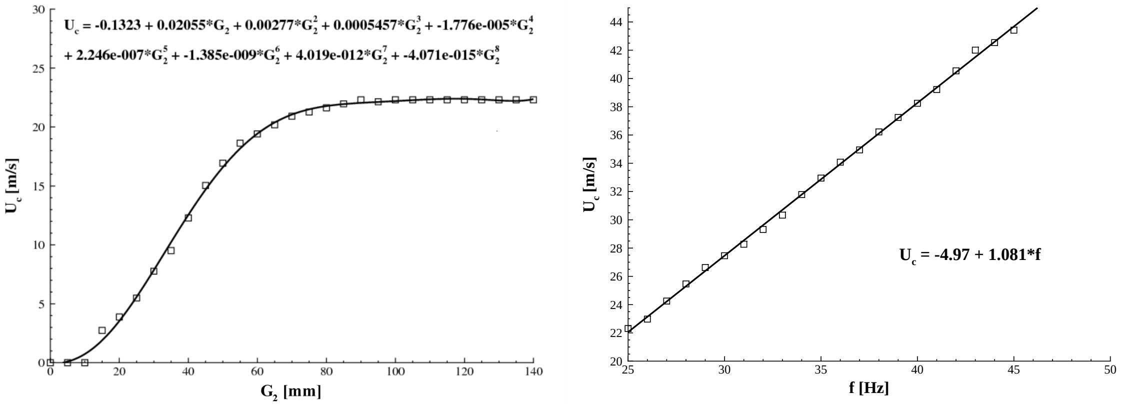

(a) (b)

Figure 3.4: Velocity increase due to the variation of a) Guillotine's aperture; b) Frequency variation.

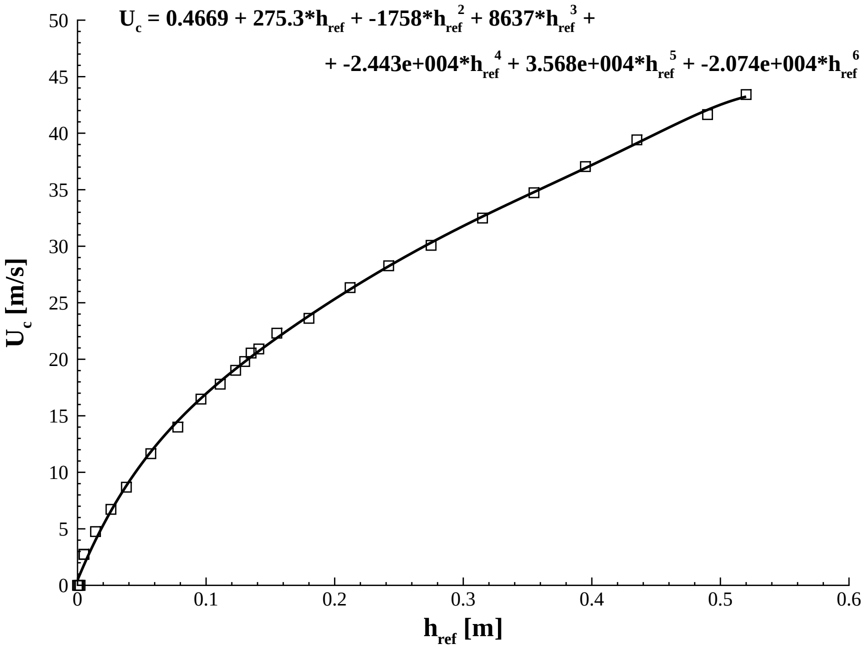

Figure 3.5: Velocity variation plotted against Δh_{ref} due to $G2$ and frequency variation.

Vertical Velocity Profiles

As desired, the interaction between the droplet and cross-flow should not display any abrupt velocity changes other than the moment when the drop effectively enters the airflow. Thus, the verification of a uniform, plug velocity profile is required to ensure that during the breakup stages no velocity gradients are present. Since various flow speeds are used, the determination of the profile for each of these is the objective of this subsection.

Knowing the range of velocities at which the breakup stages ensue, four wind speeds ($\mathrm{U_c} = 10\,\mathrm{m\,s^{-1}}$, $\mathrm{U_c} = 15\,\mathrm{m\,s^{-1}}$, $\mathrm{U_c} = 25\,\mathrm{m\,s^{-1}}$ and $\mathrm{U_c} = 35\,\mathrm{m\,s^{-1}}$) are selected to further prove the profile's uniformity. The first set of profiles measured at $10\,\mathrm{mm}$ of the tunnels' width is the point where the flow is no longer affected by wall interactions and the velocity is the same of that at $20\,\mathrm{mm}$, which corresponds to the tunnels symmetry plane. The same consideration is made for $30\,\mathrm{mm}$ and all the measurements were performed using the Pitot Tube and the U-shaped manometer, Figure 3.6b). As seen in, the use of the three positions regarding the width of the tunnel ($\mathrm{w} = 1\,\mathrm{mm}, \mathrm{w} = 2\,\mathrm{mm}$ and $\mathrm{w} = 3\,\mathrm{mm}$) is a way to ensure that even if the drop doesn't enter the flow in the tunnels geometric center, it will not experience a different velocity. This proves the velocity profiles ate not only vertically but also horizontally uniform, Figure 3.7.

The profiles display a small acceptable boundary layer influence of approximately $1\,\mathrm{cm}$ followed by a constant velocity region, in which the droplets interact with the flow and the breakup regimes are found, meaning that the contraction is built with the desired accuracy showing no signs of significant flow separation and disturbance.

As for the measuring methodology, an array of differently distributed points is chosen along the nozzle's height. For the point near the upper wall, a spacing as small as $0.5\,\mathrm{mm}$ is used, to better represent the boundary layer region. As the velocity stabilizes, the spacing is increased to a maximum of $10\,\mathrm{mm}$ to reduce the amount of data and save time during data acquisition. The Pitot tube is placed as close to the nozzle's exit as possible, Figure 3.6a), to measure the velocity profiles at the contractions' exit and assess the existing velocity gradients.

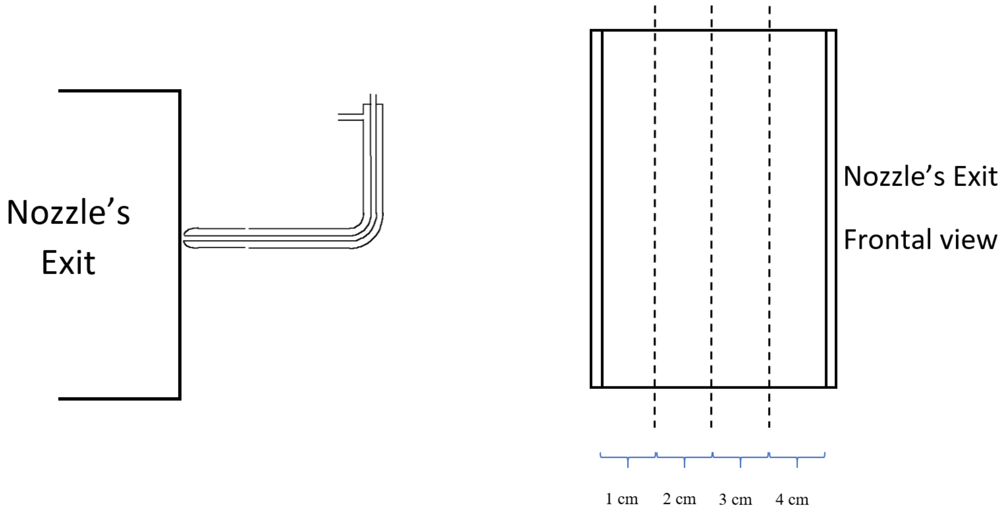

(a) (b)

Figure 3.6: Schematics of the pitot tube and measurement plane positions.

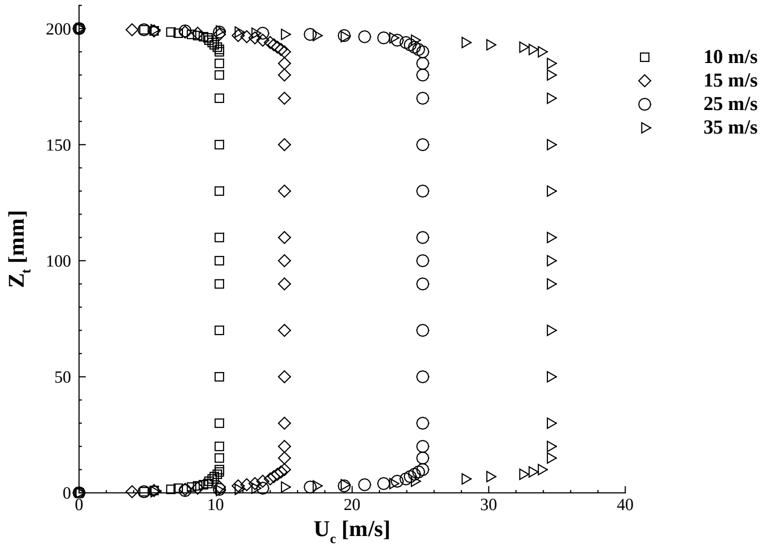

(a) $w = 10\,\mathrm{mm}$

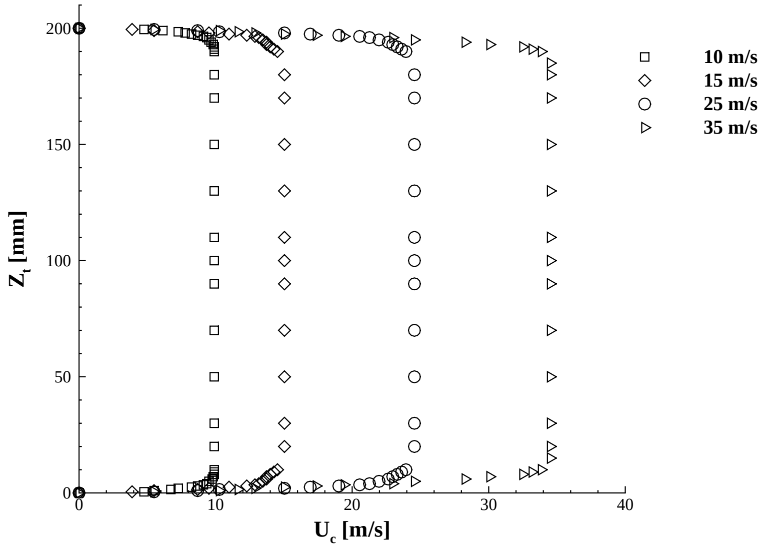

(b) $w = 20\,\mathrm{mm}$

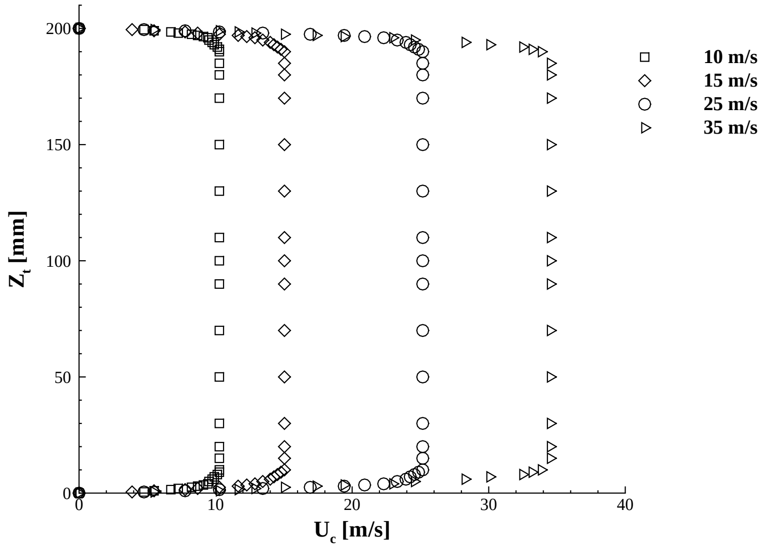

(c) $w = 30\,\mathrm{mm}$

Figure 3.7: Velocity profiles measured for various points in the wind tunnel's width, for the chosen velocities.

3.1.3 Injection System

The droplet generation is done with the use of a NE-1000 Single Syringe Pump, Figure 3.8. This pump has a range of infusion that goes from $1.459\mu\mathrm{l\,h^{-1}}$, for a $1\,\mathrm{ml}$ syringe, up to $127.2\,\mathrm{ml\,min^{-1}}$ for a $60\,\mathrm{ml}$ syringe. The present study uses $50\,\mathrm{ml}$ syringes and a pump rate of $0.5\,\mathrm{ml\,min^{-1}}$ for all mixtures, with two different flat head needles enabling the capability of drop diameter variation. Their characteristics allow a drop generation without a meaningful initial velocity, i. e., free-falling drops. The main reason for the use of this equipment is the existence of computer software that allows the variation of the drop rate remotely, meaning the use of the pump is made much easier and less time-consuming.

Figure 3.8: NE-1000 Single Syringe Pump.

The needles are attached to the syringe through an appropriate tube so the pump can be in a static stable mount, thus reducing unwanted vibrations. As stated before, the diameters of the drops are varied and this is done by using different needles with different inner diameters. The inner diameters are $0.30\,\mathrm{mm}$ and $1.50\,\mathrm{mm}$ for the Light Blue and Olive colours, Figure 3.9. For each mixture, a different set of needles was used to avoid contamination of the drops.

Figure 3.9: Stainless steel needles. Correspondent inner diameters: Olive - $1.50\,\mathrm{mm}$; Light-Blue $0.30\,\mathrm{mm}$ [46].

3.1.4 Image Aquisition System

As the time-frames underlying the present study are very small, the use of a high-speed camera is essential to capture and analyse different test conditions. The camera used is a Photron

FASTCAM mini UX50 with a $1.3\,\mathrm{mp}$ (mega-pixel) image resolution at frame rates up to $2000\,\mathrm{fps}$ and can record at $16\,000\,\mathrm{fps}$ at the expense of a resolution decrease. Attached to the camera is a Macro Lens Tokina AT-X M100 AF PRO D with a minimum focus distance of $300\,\mathrm{mm}$, a focal length of $100\,\mathrm{mm}$, a $1:1$ macro ratio and a filter size of $55\,\mathrm{mm}$.

Figure 3.10: Photron FASTCAM mini UX 50 and the Macro Lens Tokina AT-X M100 AF PRO D.

For the current experiment, the characteristics of image capture (resolution, frame rate and shutter) are altered with aid of the camera's computer software. This allows the frame rate to be set to $2500\,\mathrm{fps}$ and the shutter of the lens to $1/10\,000\,\mathrm{s}$, which means a bigger number of images are captured when the trigger is activated. The shutter variation helps mitigate the blurriness in the images, yet with its increase, the images turn darker because of a smaller light exposition. Figure 3.11 is a representation of the drops insertion and travel planes superposed with an actual representation of the camera's image acquisition.

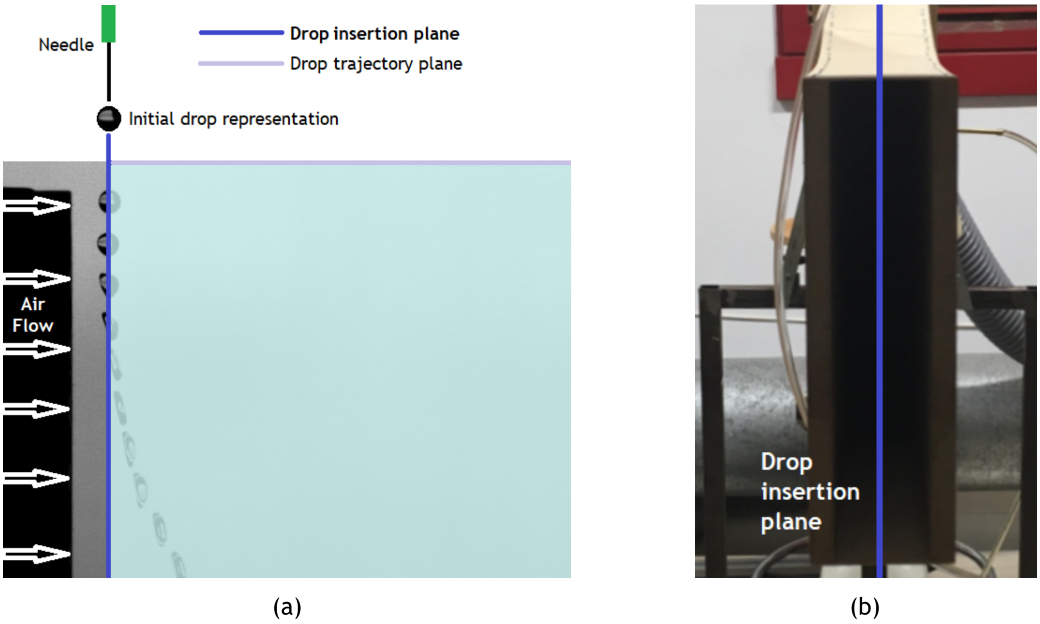

(a)

(b)

Figure 3.11: Representation of: a) drop insertion plane with the front faced tunnel nozzle; b) lateral view of drop insertion and travel planes.

3.1.5 Illumination System

Acceptable and clear quality images are only obtained by the high-speed camera with the appropriate lighting apparatus. The need for near perfect contrast between the droplet, background and any other objects present in the image is essential to enhance the image treatment accuracy. Moreover, it is easier for the Matlab algorithm, mentioned in Subsection 3.2.1, to eliminate small errors and disturbances if the image is clear and consistent. For this, several $96\,\mathrm{W}$ LEDs ribbons are attached to a flat wood board connected to a power supply. This converts alternated into direct current eliminating the light flickering, captured by the camera in other AC light sources, Figure 3.12. The room was kept in complete darkness during the image acquisition. For a more uniform light display the LED's were mounted behind a diffusion glass and the camera, droplet and lighting planes are all parallel.

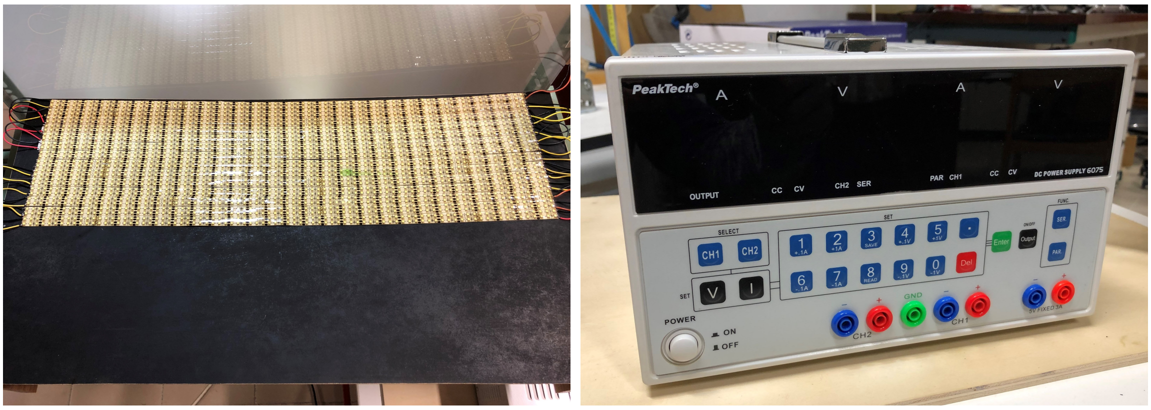

(a) (b)

Figure 3.12: Representation of: a) LED's mounted on the flat board; b) power supply.

3.2 Methodology

Before any measurement or test is performed, a detailed work structure is required to minimize waste of fuel and ensure the best results and accuracy. This section presents the steps necessary for the present works' image characterization.

Once the tunnel is set and calibrated, the first step is to identify each regime and the respective cross flow velocities. With this the threshold of each breakup mode is determined, making it easier to set the velocity for the desired stage and experiments throughout this work. Three tests are performed for the onset of each regime, i.e., the images are captured for whenever each regime appears for the first time. This allows for the images to show each of these without any interferences or transition phenomena, excluding the Dual Bag Breakup regime.

Every time the flow velocity is increased or fluid is changed, it is necessary to assure the position of the camera remains unaltered. Markings on the floor allow the camera to always be at the same distance of the testing facility and levels in the camera enable the centring of the desired image. The test section is always cleaned and kept tidy, especially the diffusion glass because the presence of impurities and dust can be captured easily by the camera and the Matlab™ software produces undesired errors. The reference snapshot, explained later in this section, is also taken for every test to ensure the minimal error associated to drop characteristics determination.

3.2.1 Image and Data Processing

Pixel Size

All the data is recovered in pixels since all the experimental footage from the present work is retrieved through the high-speed camera. The image scaling can be very different with even the slightest camera angle or position changed. For every test condition, and because not all of the tests are able to be executed on the same day, a reference was used to determine the pixel size. The reference used was a needle with a known outer diameter of $1.82\,\mathrm{mm}$, Figure 3.13a.

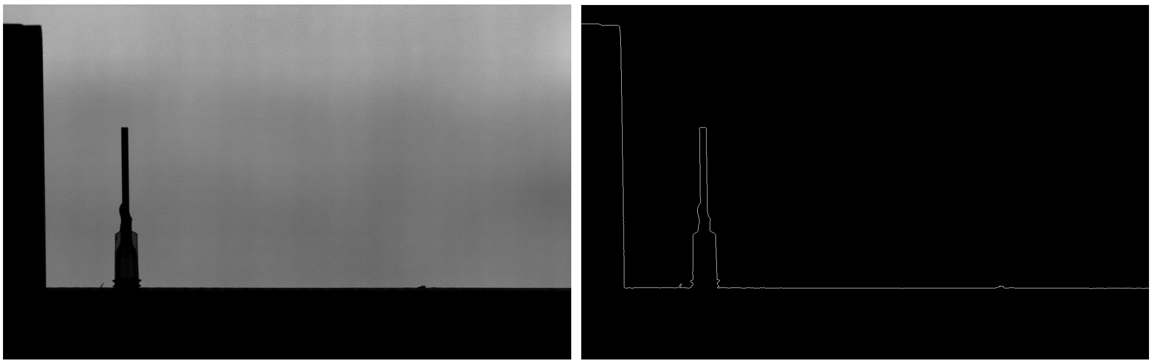
(a) (b)

Figure 3.13: Reference needle, 3.13a, snapshot acquired using the camera's software and reference snapshot in binary outlining the needle's contour 3.13b.

With the aid of a Matlab™ Algorithm, an "$in\ house$" built code code is used to outline the needles outer contours, and measure the number of pixels (adapted from [40, 47]). As seen in Figure 3.13b discrepancies may appear in the outline, so in the algorithm, a set of 10 lines of the image were chosen and cropped to fit a constant section of the needles body.

Consulting the Springer Handbook of Experimental Fluid Mechanics [48], the measurements of a length in digital image with grey values associated with the pixel positions can only be determined with an accuracy of $\pm 0.5\mathrm{pixel}$. With a pixel size of $113\,\mu\mathrm{m}$ the error accounts for $\pm\ 56\,\mu\mathrm{m}$, 1.8% of the drops sizes used, which is more than acceptable for the expected results.

Droplet Diameter

The governing non-dimensional parameters that influence the Breakup Regimes are mainly the Weber, Ohnesorge and Reynolds numbers. The diameter and velocity of the droplets are needed to calculate these parameters.

The images acquired in each test are introduced within the Matlab algorithm to determine the drops diameters. This code was developed so the desired image can be selected and transformed into a matrix of pixels, were each of these corresponds to a certain value. To determine the diameter, a background image and an image with the drop are needed, as shown in Figure 3.14.

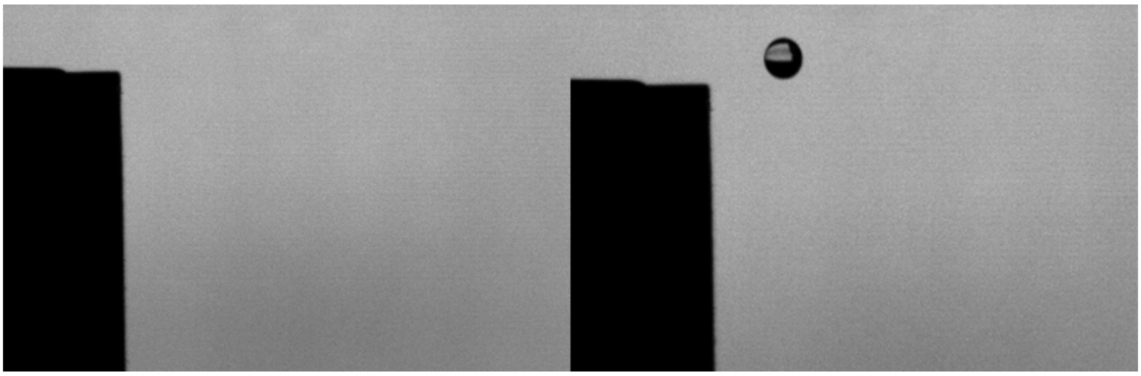

Figure 3.14: Background and Drop image to be subtracted.

The algorithm uses the image of the full droplet and subtracts it from the background image. This alone only outputs a full black image with no information available as seen in Figure 3.15a), so it proceeds to turn the subtraction into binary and the drop starts to appear. The zeros correspond to black pixels and the ones correspond to white pixels, and the image appears as 3.15b). Because of reflections and other disturbances in the images only the outline and some other points inside the drop appear in the binary condition. To achieve the full white drop, a filter is used to fill the drops' perimeter and create the full binary drop. Another filter is used to eliminate possible errors outside the perimeter caused by unavoidable dust particles or small reflexes due to the lighting rig.

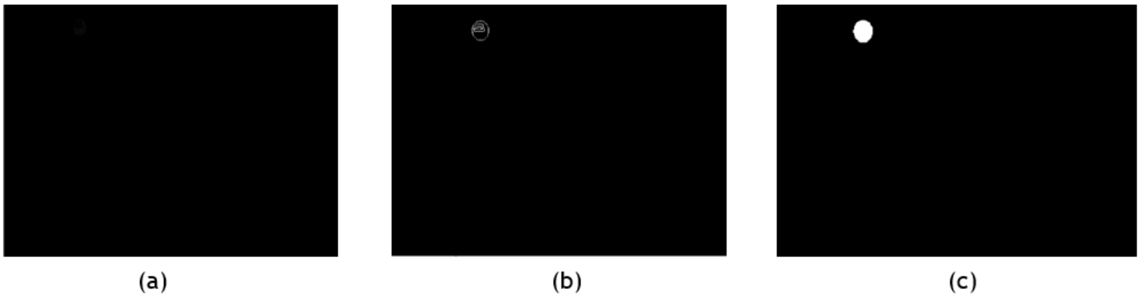

(a) (b) (c)

Figure 3.15: Image in binary with use of MatLab algorithm.

With the aid of the software's capabilities, the maximum length and height of the drop are determined in pixels. Both lengths are calculated because, during the fall, the drop contracts and stretches so the values of these two parameters vary. Therefore, diameters of different drops are determined in order to reach a mean value to verify its spherical form. All vertical and horizontal lengths are considered from the first full drop to appear in the images to the last one.

These lengths are determined by adding the values of each column. Taking into account, as mentioned before, that ones and zeros correspond to white and black pixels respectively, the column with the maximum number of pixels corresponds to the vertical maximum length of the drop. For the horizontal maximum length, the same matrix is used, although the zeros and ones are inverted, and adding all the values of the lines then subtracting them to the total number of horizontal pixels in the image ($1280\mathrm{p}$) we obtain the wanted value.

With the pixel size already known, being that the measurements in pixel of each droplet have a minimum value of $26\mathrm{p}$ and maximum of $28\mathrm{p}$, the size of the generated droplet was calculated to be the mean value: $3.1\,\mathrm{mm}$. As mentioned above, various tests are conducted to minimize the error associated with the measurements and achieve an accurate value of diameter. The images only show the drop in two dimensions, despite knowing the real drop varies its shape in three dimensions. This is accounted for, verifying that the maximum vertical and horizontal lengths never exceed 2% of the initial drop diameter, thus it is possible to assume the drops spherical form.

Velocity Determination

The velocity of a droplet at the onset of breakup is crucial for the determination of the Weber number. For this, the same image treatment is done, but instead of measuring the vertical and horizontal lengths the determination of the centroid enables the approximation of the droplets general trajectory, Figure 3.16. This approximation is used in the existing literature, suggesting the treatment of the droplet as a point of mass to better predict its behaviour and trajectory.

In this case, three images are used: the background, the droplet before the initiation of breakup and the droplet five frames before the latter one. The images are retrieved at $2500\mathrm{fps}$, meaning the interval between the two frames accounts for a time-step of $0.8\,\mathrm{ms}$. Knowing the distance and time travelled between images, the velocity is calculated.

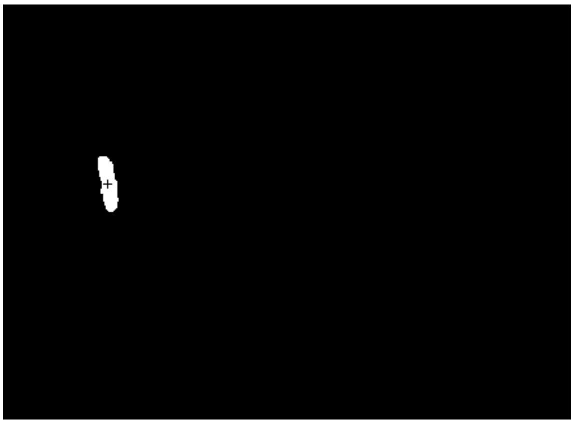

Figure 3.16: Representation of the drops centroid, using the Matlab software.

Using two consecutive frames can induce unwanted errors in velocity determination because of the very small time elapsed between each. Therefore a choice of 5 frame interval is considered and velocities of both are compared to assess the error propagation inherent to different time intervals. The difference between the 5 frames ($2\,\mathrm{ms}$) and 1 frame ($0.4\,\mathrm{ms}$) intervals is about $0.01\,\mathrm{m\,s^{-1}}$, meaning the error propagation ends up not being as great as thought, yet the consideration was maintained. For each cross-flow velocity and for each drop three tests are made in order to determine a mean velocity value.

3.3 Fluid Properties

The present work utilizes four different fluid mixtures: $\mathrm{H_2O}$, Jet A-1 100%, Jet A-1 75% - 25% HVO and Jet A-1 50% - 50% HVO, where HVO is the NEXTBTL Hidro-processed Vegetable Oil [49]. The use of water is of importance because it is known as a reference fluid and its properties are well defined in the available literature. The main fluid properties (density, surface tension, and viscosity) are measured in a controlled environment in the following conditions: Temperature $22^\circ \pm 1^\circ$; Humidity 50%. The use of such percentages is chosen because of the ease to mix the fuels without waste. It is also a way to define halfway thresholds: 50% - 75% - 100%.

The current mixtures are already utilized in the work of [40, 47, 50], so the next subsections present the measurements and results conducted by the respective authors.

3.3.1 Density

Density ρ is the ratio between the mass and volume of a homogeneous solution at a specific temperature. The method used to determine this property is by pycnometer, considered very accurate for both fluids and solid objects. Table 3.3 demonstrates the values of the experiments obtained and presented by [47].

Table 3.3: Density determination, adapted from [47].

Fluid	*Essay*	ρ[g/ml]	ρ[kg/m^3]	
Jet A-1 100%	1	0.7980	798.0	798.3
	2	0.7986	798.6	
Jet A-1 75% - 25% HVO	1	0.7948	794.8	785.0
	2	0.7951	795.1	
Jet A-1 50% - 50% HVO	1	0.7922	792.2	792.4
	2	0.7925	792.5	
H_2O			1000.0	

It is worth noticing the decrease in density with the decrease of Jet Fuel concentration. Albeit, Jet A-1 100% demonstrates a higher but not much different value compared with the half mixture. The table does not include all of the mixtures tested, and only the ones relevant for the present work are illustrated.

3.3.2 Surface Tension

The surface tension σ is given by the specific free energy of a liquid surface at the interface of another fluid. The measurements performed are able due to the use of a Data Physics – OCAH200 employing the pendant droplet method. At the time of the measurements, the machine had been recently calibrated to an accuracy of 0.6%.

Table 3.4: Surface Tension determination, adapted from [47].

Fluid	Essay 1[mM/m]	Essay 2[mM/m]	Essay 3[mM/m]	σ[mM/m]
Jet A-1 100%	25.49	25.49	25.13	25.37
Jet A-1 75% - 25% HVO	25.55	25.55	25.51	25.53
Jet A-1 50% - 50% HVO	24.60	24.68	24.73	24.64
H_2O				71.97

As seen in Table 3.4, three tests are performed and the mean values calculated to provide a value of surface tension for each mixture. The difference between the values is not significant, and a uniform variation cannot be established. The main difference may be encountered when a comparison is made with the water, as the value of its surface tension is higher by a significant factor (approximately 3 times).

3.3.3 Viscosity

The viscosity μ is defined as a measure of the fluids internal resistance to motion caused by cohesive forces among the fluid molecules. To measure the dynamic viscosity of the fluid a Brookfield DV3TRVCP Rheometer was used, and the Kinematic viscosity υ is calculated as follows:

$$Kinematic \quad Viscosity = \frac{Dynamic \quad Viscosity}{Density} \tag{3.14}$$

The values of each mixture are, as for the properties before, presented in Table 3.5:

Table 3.5: Viscosity determination, adapted from [47].

Fluid	ν[Pa.s]	ρ[kg.m^{-3}]	μ[mm^2.s^{-1}]
Jet A-1 100%	0.00112	798.3	1.403
Jet A-1 75% - 25% HVO	0.00144	795.0	1.811
Jet A-1 50% - 50% HVO	0.00179	792.0	2.259
H_2O	0.00100	1000.0	1.000

The viscosity of the mixtures increases with the decrease of Jet A-1 concentration, with the 100% mixture having the lowest viscosity. All of the above fluid properties are studied according to the Springer Handbook of Aviation Fuel Properties [51] and all of its influence on the respective regimes studied in this work, are presented in Chapter 4.

Chapter 4

Results and Discussion

In this section all results extracted from the image characterization mentioned in Chapter 3 will be presented, discussed and compared with the information available in the literature. Firstly, the visualization and identification of each regime is conducted, as well as respective Weber numbers. The velocity components associated with the drops movement due to the cross-flowed air stream are needed to determine the relative velocity between flow and drop so the Weber number can be calculated.

Secondly, the drops cross-stream diameter increase, until the disc-like shape appears, is studied and plotted against the time interval correspondent to the drop-flow interaction. This will help understand the drop's deformation ratio and behaviour due to different air velocities as well as correlations between these and respective a regime that ensues.

In addition, the characteristic time was calculated for each set of experiments. This will provide new data useful for the creation and improvement of current, and possibly new, computational models to predict and study the secondary atomization in a more detailed fashion.

Lastly, drop trajectory is presented and analysed for each regime. The experimental facility's validity is assessed and proven adequate for the study of Aerodynamic Breakup phenomena, while also proposing slight changes and insight on the functionality of such facility.

4.1 Visualization

The main objective of this section is to find and identify each breakup regime described in the literature, and locate possible structure differences created by the new set of mixtures. After they're identified, the search for the first occurrence of each regime is initiated, having into account that each occurs for an interval of Weber numbers instead of only one point in this spectre. It is also considered that data extracted from each of these images is sufficient to characterize the whole range of air flow speed, and consequently We numbers. Although, for example, the bag regime displays different bag structure inflations, no other significantly different scenario is found, leading to the aforementioned consideration.

All the drops are kept at the same initial diameter, D_0, and the height of the injector always at $0.25\,\mathrm{m}$ above the upper boundary of the tunnel. Since the water's surface tension is much higher than the rest of the mixtures, a needle with much smaller inner diameter is used to produce a drop of the same D_0. The rest of the mixtures produced the same mean initial diameter for the thicker needle.

4.1.1 Deformation Stage

Although a big part of the available literature refers to the first stage of atomization as Vibrational Breakup, the actual secondary atomization underlying this mechanism is not observed for any of the mixtures, Figure 4.1. This indicates that either the air flow does not have enough velocity to induce a significant force towards the initiation of breakup phenomena, or the test section is not big enough for the drop to experience secondary atomization at such low Weber numbers. Henceforth, this regime will be referred to as Deformation.

As secondary atomization is not observed, the study of these conditions is merely based in a threshold perspective, therefore excluding the calculation of maximum cross-stream diameter due to excessive calculation and only a range is significant for this characterization. For this regime, Table 4.1 presents the range of We were deformation is identified for all mixtures.

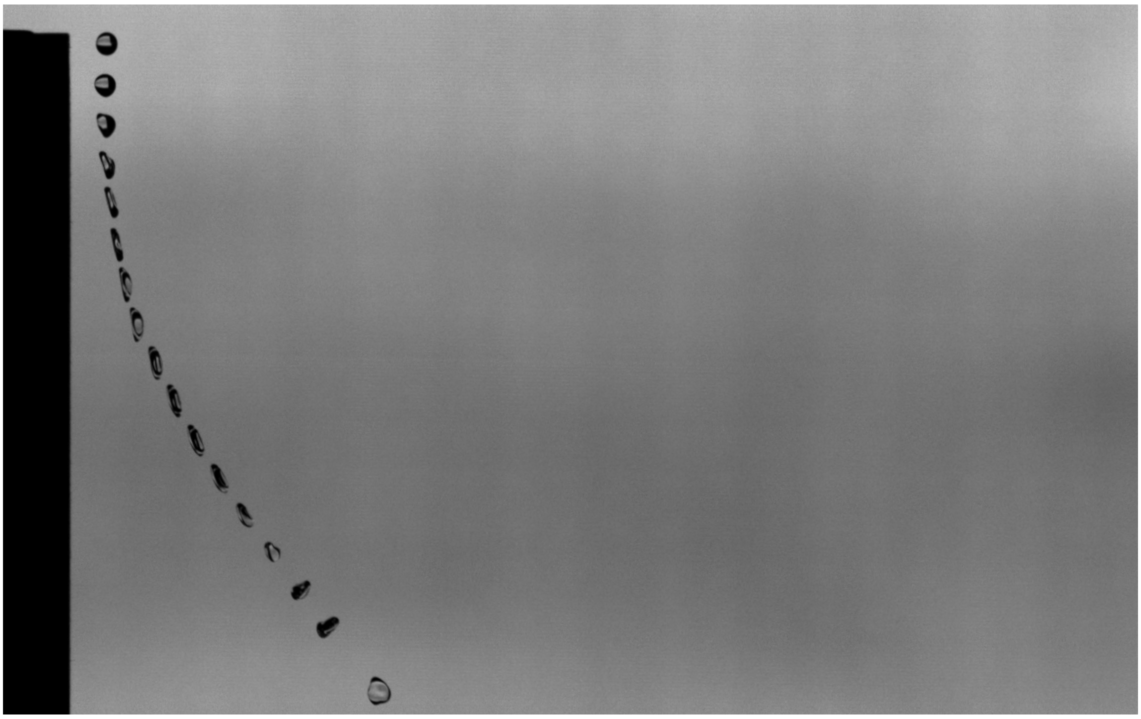

Figure 4.1: 100% Jet A1 drop deformation.

Table 4.1: Deformation Stage Weber range for all fluids.

Fluid	*Range*
Jet A-1 100%	0 < We < 13
Jet A-1 75% - HVO 25%	0 < We < 13
Jet A-1 50% - HVO 50%	0 < We < 14
$\mathrm{H_2O}$	0 < We < 17

4.1.2 Bag Breakup Stage

All the mixtures promote the creation of Bag Breakup Regime, as observed in Figure 4.2. Even though this stage starts at slightly different Weber numbers for each fuel mixture, the biggest difference are the water experiments. The use of a small drop for these implies that surface tension proves itself to be progressively more difficult to overcome. Albeit, the actual structures created in this stage do not show any differences between all mixtures. The drops' transformation into an ellipsoid followed by the bag formation, development and subsequent secondary atomization is observed, as expected. The ring created in the edges of the drop appears to contain the bulk of the volume, with the bag leading to small drops upon secondary atomization.

This leads to further fragmentation, and the ring ends up breaking into larger drops than the bag. Figure 4.2 is a representation of the images acquired from the high-speed camera for this regime.

The first frame corresponds to $t = 0\,\mathrm{ms}$, being the point of first interaction between drop and the flow field, with this consideration analogous for all the upcoming regimes. It is important to mention $t = 0\,\mathrm{ms}$ is when the drops' entire frontal area is exposed to cross-flow influence, as shown in all upcoming illustrations. Furthermore, the frames chosen for representation of all fluids are the same, corresponding to a specific structure visualization:

1. First interaction with flow - undistorted drop
2. Deformed drop - ellipsoid shape evolution
3. Bag formation
4. First case of bags' secondary atomization
5. Toroidal Ring atomization

This allows a table elaboration such as that presented below, Table 4.2. The same pattern in breakup structures is clearly noticed for the fuel mixtures, while a strong deviation is found on the $\mathrm{H_2O}$ experiments. This evident difference proves a great influence of σ on this phenomenon, expected from the analysis of We equation. The big cross-flow increment needed for the visualization of bag breakup on water experiments also promotes a shorter time interval between expected structures.

Table 4.2: Time-stamps for each structures' occurrence for the bag breakup regime.

Structure	t[ms]			
	Jet A-1 100%	Jet A-1 75% - 25% HVO	Jet A-1 50% - 50% HVO	$\mathrm{H_2O}$
1	0	0	0	0
2	10.4	10.4	10.4	6.4
3	17.2	17.2	17.2	10.8
4	21.2	21.2	21.2	13.6
5	34.4	34.4	34.4	22.4

The fluids tested show an agreeable Weber number range, within the values consulted in the literature, presented in Table 4.3, while knowing this regime is expected to ensue roughly between $12 < \mathrm{We} < 20$. The only exceptions are the water experiments which, as mentioned before, suffer greatly from the influence of surface tension force.

Table 4.3: Bag regime Weber range for all fluids.

Fluid	*Range*
Jet A-1 100%	13 < We < 20
Jet A-1 75% - HVO 25%	13 < We < 21
Jet A-1 50% - HVO 50%	14 < We < 21
$\mathrm{H_2O}$	17 < We < 26

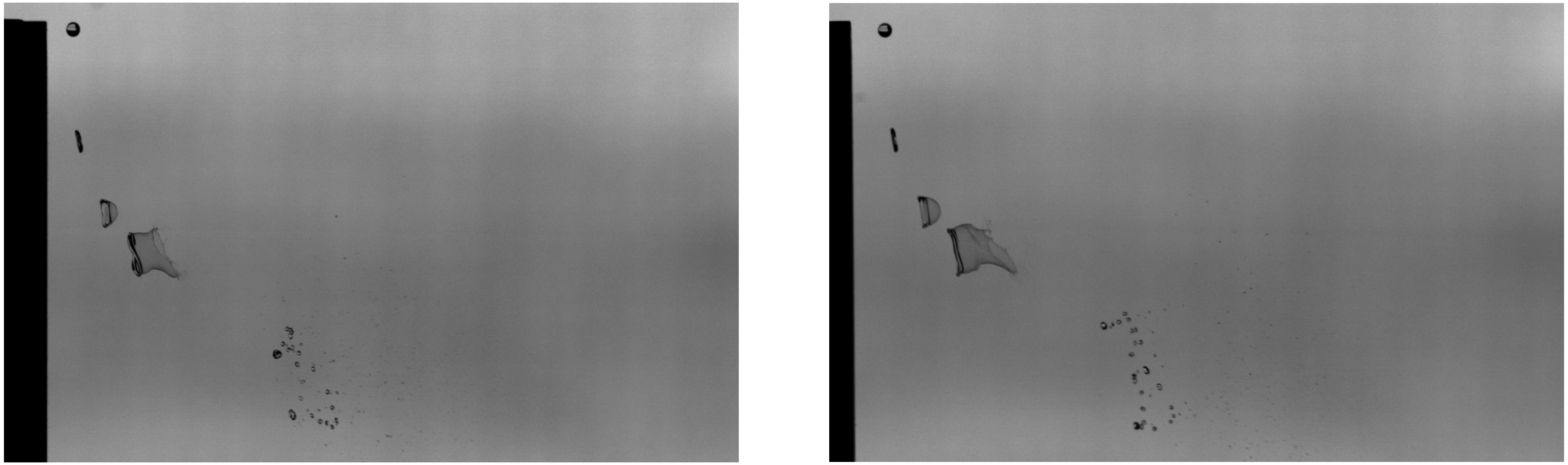

(a) Jet A-1 100%

(b) Jet A-1 75% - HVO 25%

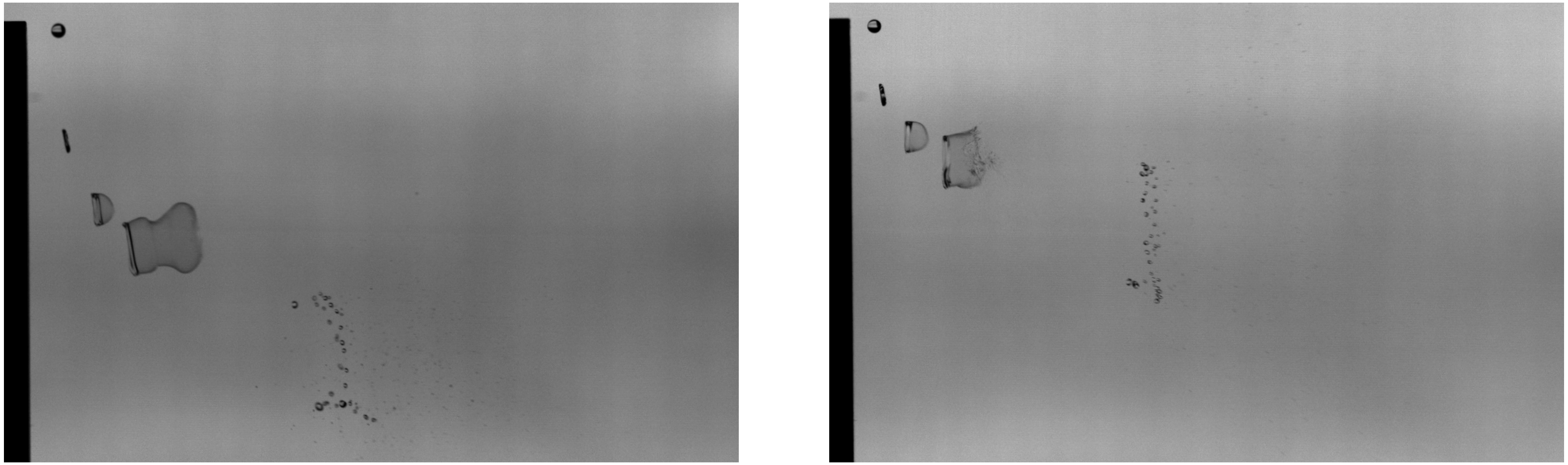

(c) Jet A-1 50% - HVO 50%

(d) H_2O

Figure 4.2: Bag Breakup sequence for the mixtures, captured with the high-speed camera, with mean drop diameter $D_0 = 3\,\mathrm{mm}$ and: a) $U_c = 9.28\,\mathrm{m\,s^{-1}}$, $\mathrm{We} = 13$; b) $U_c = 9.64\,\mathrm{m\,s^{-1}}$, $\mathrm{We} = 13$; a) $U_c = 9.81\,\mathrm{m\,s^{-1}}$, $\mathrm{We} = 14$; a) $U_c = 18.84\,\mathrm{m\,s^{-1}}$, $\mathrm{We} = 17$.

4.1.3 Multimode Stage

This stage is a way of describing three different structures. The use of a more embracing description is due to disagreement between authors while also being a transition stage with no well-defined thresholds for the different regimes found. The first to appear is the Bag-Plume regime: a bag-like structure with a plume of liquid within the bag space. This is followed by the Shear-Plume regime: a mass stripping phenomenon from the edges of the drop, with the persisting existence of a plume creation. In the present work, it is referred to as shear-plume because the stripping phenomena resembles a shear effect on the drop. Furthermore, the present experiment allows the visualization of the Dual Bag Regime that will be briefly explained. These regimes are expected to occur in between a Weber number range of roughly $20 < \mathrm{We} < 80$.

Bag-Plume Stage

As expected, with the increase of air flow speed the Bag-Plume regime appears. Due to aerodynamic instabilities, the creation of a liquid plume is observed within the bag structure and one is able to clearly identify the initiation of said transition phase in Figure 4.3. The full undistorted drop corresponds to $t = 0\,\mathrm{ms}$, as before. The structures chosen for the representation are similar to those of the previous regime, with the following time-stamps, Table 4.4.

1. First interaction with flow - undistorted drop
2. Deformed drop - ellipsoid shape evolution
3. Bag and plume formation
4. First case of bags' secondary atomization
5. Toroidal Ring and plume atomization

Table 4.4: Time-stamps for each structures' occurrence for the bag-plume breakup regime.

Structure	t[ms]			
	Jet A-1 100%	Jet A-1 75% - 25% HVO	Jet A-1 50% - 50% HVO	$\mathrm{H_2O}$
1	0	0	0	0
2	8	8	8	5.2
3	14.4	14.4	14.4	8
4	17.6	17.6	17.6	9.6
5	25.6	25.6	25.6	15.2

Once again, increasing flow velocity will decrease the time it takes for breakup to occur. The mixtures present the same structures for the same time intervals and each occurs earlier compared with the previous regime. This is reasonable, yet the magnitude of this decrease is deeply dependant on flow velocity. Water shows the same behaviour; higher speeds are necessary to achieve bag-plume visualization, promoting shorter intervals between each structure.

The creation of this plume structure is not fully understood in the available literature, yet its' occurrence is ascribed to Rayleigh-Taylor instabilities described by and instability between the interface of two fluids with different densities, where the heavier fluid is accelerated by the lighter one [5, 17, 19, 25]. In this case, the Bag-Plume regime is found to occur in the range of roughly $21 < \mathrm{We} < 40$, except for the water experiments, Table 4.5. It is of importance to notice the plume is not geometrically centred with the horizontal symmetry plane of the drop

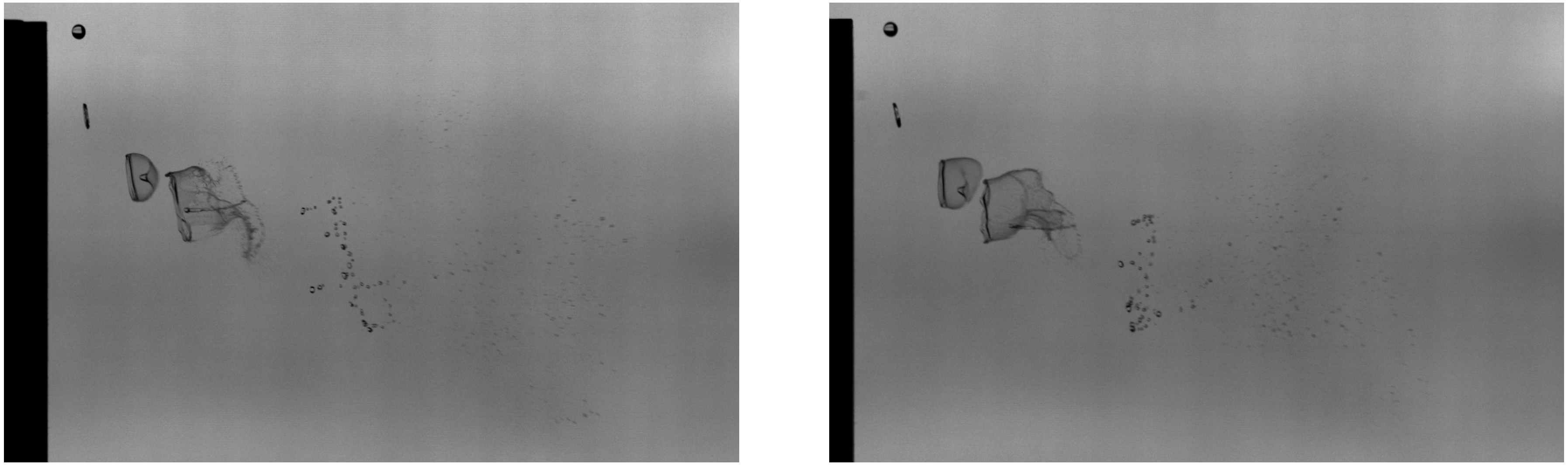

(a) Jet A-1 100%

(b) Jet A-1 75% - HVO 25%

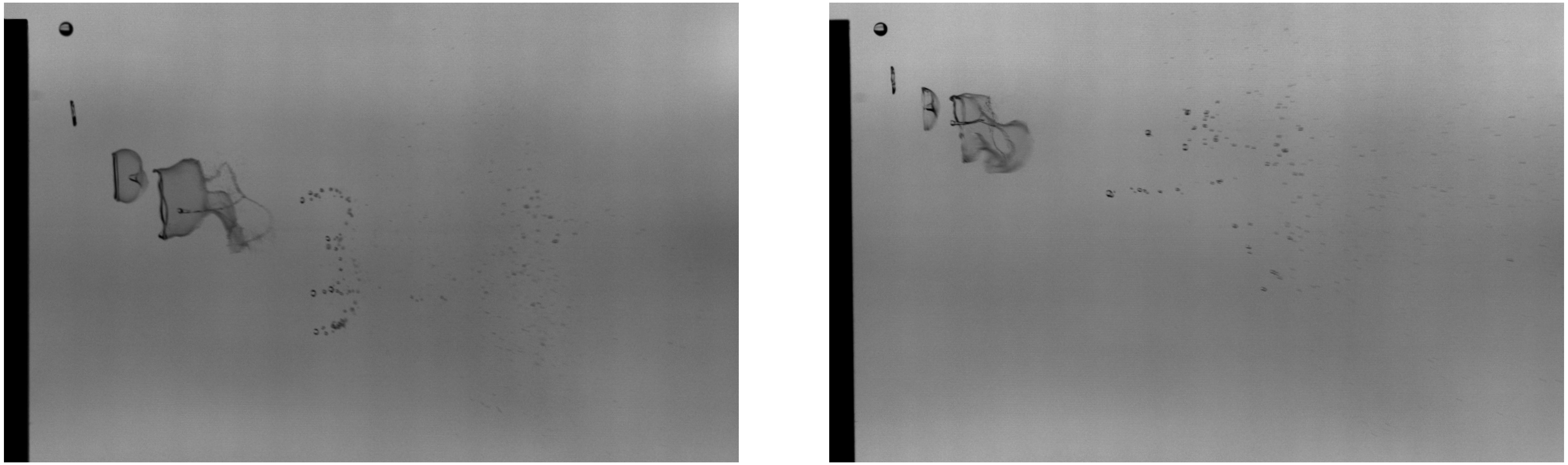

(c) Jet A-1 50% - HVO 50%

(d) $\mathrm{H_2O}$

Figure 4.3: Bag-Plume Breakup sequence for the mixtures, captured with the high-speed camera, with mean drop diameter $D_0 = 3\,\mathrm{mm}$ and: a) $U_c = 12.06\,\mathrm{m\,s^{-1}}$, $\mathrm{We} = 20$; b) $U_c = 12.21\,\mathrm{m\,s^{-1}}$, $\mathrm{We} = 21$; c) $U_c = 12.06\,\mathrm{m\,s^{-1}}$, $\mathrm{We} = 21$; d) $U_c = 23.88\,\mathrm{m\,s^{-1}}$, $\mathrm{We} = 27$.

as it travels. This, as reported, shows a somewhat arbitrary position of this structure within the bag, once again suggesting a strong influence of flow evolution on the drops' deformation stages.

Table 4.5: Bag-Plume regime Weber range for all fluids.

Fluid	*Range*
Jet A-1 100%	20 < We < 40
Jet A-1 75% - 25% HVO	21 < We < 40
Jet A-1 50% - 50% HVO	21 < We < 43
H_2O	26 < We < 36

The bag-like structure is the first to suffer atomization, and a large number of small drops are dispersed towards downstream direction, similar to the Bag regime. The ring attached to it also resembles the previous regime with the addition of the plume structure. Fragmentation of plume and ring appears to occur almost simultaneously and produce bigger drops for both structures, and these appear to contain the bulk of fluid in volume, consequently producing larger droplets than the bag.

Shear-Plume Stage

Later in the transition stages of aerodynamic breakup, the Shear-Plume regime is found, Figure 4.4. While still showing the presence of a plume on the drops' central regions, the edges suffer a shearing effect created by the ever greater aerodynamic forces. There is a stripping of liquid from it that undergoes subsequent atomization. In this case, the mass stripped from the edges breaks up into small drops. In some cases, the plume gives way to bigger drops and in others, it simply remains intact with no big atomization events. The latter case is observed fewer times than the former, and so there is an assumption that for the mean process of the Shear-Plume regime, plume disintegrates into bigger droplets than the edge stripping effect. There is seldom evidence of thin sheets of fluid, similar to the bag-plume regime and, although one could assume that this case still fits in the previous stage, the formation of thin sheets of liquid is unavoidable due to the fuel's properties as so for the inflation of these, in addition to the fact that it is observed rarely. It is not sufficient information to otherwise classify this regime, as it also occurs with certain randomness, and does not always resemble bag structures.

For this case, the image composition is done considering

1. First interaction with flow - undistorted drop
2. Deformed drop - ellipsoid shape evolution
3. Mass stripping effect and plume appearance
4. Plume remnants
5. Plumes' secondary atomization

The time stamps continue to decrease in duration, and the water experiments still require high cross-flows to achieve the same regime as the fuel mixtures, Table 4.6. On a general basis, atomization appears quite simple with the mass stripping events creating a large number of small droplets. The non-existence of toroidal rings strongly indicates a bigger plume volume and consequently large daughter drop creation. Structures three and four are joined in the water case illustration due to the superposition of images.

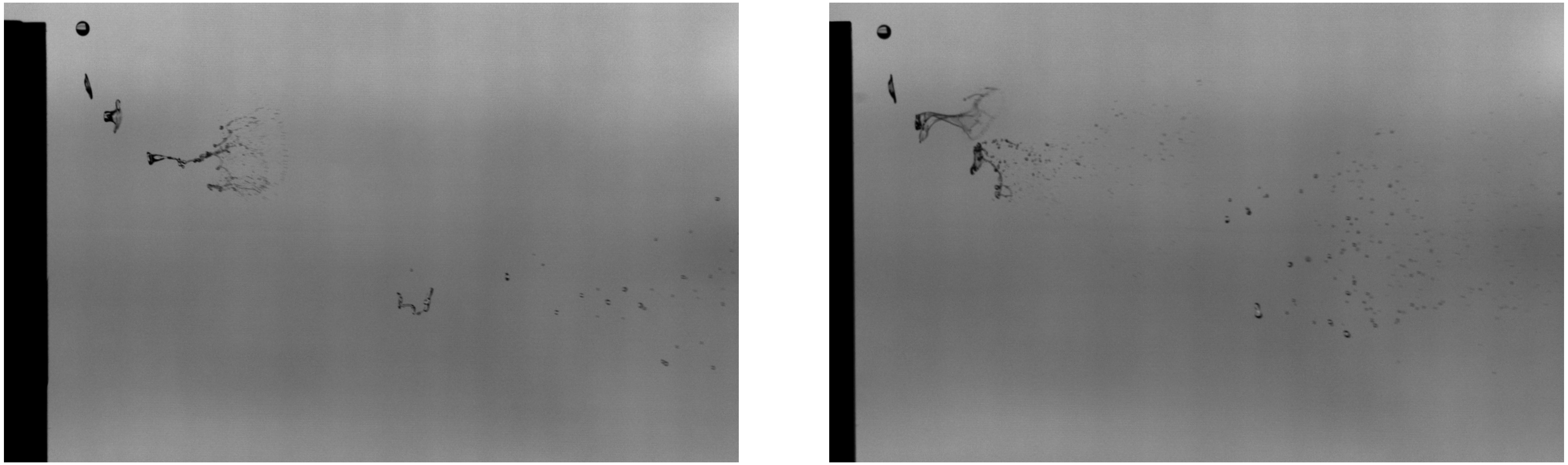

(a) Jet A-1 100%

(b) Jet A-1 75% - HVO 25%

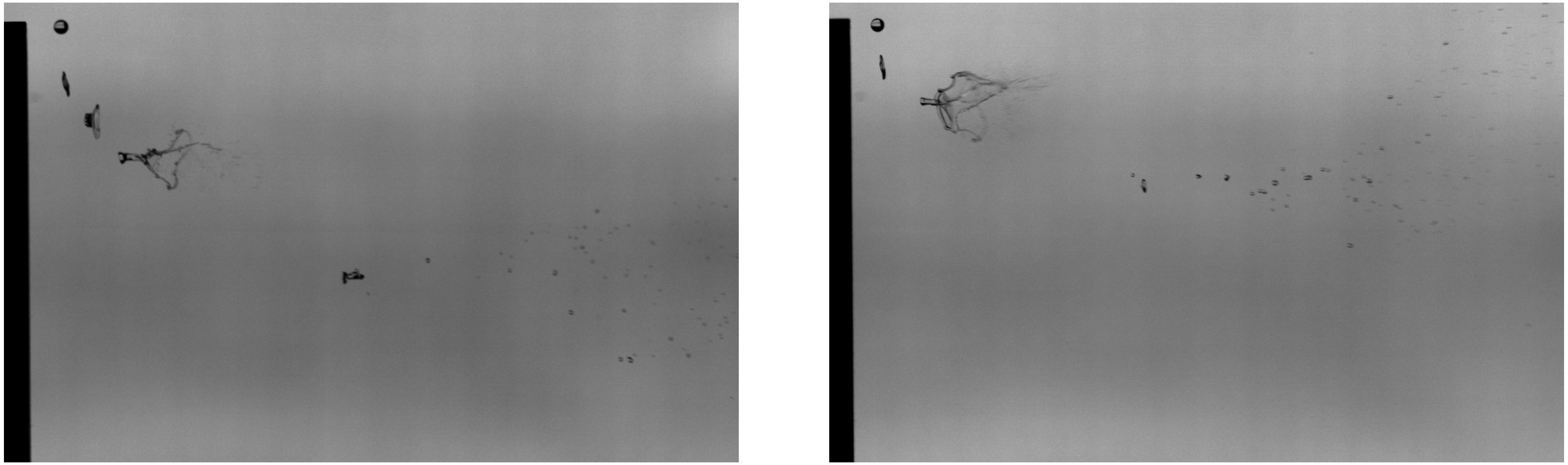

(c) Jet A-1 50% - HVO 50%

(d) $\mathrm{H_2O}$

Figure 4.4: Shear-Plume Breakup sequence for the mixtures, captured with the high-speed camera, with mean drop diameter $D_0 = 3\,\mathrm{mm}$ and: a) $U_c = 16.90\,\mathrm{m\,s^{-1}}$, $\mathrm{We} = 40$; b) $U_c = 17.00\,\mathrm{m\,s^{-1}}$, $\mathrm{We} = 40$; c) $U_c = 17.11\,\mathrm{m\,s^{-1}}$, $\mathrm{We} = 43$; d) $U_c = 27.34\,\mathrm{m\,s^{-1}}$, $\mathrm{We} = 36$.

Table 4.6: Time stamps for each structures' occurrence for the shear-plume breakup regime.

Structure	t[ms]			
	Jet A-1 100%	Jet A-1 75% - 25% HVO	Jet A-1 50% - 50% HVO	H_2O
1	0	0	0	0
2	5.6	5.6	5.6	4
3	9.6	9.6	9.6	8
4	13.6	13.6	13.6	
5	23.8	23.8	23.8	18.8

This stage was found within the expected range of crossflow velocities, Table 4.7, and did not show an overall difference in characterization when compared to the literatures findings.

Table 4.7: Shear-Plume regime Weber range for all fluids.

Fluid	*Range*
Jet A-1 100%	$40 < \mathrm{We} < 76$
Jet A-1 75% - 25% HVO	$40 < \mathrm{We} < 76$
Jet A-1 50% - 50% HVO	$43 < \mathrm{We} < 79$
H_2O	$36 < \mathrm{We} < 56$

Double-Bag Stage

As stated by [18] a new regime was identified and would be henceforth studied by other authors. It is described by the formation of two consecutive, separate bag creation events. The first is much similar to the Bag-Plume stage, and the plume created is of such magnitude that later in time, because of aerodynamic loading, it starts to deform and create a Bag regime phase. More specifically, it is the occurrence of two regimes in one single droplet. The atomization processes are the same as the two mentioned regimes and produce drops of the same mean apparent size.

The present work will not focus on this regime because of the inability to predict where and when it happens. The authors propose that it occurs between $28 < \mathrm{We} < 41$, yet for both the fuel mixtures and the water it firstly appears for $\mathrm{We} > 40$. Moreover, with the same conditions and flow speeds, some tests produce this event, while others more often do not. This uncertainty in events made the study and the definition of the regimes' thresholds very hard to establish, and Figure 4.5 only qualitatively illustrates this stage.

In a first approach, this regime has two well-defined breakup stages. Firstly, the appearance of an apparently simple and common bag-plume occurrence. This is followed by the plumes' deformation that produces another bag structure, creating as the name indicates the dual bag regime. A simple characterization of this regime and the time intervals are presented only for the Jet A-1 100% case, as follows:

Table 4.8: Dual-Bag time-stamps correspondent to the visualization of this regime for the Jet A-1 100%.

Event	t[ms]
First interaction with flow - undistorted drop	0
Deformed drop - ellipsoid shape evolution	4
Bag and Plume creation	9.6
First Bag breakup occurrence	13.2
Plume inflation into bag structure	22.4
Breakup of all structures	30.4

Total breakup time takes longer to occur due to the additional structures created by the plume. As this is not always observed a more detailed approach to this regime is needed for the present fuel mixtures.

Figure 4.5: Jet A-1 100% example of the Dual-Bag regime.

4.1.4 Shear Stage

Finally, the shear regime ensues with no plume structure. Mass from the edges is continuously stripped from the initial spherical drop, producing small droplets and dispersing them downstream. In some cases the after some time the stripping event deforms the drop in such a way that filaments of liquid are formed creating bigger resulting droplets.

Additionally, breakup mechanisms are apparently more efficient and strong in the atomization process and the cease of fragmentation occurs sooner, as seen in Figure 4.6. The shearing effect also demonstrates a chaotic deformation of the filaments before atomization, with no repeatable structure found other than the initial apparent destruction of the initial drop. This regime is said to be visible between $80 < \mathrm{We} < 350$, before the start of catastrophic breakup. Although, because of maximum flow speed limitation, the threshold of $\mathrm{We} = 350$ could not be exceeded, and required a significant increase in speed.

Furthermore, as referred in Chapter 1, the structures found in the Catastrophic stage are rarely found in most practical spray systems, and due to this consideration, the scope of this work ends with the study of the Shear breakup regime. It is also considered that this stage will no longer be identified beyond $\mathrm{We} > 350$. Thus, this case is found in the ranges shown in Table 4.9.

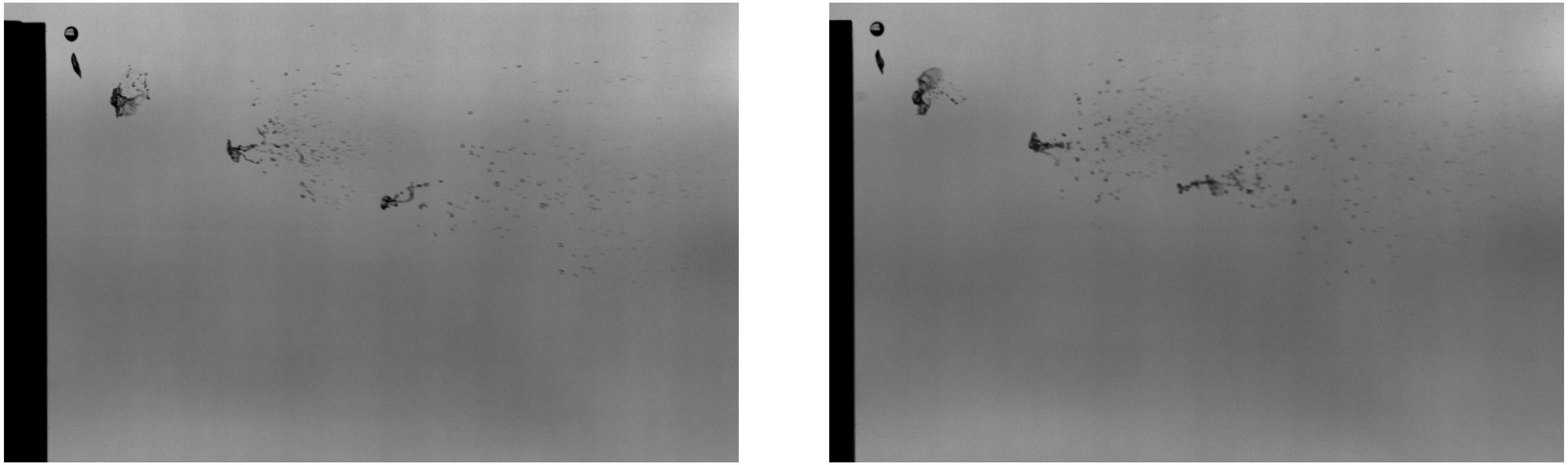

(a) Jet A-1 100%

(b) Jet A-1 75% - HVO 25%

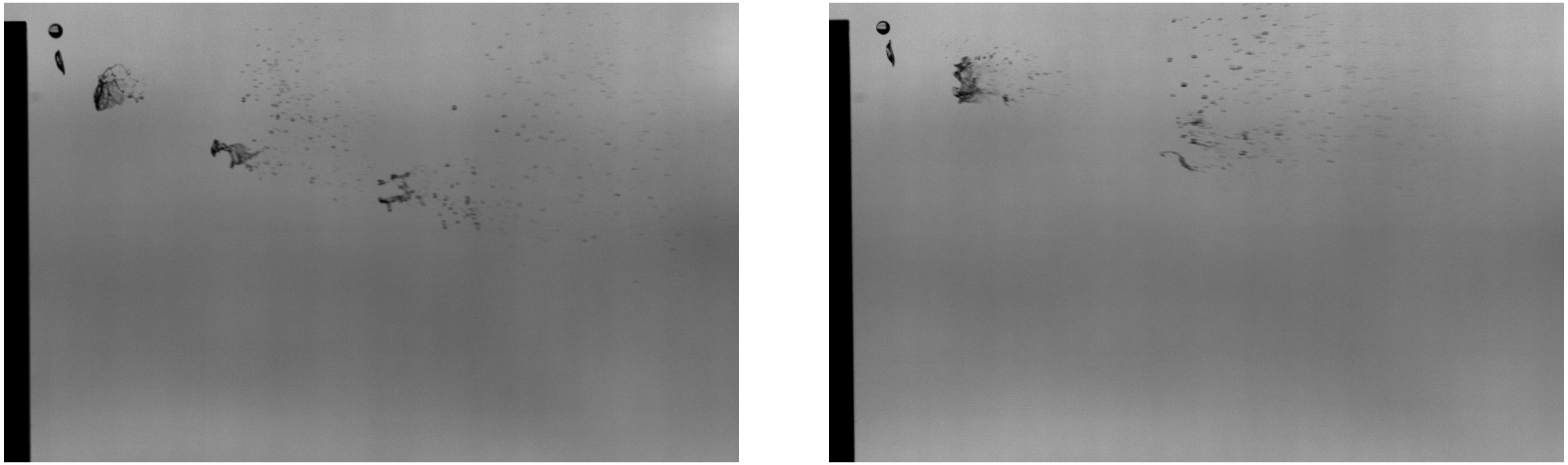

(c) Jet A-1 50% - HVO 50%

(d) $\mathrm{H_2O}$

Figure 4.6: Shear Breakup sequence for the mixtures, captured with the high-speed camera, with mean drop diameter $D_0 = 3\,\mathrm{mm}$ and: a) $U_c = 23.43\,\mathrm{m\,s^{-1}}$, $\mathrm{We} = 76$; b) $U_c = 23.43\,\mathrm{m\,s^{-1}}$, $\mathrm{We} = 76$; c) $U_c = 23.51\,\mathrm{m\,s^{-1}}$, $\mathrm{We} = 34.15$; d) $U_c = 23.88\,\mathrm{m\,s^{-1}}$, $\mathrm{We} = 58$.

Table 4.9: Shear-Plume regime Weber range for all fluids.

Fluid	*Range*
Jet A-1 100%	76 < We < 350
Jet A-1 75% - 25% HVO	76 < We < 350
Jet A-1 50% - 50% HVO	79 < We < 350
H_2O	We > 56

The approach for image composition is similar to the other regimes, taking into account the following events of this regime and time stamps present in Table 4.6.

1. First interaction with flow - undistorted drop
2. Deformed drop - ellipsoid shape evolution
3. Mass Stripping effect
4. Core drop disintegration
5. Further atomization processes

Table 4.10: Time-stamps for each structures' occurrence for the shear breakup regime.

Structure	t[ms]			
	Jet A-1 100%	Jet A-1 75% - 25% HVO	Jet A-1 50% - 50% HVO	H_2O
1	0	0	0	0
2	3.2	3.2	3.2	2.8
3	7.2	7.2	7.2	6.8
4	13.2	13.2	13.2	
5	19.2	19.2	19.2	12.8

The water experiments continue to show discrepancies when compared to the fuel mixtures and literature. Weber number is a ratio between disruptive forces and stabilizing surface tension forces $(\rho_g D_0 U_r^2)/\sigma$, and as water has a surface tension greater in a factor of approximately three fold, as the drops' initial diameter is reduced, the relative velocity necessary to cause the aforementioned regimes need to be ever greater. For example, for the case of a $3\,\mathrm{mm}$ Jet A-1 drop to achieve the bag regime, a relative velocity of $U_r \approx 12\,\mathrm{m\,s^{-1}}$, while for a water drop of the same diameter it needs $U_r \approx 17\,\mathrm{m\,s^{-1}}$. This is the reason behind the great differences in Weber number thresholds for each regime. So, if one wants to take into account the same values, a bigger D_0 for the water drop is needed.

4.2 Transitional Drop Characterization

Upon the visualization of each regime, there is a need to describe the drop in accordance to the non-dimensional groups. Considering the drops diameter and properties Ohnesorge number is obtained and the drops' velocity components at the onset of breakup initiation provide the necessary information to calculate the Weber numbers. This section will present and analyse these concepts and couple them with each respective regime, as seen, for example, for the Weber number ranges in the visualization section.

4.2.1 Ohnesorge Number

The Ohnesorge number takes advantage of the drops initial diameter and the ratio of viscous to surface tension forces, facilitating the characterization of the drops size, and at the same time creating a concise difference between fluids. As seen in Table 4.11, the same diameter produces different characterizations of Oh due to the difference in properties.

Table 4.11: Properties of the fluids used in the present work and Ohnesorge number determination.

$Fluid$	$\mathrm{D_0}$ [mm]]	$\mathrm{Oh} \times 10^3$
Jet A-1 100%	3.1	4.5
Jet A-1 75% - 25% HVO	3.1	5.7
Jet A-1 50% - 50% HVO	3.1	7.3
$\mathrm{H_2O}$	3.0	2.2

So, while examining the parameters presented in the next subsections, there is less confusion and the characterization of each fluid can be done almost effortless. The variation of this non-dimensional group is also used for a better representation of the viscous forces present on each fluid. If Oh assumes a large value, a big influence of μ is implied. However, $\mathrm{Oh} < 0.1$ already represents a point of negligible viscosity influence, therefore as Ohnesorge number ranges from $2.2 \times 10^{-3} < \mathrm{Oh} < 7.3 \times 10^{-3}$, it is safe to assume that viscosity will not have a significant influence on the breakup phenomena.

4.2.2 Weber and Reynolds Numbers

The Weber number uses relative velocity between drop and flow to create a non-dimensional ratio between disruptive forces to stabilizing surface tension forces. This parameter also takes into account the drops diameter, but as only its' surface tension force is included within this ratio, the characterization is not as strict as the aforementioned one. This fluid property is a way to understand how the drop behaves when affected by a cross-flow, and with a constant drop diameter, the influence of this parameter can be seen to be a great factor in the Weber number determination.

Table 4.12 is a representation of flow and drop velocity components determination, relative velocity calculation and ultimately Weber and Reynolds number determination. The Reynolds number is also calculated because of the close relation with both Weber and Ohnesorge numbers and is of some interest for the characterization of each regime and fluid. The velocity components are mean values of three tests and measurements for each fluid and regime, measured right before the creation of any breakup structure.

Taking into account regime transitions, vertical velocity variation values for the fuel mixtures display little variations with a very small decrease of this parameter from the Deformation $\rightarrow$ Bag through the last regime transition. Horizontal velocity components display some rather curious variation with no clear patterns being observed within each regime, except the water experiments for the first three transitions where U_{d_x} is higher than the fuel mixtures. The Shear-Plume $\rightarrow$ Shear transition exhibits a lower value of this parameter for the water.

In short, in an ideal situation, vertical velocity should decrease with a flow speed increase, while the horizontal velocity component should increase. The latter case is observed for the fuel mixtures, while their value for the water experiments decrease. Nonetheless, effective drop velocity remains essentially constant through all regime transitions with a value of $U_d = 2.01\,\mathrm{m\,s^{-1}}$. These values also have a small influence on relative velocity variation, with a clear similarity to the flow speed increase.

As for We and Re, their values increase alongside the cross-flow velocity magnitude with the exception of the $\mathrm{H_2O}$ cases that will be explained next. Although one can state the relative and flow velocities display very close and similar values, for precision and error mitigation purposes, the correspondent vertical and horizontal components are not neglected. Thus, the calculation of the non-dimensional groups can be done with higher confidence.

Table 4.12: Characterization of the drops velocity components, diameter and surface tension, air density and viscosity and resulting Weber and Reynolds numbers.

Regime	*Fluid*	$\mathrm{U_c[m/s]}$	$\mathrm{U_{d_y}[m/s]}$	$\mathrm{U_{d_x}[m/s]}$	$\mathrm{U_d[m/s]}$	$\mathrm{U_r[m/s]}$	We	Re
Deformation → Bag	Jet A-1 100%	9.29	2.06	0.35	2.06	9.17	13	1886
	Jet A-1 - HVO 75% - 25%	9.64	2.00	0.46	2.06	9.40	13	1933
	Jet A-1 - HVO 50% - 50%	9.81	1.99	0.48	2.05	9.54	14	1963
	$\mathrm{H_2O}$	18.84	1.97	0.77	2.12	18.17	17	3605
Bag → Bag-plume	Jet A-1 100%	12.06	1.94	0.54	2.02	11.68	20	2402
	Jet A-1 - HVO 75% - 25%	12.21	1.94	0.51	2.01	11.86	21	2439
	Jet A-1 - HVO 50% - 50%	12.06	1.88	0.62	1.98	11.59	21	2384
	$\mathrm{H_2O}$	23.88	1.90	0.72	2.03	23.24	27	4462
Bag-Plume → Shear-Plume	Jet A-1 100%	16.90	1.88	0.65	1.98	16.35	40	3363
	Jet A-1 - HVO 75% - 25%	17.00	1.83	0.69	1.96	16.42	40	3376
	Jet A-1 - HVO 50% - 50%	17.11	1.90	0.44	1.95	16.79	43	3453
	$\mathrm{H_2O}$	27.34	1.86	0.67	1.97	26.73	36	5305
Shear-Plume → Shear	Jet A-1 100%	23.43	1.78	1.05	2.06	22.45	76	4678
	Jet A-1 - HVO 75% - 25%	23.43	1.80	0.91	2.02	22.60	76	4648
	Jet A-1 - HVO 50% - 50%	23.51	1.71	0.87	1.93	22.70	79	4669
	$\mathrm{H_2O}$	34.15	1.84	0.52	1.91	33.68	58	6682

4.3 Fluid properties influence on the variation of Weber number

The ultimate way to characterize the drops' behaviour and regime manifestation is plotting Oh with We. As seen before, although the initial diameter of the drops is the same, its properties influence the deformation due to a cross-flow. For this, correlations proposed in the literature are used to verify if the new set of mixtures display a good agreement with past results and different fluid mixtures.

Figure 4.7 is an illustration of said correlations with the experimental results obtained. For this case, Bag, Bag-Plume, Shear-Plume and Shear regimes are respectively identified using squares, circles, triangles and deltas. The colour scheme is as follows:

- Black - Jet A-1 100%
- Blue - Jet A-1 75% - 25% HVO
- Red - Jet A-1 50% - 50% HVO
- Green - H_2O

For the fuel mixtures the Weber increase is seen, even if slightly, and the transitions of these seem to fit well with those proposed for other fluids. The Shear Regime is the only discrepancy, yet is of little significance, as the transition is not a well-defined boundary, and merely a compromise found from other studies. Nonetheless, the results are rather satisfying, and there is no major difference in the use of a new set of mixtures. For the water experiments there is a more steady increase in regime transitions. While in the fuel experiments regime occurrence range appears to have an ever increasing fashion, the water ranges seem more condensed.

As explained before, the use of a small droplet influences the ability for an on-coming flow to disrupt the surface tension of this fluid beyond its critical point. If one continued to reduce the initial diameter, the cross-flow velocities necessary to induce breakup mechanisms would be even higher.

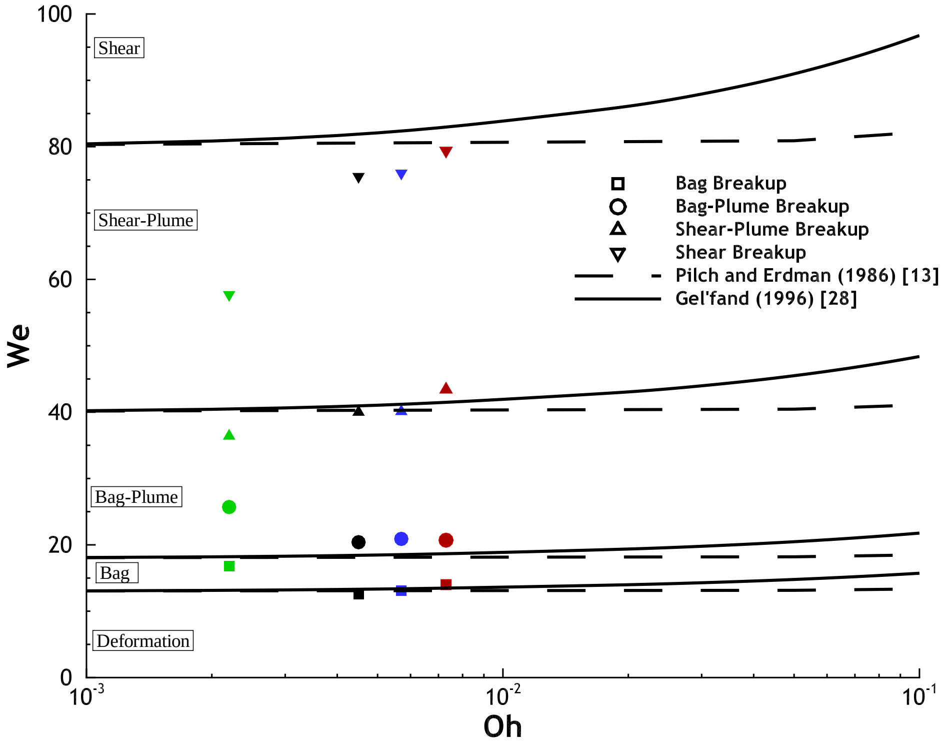

Figure 4.7: Variation of Weber number for each fluid mixture (Oh).

This can be seen in Figure 4.8, where the increasing trend of the fuel mixtures is clearly grater that the water experiments. This graphic was produced to aid the visualization of flow influence on the different properties that compose the fluids. Density of these does not vary greatly, one can assume a determinative factor is the great difference of surface tension. The fuel mixtures have similar surface tension and their increase is practically the same.

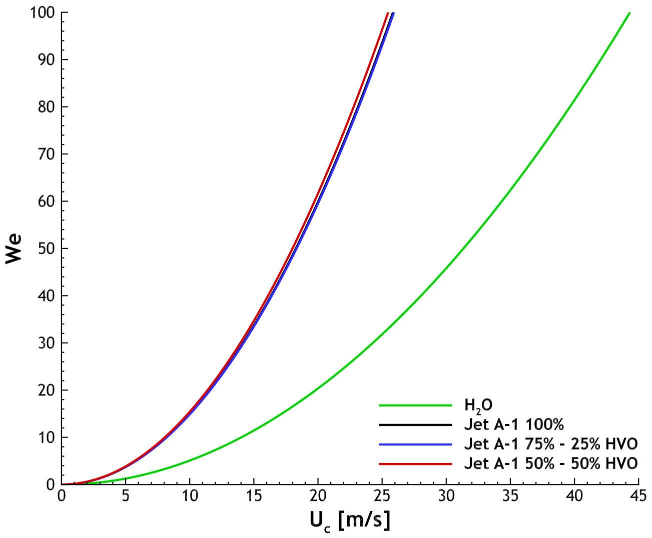

Figure 4.8: Weber number due to variation of crosstream velocity.

4.4 Cross stream diameter

The first stage of all the breakup regimes is a deformation of the spherical drop into a disk shape (oblate ellipsoid) due to its interaction with the crossflow. The non-dimensional groups, Weber and Ohnesorge numbers, are a big factor on the behaviour of the drops' deformation and will be thoroughly studied in this section.

4.4.1 Maximum cross stream diameter due to Weber number

One can state, in a first approach, the increase of flow speed will also increase the maximum cross stream diameter. This is not a good assumption because, as seen before, different structures are created and the main cause is the flow around the drop. Literature presents a constant trend after a slight increase of this parameter. The maximum cross stream diameter, D_{max}, is normalized by the drops initial diameter D_0, thus yielding ε for simplification purposes.

In a first approach, for the bag and bag-plume there is, in fact, an increase of ε with the increase of We. The constant trend proposed after this is not verified for the last two regimes which, contrary to expected, show a decreasing trend, Figure 4.9. This diameter is measured the instant in time before any breakup structures, i. e., bags, plumes or stripping effects, start to appear. The decrease of this value on the last two regimes is due to the mass stripping effect. The growth of ε is similar in all regimes, but at a defined point in time, mass starts to eject from the edges of the drop. The difference between the decrease of this parameter and the constant correlation proposed by other authors can be explained, once again, due to the surface tension values but even the water experiments illustrate the same behaviour as of the fuel. Albeit, the constant trend might be an erroneous prediction and the application in computational models can produce undesired errors. Nonetheless, the bag regime demonstrates the same diameter for all the fluids while the shear-plume and shear show values close within each regime. Bag-plume regime shows big differences and the number of experiments is not enough to determine the reason for these.

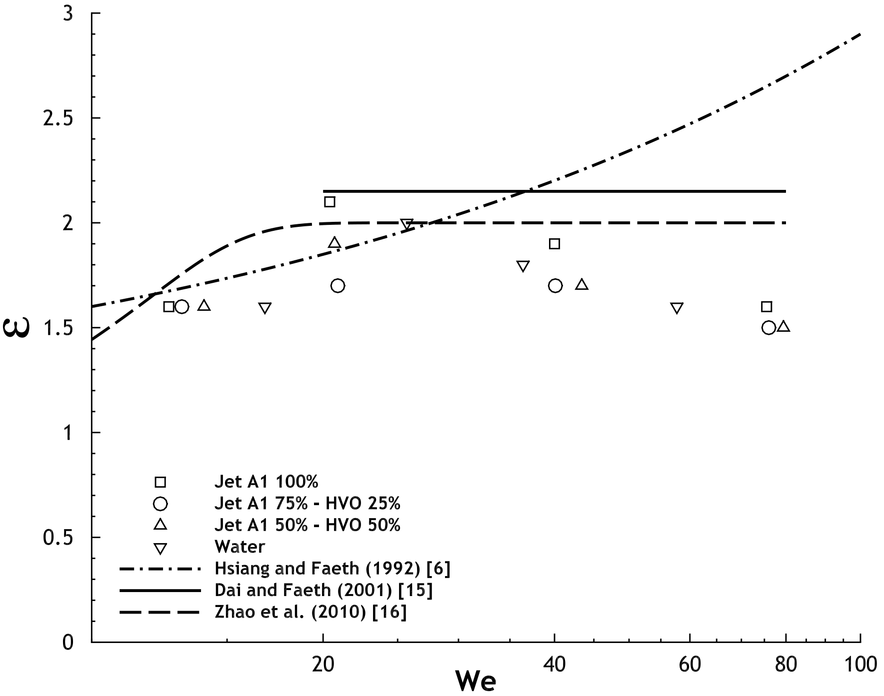

Figure 4.9: Variation of the maximum cross stream diameter for different regimes (different We).

4.4.2 Maximum cross stream diameter due to Ohnesorge number

After the influence of the flow in drop deformation is studied, an Ohnesorge number based influence is studied to determine if there are any significant differences between fluids. As assumed, there is no clear evidence of viscosity interference on diameter variation.

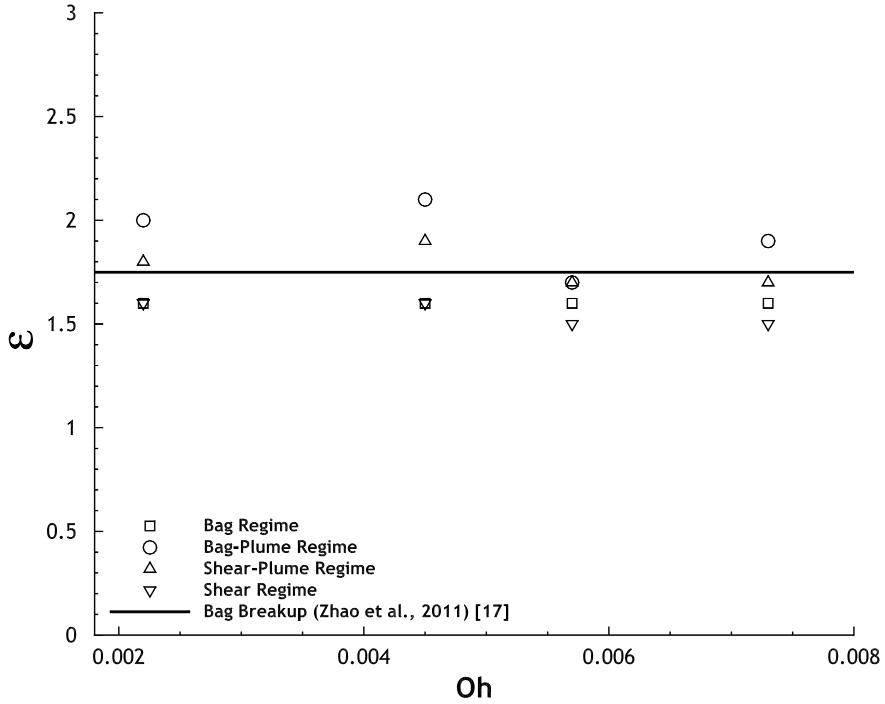

Figure 4.10: Variation of the maximum cross stream diameter for different fluids (different Oh).

The results shown in Figure 4.10, show no specific trend and appear revolve around the constant threshold proposed by [17] for the bag regime. Although in the authors' work, the constant value is attributed to the Deformation → Bag regime transition, present results do not agree with the premise that $\varepsilon = 1.75$ is a threshold line between these regimes.

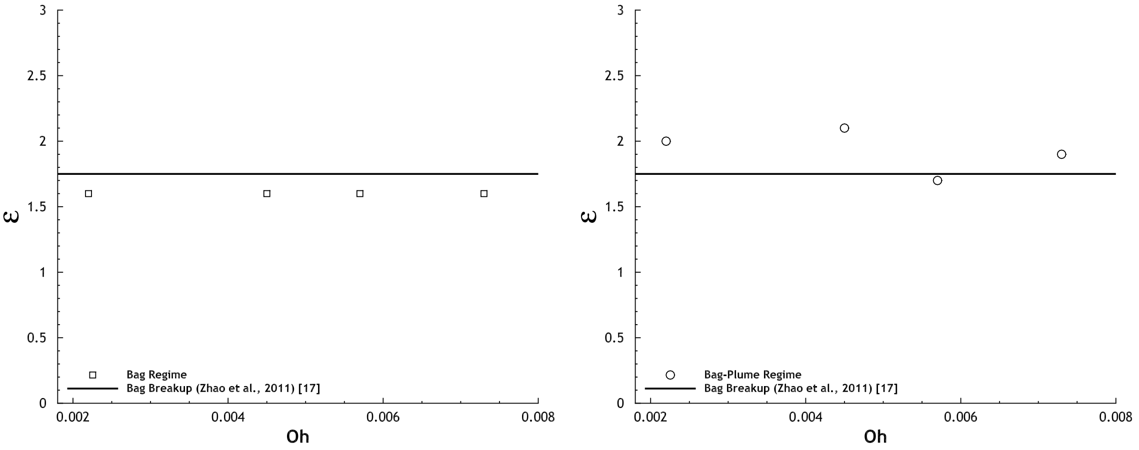

(a) Bag Regime (b) Bag Plume Regime

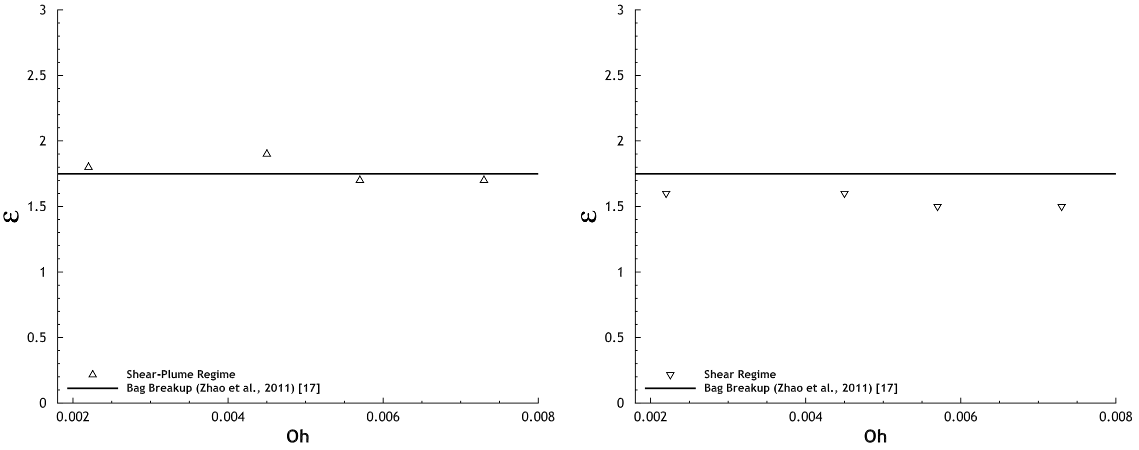

(c) Shear Plume Regime (d) Shear Regime

Figure 4.11: Variation of the maximum cross stream diameter for different fluids (different Oh) and each regime.

A more detailed and relevant analysis is presented in Figure 4.11, where each regime is treated separately. Using Zhao et al.'s equation as a reference [17], results obtained in the bag regime demonstrate a deviation from the constant reference with $\varepsilon = 1.6$ for this stage. The shear regime also presents lower ε values, with a mean value similar to the first regime. Regimes containing a plume appearance revolve around the constant line.

Not only do the present experiments disagree with the threshold between deformation and bag regimes, but all other regimes also seem to have no defined transition line between each other. Moreover, one could state that Zhao et al.'s proposal can be seen [17], not as a transition point, but as a mean maximum cross stream diameter value for all these regimes. The value proposed, $\varepsilon = 1.75$, has an almost perfect fit for maximum diameter variation of this dissertation.

4.5 Time-based approach to the breakup phenomena

Once the initial drop deformation is studied, along with the structures created in each variation of Weber number, a time based approach is needed to compare the events and at which point these occur. The non-dimensional time characterization is important since the time-stamps present in these experiments are very small. For Section 4.1, this approach is not employed since it is a qualitative description of the breakup events. Time intervals presented are a way to inform the reader that the structures are captures at the same expected time of appearance. This section will use the non-dimensional characterization of time and compare the present results with the literatures' correlations.

4.5.1 Breakup initiation time

The first big event on the breakup phenomena is the initiation of breakup structures' formation. So, the time elapsed since the drops' first interaction with the flow to the first appearance signs of different structures is called the Breakup Initiation Time, τ_{ini}. Assuming this is when the drops have a maximum cross stream diameter is not correct. After the point of maximum ε, this value remains somewhat constant for a very brief time interval before the appearance of breakup structures.

Coupling this parameter with the variation of Weber number, Figure 4.12, one can identify a slight decrease of τ_{ini} as We increases. With a more cautious verification, the evolution of τ_{ini} appears to increase very slightly for $\mathrm{We} < 20$, while for $\mathrm{We} > 20$ there is, in fact, a decreasing trend. Plotting against Pilch and Erdmans [13] equation, the decreasing trend is similar but presents higher values as the flow speed is increased.

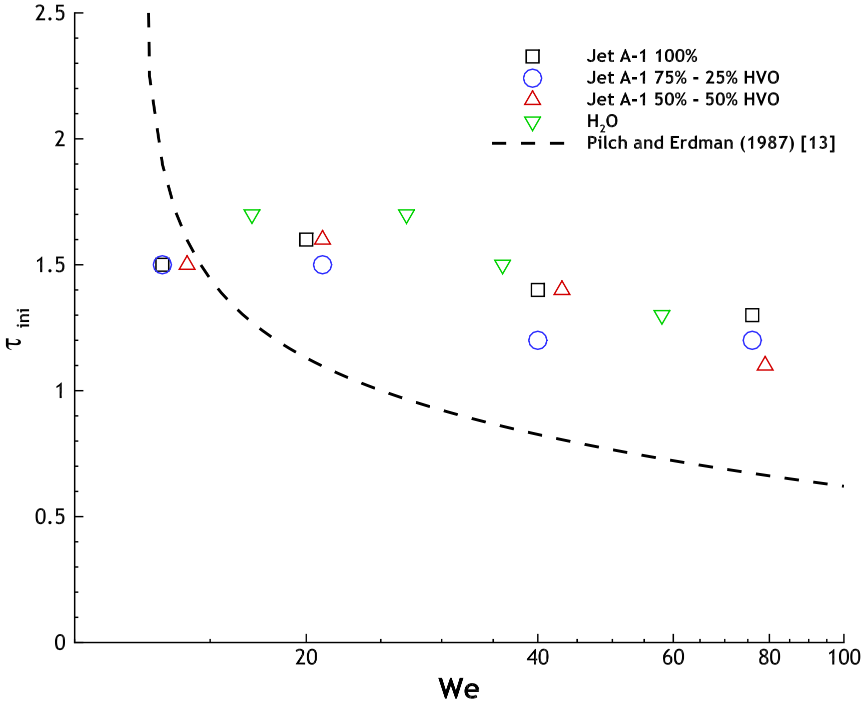

Figure 4.12: Regime based Breakup initiation time for all fluids.

Secondary atomization occurs after a certain threshold is overcome, and so the existence of an asymptote is expected and the ever decreasing line is an acceptable consideration within the literature. The first experiments agree very well with the curve and a continuing decrease is expected. Instead, the bag-plume regime shows higher initiation time values followed by the decrease expected before.

In the other hand, plotting these values with the Ohnesorge number shows a different scenario, Figure 4.13.

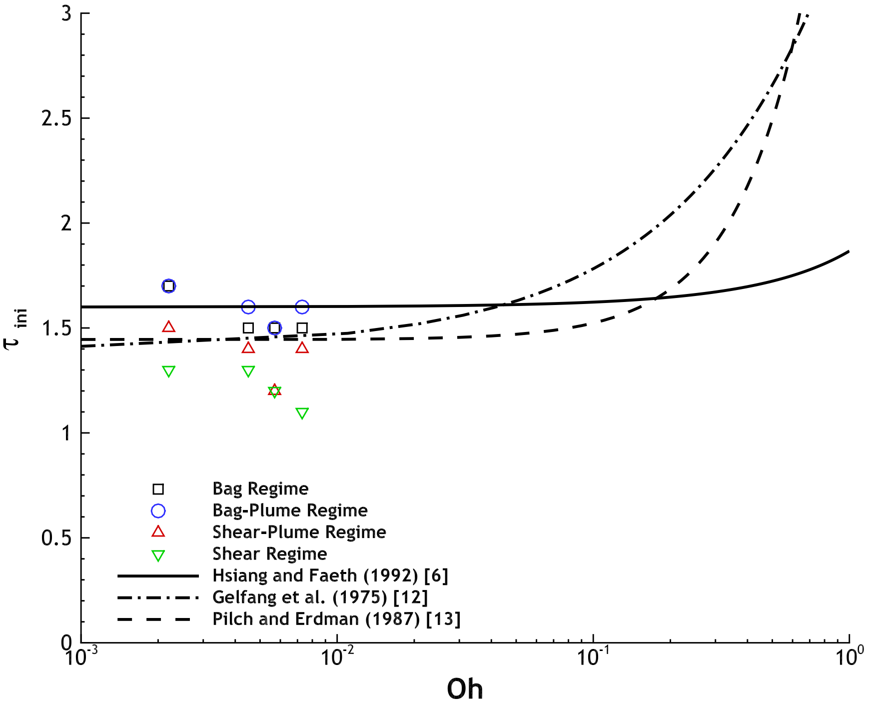

Figure 4.13: Fluid based Breakup initiation time for all regimes.

All the breakup regimes, with the exception of the Shear regime, show reasonable agreement with the correlations proposed for all the fluids. It is visible that Hsiang and Faeth's [6] curve is a very good fit for the bag regime results. The correlations proposed by Pilch and Erdman and Gelfand et al. [12, 13] also fit very well with the bag-plume and shear-plume results. While the shear regime results are close to the latter's correlations, its' mean value is lower than those of other regimes and do not fit as good. One can also assume that for the present volume of experiments performed, and values obtained, the results appear rather acceptable within past results, and so no big differences are encountered.

4.5.2 Total breakup time

Once all breakup phenomena have ceased, the total breakup time is reached, measured since the first drop-flow interaction and the increase of flow speed can hint to a decrease in total breakup time, τ_{tot}. In spite of this assumption, the creation of different structures also greatly influences the rate of deformation and fragmentation. Bag structures will suffer secondary atomization significantly faster than plume or liquid filaments and produce smaller fragments. As seen in the case of the Dual-Bag regime, the creation of a bigger plume gives way to the initiation of another bag structures' atomization, increasing the total breakup time. Past results propose a quite complicated relation between Weber number and total breakup time. The first major decrease in breakup time ends with the beginning of the bag-plume regime. A slight linear increase follows until half-way through the shear-plume regime, and enters a decreasing stage once more for the remainder of this and the shear regime.

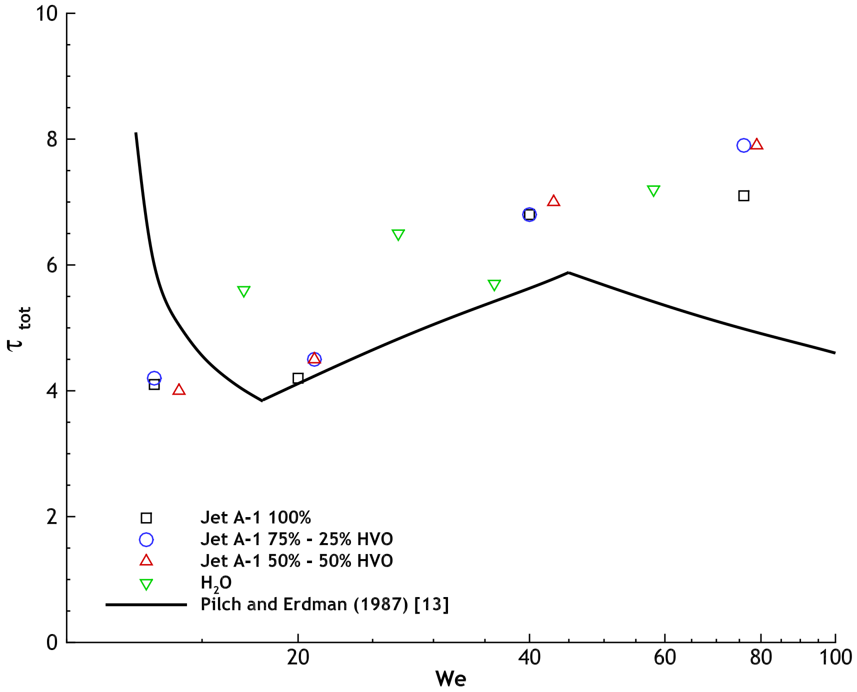

Figure 4.14: Regime based total breakup time for all fluids.

Plotting these correlations with the results obtained, a good agreement is found for the linear increase, while for the first steep decrease do not fit well within the curve. For the shear stages an ever increasing time value is encountered, contrary to the relation proposed by [13], Figure 4.14. The water experiments show a very big variation of its total time value when compared to the other fluids, for the first three regimes. As per usual, surface tension plays a big role in resisting secondary atomization, with bag and bag plume regimes appearing to be the ones that suffer mostly from this fluid property. On the shear-plume regime analysis, the remaining plume after mass stripping phenomena has a similar volume and size to those of other fluids, and because of the surface tension value it does not undergo further atomization, being the reason the total breakup time values are lower.

Taking into account the results plotted against Ohnesorge number, a different paradigm rises, Figure 4.15. Even though the proposed correlations are similar to the initial breakup time and with a positive translation of the $y - direction$ values, the results show a big and chaotic scatter, with no apparent fit. For the Jet A-1 100% and Jet A-1 75% - HVO 25% mixtures and the Bag, Bag-Plume and Shear-Plume regimes, τ_{tot} values are slightly lower than the proposed curves, yet for the rest of the fluids and regimes, total breakup times occur at much higher values than those proposed. The fluids properties might be responsible for this representation but the scatter seems to be random and independent of the fluid used in the test.

Contrary to what is presented in Section 4.1, the total breakup time values for the water are higher compared to the fluids. The difference between the representation of the breakup phenomena presented in the previous section and the present one is the ceasing of all atomization

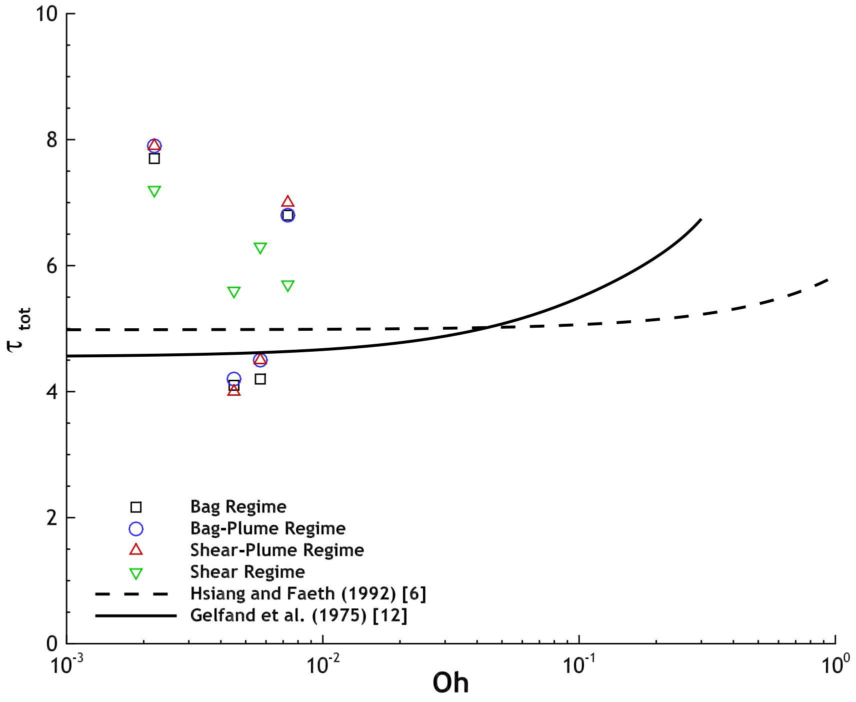

Figure 4.15: Fluid based total breakup time for all regimes.

processes. As said, τ_{tot} represents the point in time where no more drops suffer secondary atomization, and although the water experiments present faster occurrences of each structure, the small drops created can suffer further breakup because of their size.

4.5.3 Time-wise evolution of ε

The interaction of flow with the drop during its deformation, and until maximum diameter is reached, causes a change in drag coefficient inherent to the drops' shape. As known, the C_D of a spherical object is different from that of a disk, and aerodynamic loading is not constant and immediate. The characterization of the drops cross-stream diameter allows a better understanding of the shape evolution while also being a valuable asset for implementation in drag coefficient determination on computational models.

Firstly the characterization of the drops behaviour for each fluid is done separately, grouping all regimes and trying to find a difference or relation with the increase of flow speed, Figure 4.16. Once all the fluids and regimes were plotted, a certain similarity between all of the crosstream evolutions is found. The maximum diameter increase seems to occur in an approximate magnitude for all regimes, and with further visualization, for all the fluids. It is also seen, as expected, that the increase is not linear, presenting an almost constant evolution in the primordial stages of deformation followed by a non-linear increase.

The need to group all these experiments into one plot is evident, Figure 4.17. Since the literature proposes correlations for specific regimes, it is also of importance to verify these and compare them with the present results. The linear increase proposed in the earlier stages of aerodynamic breakup studies is somewhat erroneous, with authors later proposing different corrections with this consideration. Exponential increases are proposed as well as a two stage correlation with a constant initial value followed by a linear increase.

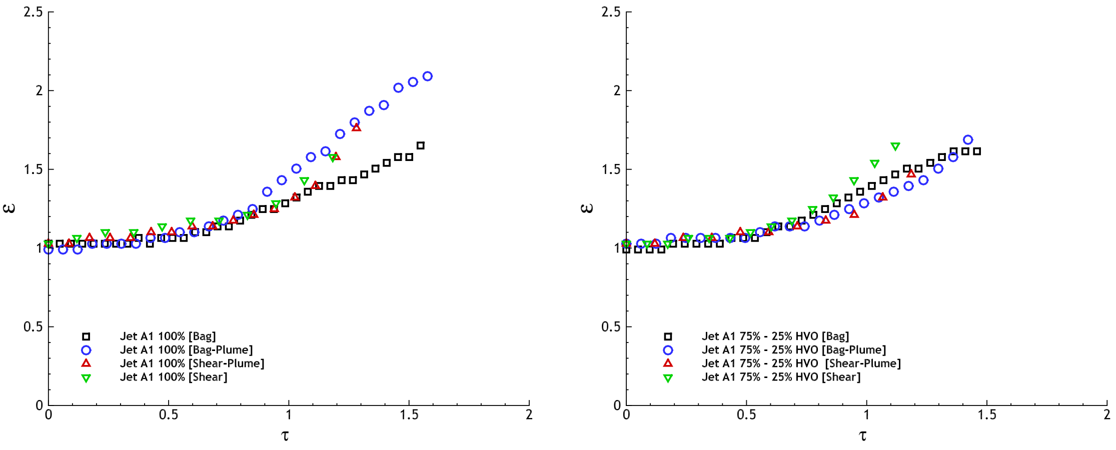

(a) Jet A-1 100%

(b) Jet A-1 75% - 25% HVO

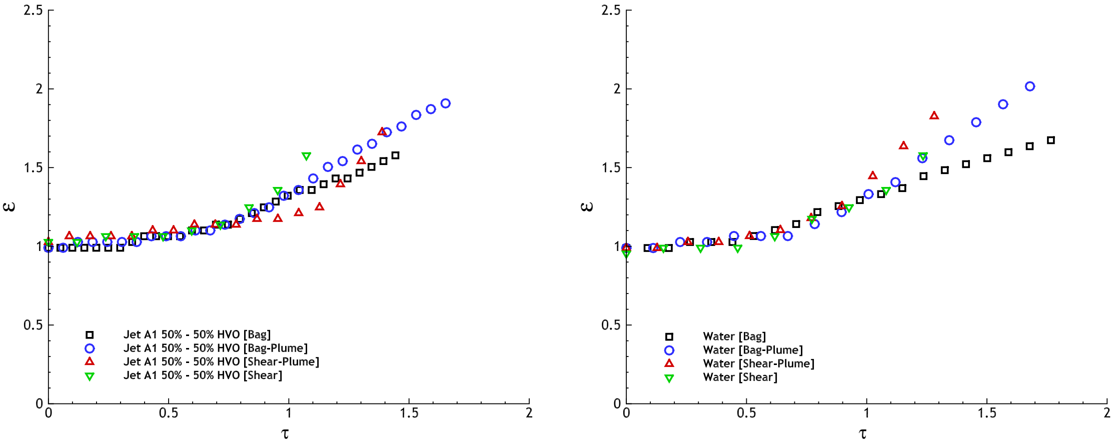

(c) Jet A-1 50% - 50% HVO

(d) H_2O

Figure 4.16: Time-wise variation of the maximum cross stream diameter for different fluids.

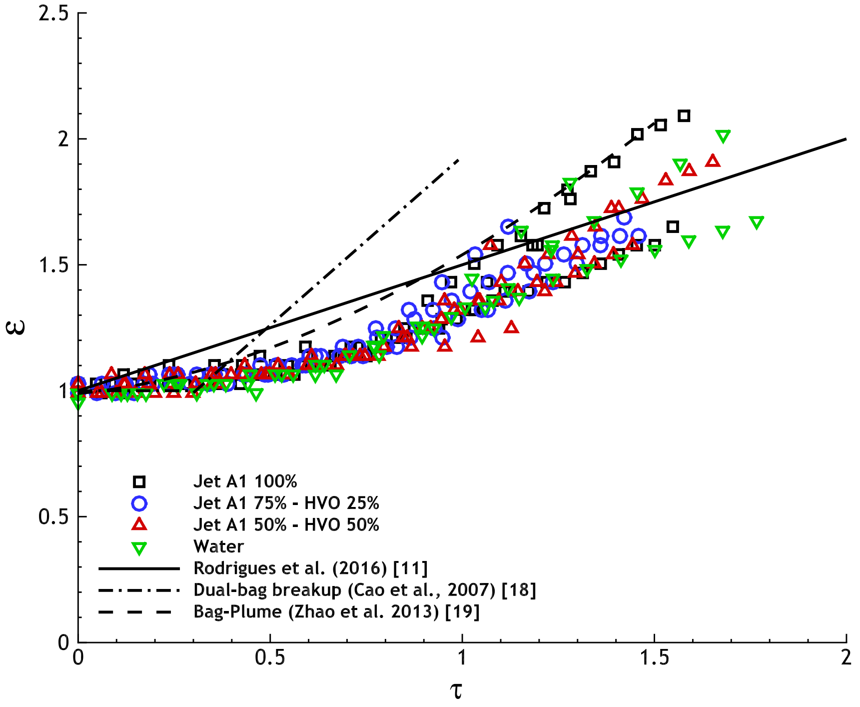

Figure 4.17: Time-wise variation of the maximum cross stream diameter for all the experiments.

The correlation proposed by Zhao et al. [19] demonstrates some deviations from the present results, only predicting some of the initial values with accuracy. It also lies well with the late evolution of the Bag-Plume regime for Jet A-1 100%, yet fails to describe this regime for the other fluids. Although the Dual-Bag regime is not presented in this characterization, once there is evidence that correlations can be fitted to all regimes, the verification of this premise is necessary using the one proposed by [18]. For the initial values it fits well within the results, but the fast linear increase demonstrates a very rapid occurrence of the maximum cross stream diameter, which is not found for any test.

So, with the amount of data collected for these fluids and regimes, the present work suggests a correlation of the cross stream time-wise evolution, Eq. 4.1 that takes into account an approximate mean value of all the results obtained.

$$\varepsilon = 1 + 0.3\tau^{2.35} \quad , \tau < 2 \qquad (4.1)$$

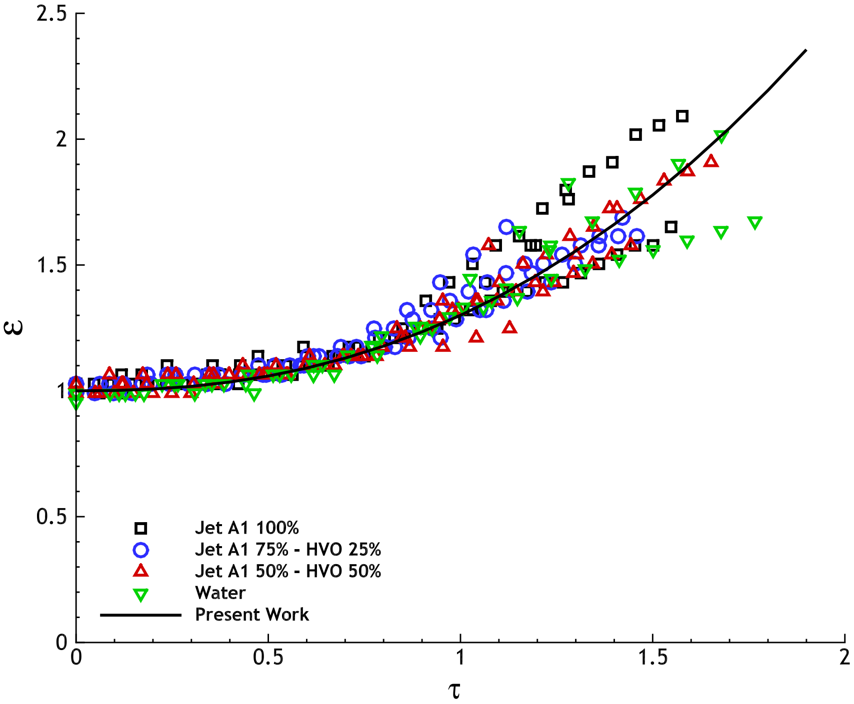

Figure 4.18: Time-wise variation of the maximum cross stream diameter for all the experiments plotted with the proposed correlation Eq 4.1.

As seen, the expression embraces all the experiments and can be an acceptable fit enabling a more precise approach to the drag coefficient determination for the different stages and drop shape. The water experiments do not present a systematic and noticeable difference from the other mixtures, leading to the assumption that all drops have the same mechanism intrinsic to their deformation until maximum cross stream. It is important to also refer, that for this subsection, the actual maximum diameter achieved by each drop is not taken into account, and only the evolution is studied.

4.6 Drop Trajectory

The study of the drops position in space from the moment of its insertion in the flow is done by a centre of mass approach. The determination of the centroid is as described in Chapter 3. Combustion chambers have finite boundaries and breakup needs a certain amount of time and space to occur otherwise the non-atomized drops enter impact regimes. This subsection, however, only focuses on the regime and fluid based differences of each trajectory.

The measurements also take into account the drop until the first appearance of secondary atomization, contrary to the breakup initiation time considerations. Similar to past works, the mean drop dispersion is deemed important in all the atomization process, while τ_{ini} is used as a threshold before the initiation of different regimes and structure manifestation. Moreover, the present threshold consideration for drop trajectory is due to the tremendous difficulty to identify all the small drops created by secondary atomization, using developed MatLab™code, because of the blurriness in the high-speed camera images. As these are not in the same plane as the initial drop due to spacial scatter, the identification of the product drops becomes increasingly more difficult.

The fluid behaviour due to the increase of cross-flow speeds is illustrated. The various regimes resultant from this variation are presented with the respective trajectories.

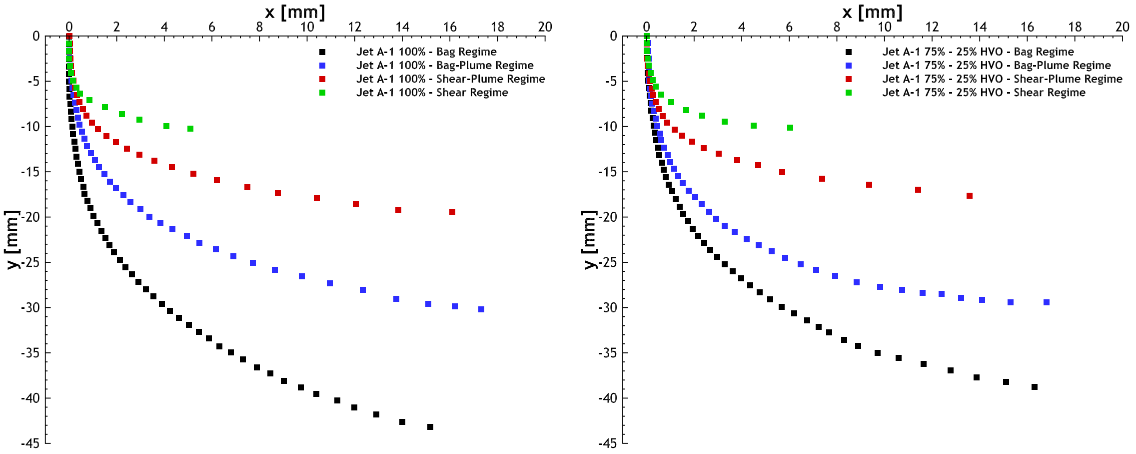

(a) Jet A-1 100%

(b) Jet A-1 75% - HVO 25%

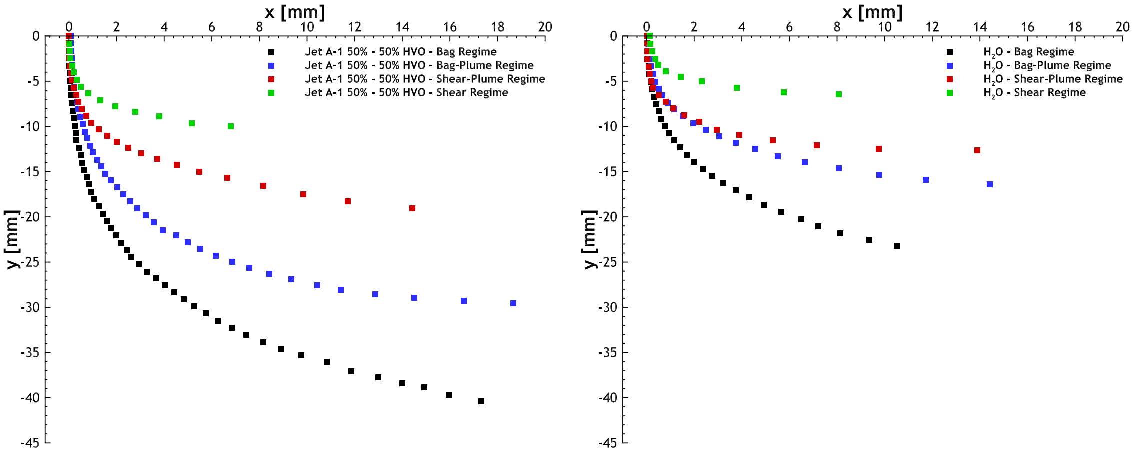

(c) Jet A-1 50% - HVO 50%

(d) H_2O

Figure 4.19: Spacial drop trajectory, where y is the gravity force direction and x is the mean flow direction in millimetres, on a fluid based approach.

On one hand, Figure 4.19 demonstrates an expected tendency on the difference in trajectories due to cross-flow speed variation. The drops horizontal velocity component increases, while the vertical velocity component decreases and as seen above, the main velocity remains essentially constant for the point of maximum diameter. This is also the case for the different positions of the drop and leads to a shift in trajectory. As a consequence, the vertical travel distance is shortened, while for this case the horizontal distance is dictated by the start of secondary atomization. Despite this verification one can notice a systematic variation of x between regimes, where the travel distance increases from the bag regime to a maximum in the bag-plume, whereas the distance decreases from the bag-plume to the shear-plume and furthermore for the shear regime. These variations, although visible for all fluids, do not have the same magnitude, and a relation is not easy to be obtained. Albeit, the trajectories appear agreeable with those found in the literature, yet due to the inability to obtain certain computational and mathematical correlations, the present trajectories could not be directly compared.

On the other hand, one can notice a great deviation from the water experiments in comparison with the fuel mixtures, while there is also a very small difference between the Jet A-1 100% and the other fuels in the bag regime, yet it does not seem to be of a significant factor, and a variation in the centroid determinations is assumed, Figure 4.20.

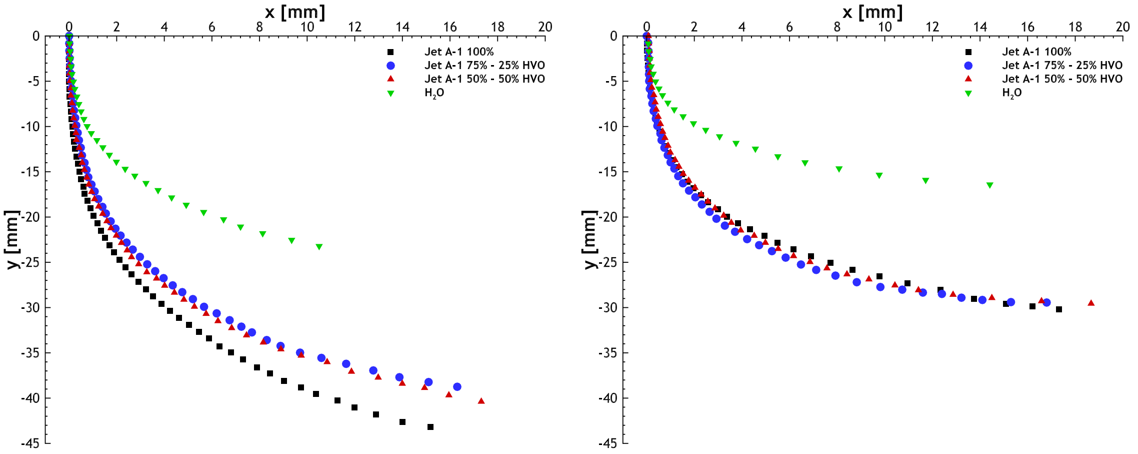

(a) Bag Regime

(b) Bag-Plume Regime

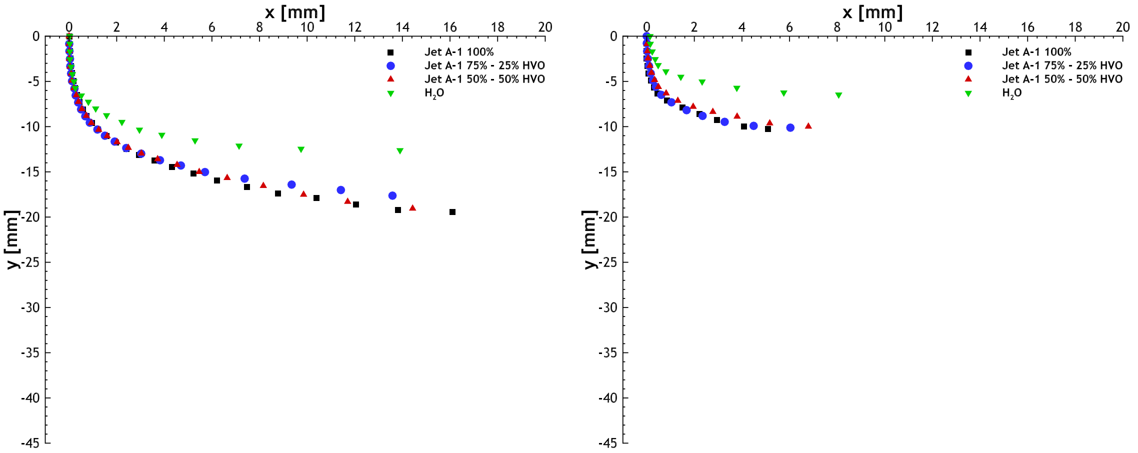

(c) Shear-Plume Regime

(d) Shear Regime

Figure 4.20: Spacial drop trajectory,where y is the gravity force direction and x is the mean flow direction in millimetres on a regime based approach.

The fluids have practically the same trajectory variation, yet the water has a much smaller vertical and horizontal travel interval. Once again, the surface tension comes into account, as explained before. Since the flow speed in the water experiments has a higher value, the travel distance is shortened and influences the interpretation of this phenomena. Also because of this, the point of first breakup occurrence is higher in the shear regime for the water than the fuel. Fuel mixtures also present a very close horizontal travel distance within the same regime and do not illustrate significant property influence in trajectory.

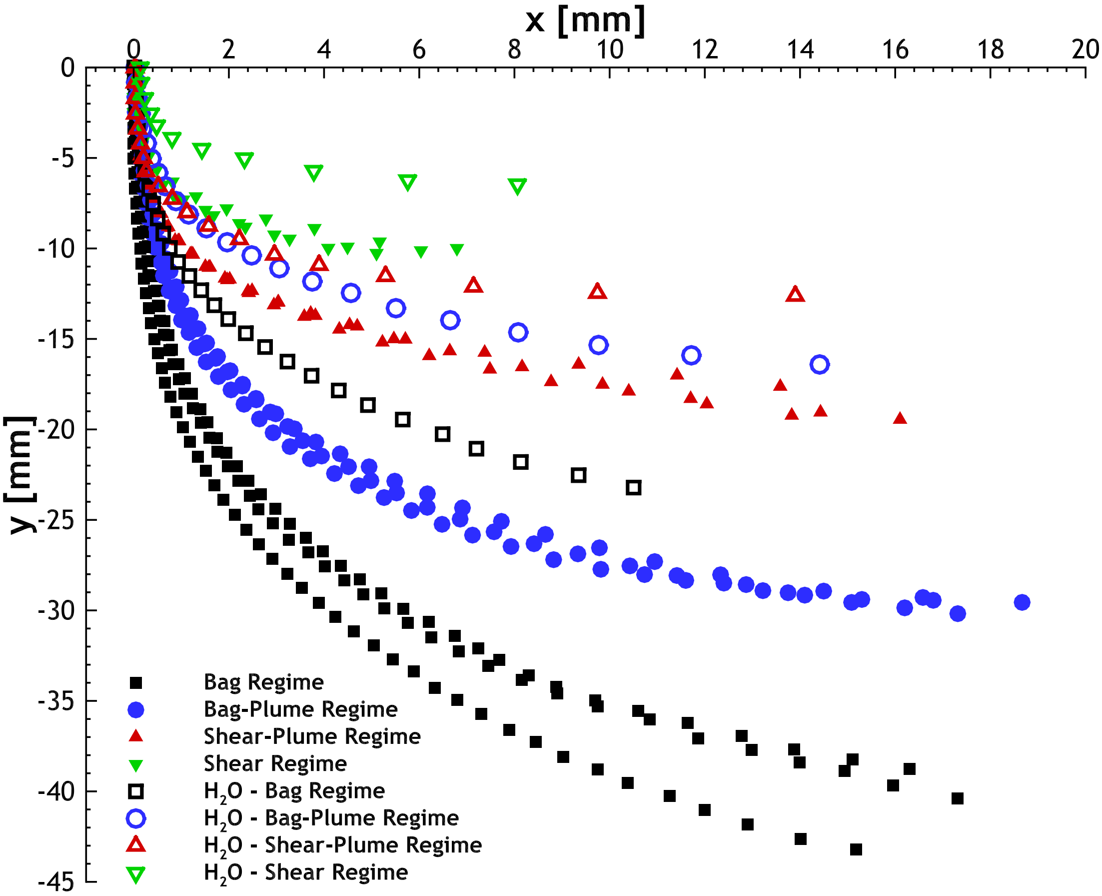

Figure 4.21: Spacial drop trajectory for all the fluids and different regimes.

Finally, when plotting all fluids and regimes, the spacial trajectory distribution of the water droplets is rather odd. The Bag regime for this fluid appears between the Bag-Plume and Shear-Plume regimes for the fuel mixtures, while the Bag-Plume and Shear-Plume regimes appear between the Shear-Plume and Shear regime mixture's trajectories. The waters Shear regime is the one that travels the lesser distance vertical distance of them all.

4.7 Summary

The study of drop dispersion, coupled with the images from Section 4.1 allows the assessment of the experimental facility's construction validity. The black rectangle present in every image is the tunnel's exit nozzle and the camera captures roughly $85\,\mathrm{mm}$ of its height, from the upper boundary. Also, with Figure 4.20 one can verify the maximum vertical displacement of a drop occurs for the Bag Regime and Jet A-1 100%, and it accounts for a value of approximately $45\,\mathrm{mm}$.

With this said, the tunnels exit nozzle can be used in cases where the drops vertical velocity is higher than the present experiment, while still having every breakup regime occurring within the uniform flow region, meaning the tunnel serves it's purpose.

The injection system guarantees the formation of a single droplet, eliminating drop interaction in the flow field. Furthermore, using a syringe diffuser helped control the amount of fuel waste present in each test, and the flat-head needles the allows the mitigation of induced initial velocity. All regimes are visualized within the camera's optical range, also serving its purpose effectively.

Finally, the two conditions necessary for the study of secondary atomization are satisfied:

- the time required for the drop to enter breakup stages must be low enough for the phenomena to occur within the flow field
- the time required for the drop to surpass the boundary layer must be less than breakup initiation time

All drops, as seen before, suffer atomization within the uniform flow field and surpassing the boundary layer with practically no deformation seen in every case.

Chapter 5

Conclusions and Future Work

The last chapter of this dissertation is a conclusive summary and suggestion of future work, based on the results of the experimental study conducted. Firstly the conclusions are presented and lastly improvements suggested for the experimental facility and methodology.

5.1 Conclusions

In a first approach, the visualization of the regimes presented in the literature is successful for all the fluids involved in this work. Coupled with this, the first occurrence of each regime coincides with the Weber number values proposed by recent studies, for the fuel mixtures. Furthermore, the Dual-Bag regime is identified and does not appear within the Weber number range proposed in the literature. However, the water requires a higher cross-flow velocity to ensure the regimes are encountered. For the earlier bag and bag-plume regimes, a higher Weber number was necessary to verify their appearance. Although the flow speed was greater for the later ones, shear-plume and shear regimes, the resultant Weber number does not increase in the same fashion. This is due to the waters' surface tension and We expression indicating that a smaller droplet diameter will require a higher cross-flow speed to achieve the said regimes, but as velocity is raised to the second power, the resultant We is not greater in the same magnitude. In fact, the required value for the latest regimes to be encountered is lower than the fuel mixtures.

Weber number is determined using the relative velocity between flow and drop. The velocity components of the drops behave as expected, with the vertical velocity diminishing as flow speed increases and horizontal velocity also increasing. The half jet fuel mixture (Jet A-1 50% - 50% HVO) shows a different variation of these values with an increase, followed by a decrease and further increase of the values. Albeit, the main drop velocity, U_d, is roughly the same for all situations presenting a mean value of $U_d \approx 2\,\mathrm{m\,s^{-1}}$. This does not greatly influence the value of relative velocity, yet for accuracy purposes is still calculated and used for We determination. The Reynolds number, calculated using U_r and μ_g, shows a simple variation with the speed producing an operation range of $Re = 1886 - 6682$.

The Ohnesorge numbers produced by the drops with $D_0 \approx 3\,\mathrm{mm}$, are all $\mathrm{Oh} < 0.1$, that indicates a point of negligible viscosity. The correlations for these conditions appear to have a very small increase with the increase of this non-dimensional number. As stated, the first visualization of each regime is concordant with the literature, Figure 4.7, except for the water experiments as also explained.

The study of the maximum cross-stream diameter is approached in a We and Oh based manner. The variation of Weber number indicates a fairly according fit with the proposed criteria for $\mathrm{We} < 30$, and a deviation for further values. The first interval sees an increase of the cross stream diameter, yet late a steep decrease of this value is encountered, contradicting previous works. Analysing the results with the variation of Oh, one can notice a mean constant trend for each regime of $\varepsilon = 1.75$, rather than this value being a transition between Deformation and Bag regimes. It is also noticed, for the present dissertation, threshold lines cannot be identified for none of the regimes.

In a similar way, the breakup time is discussed. For the breakup initiation time, τ_{ini}, due to the Weber number variation, a decrease in the time needed for breakup to ensue seems to decrease with the increase of We, but not in the same way as proposed by other authors. Due to the variation of Ohnesorge number the values seem to fit well with the correlations, except for the shear regime, which presents lower values than those expected. The total breakup time, τ_{tot}, when plotted against We, shows an apparent linear increase with the increase of this non-dimensional parameter. While for the variation of Oh there is a scatter of results with no visual pattern to follow.

Moreover, the time-wise variation of the drops' cross-stream diameter since its insertion in the flow field shows that a joint fluid and regime based approach is preferable rather than their separation. This consideration allowed the observation of non-conformities with past proposed correlations, and since the density of data is rather extensive for this case, a correlation is proposed assuming the variation of the diameter through time is not constant and equal as it advances further downstream.

Drop trajectory until the first signs of secondary atomization is presented. The centroid determination using the adapted MatLab™algorithm allowed the verification that as one increases the flow speed, the vertical travel distance of the drop shortens. As for the horizontal travel distance, the regime and fluid influences this parameter. Nonetheless, the Bag-Plume regimes is the one that takes a longer flow direction distance to indicate the first signs of breakup, analogous to the breakup initiation time, even if the thresholds chosen for the measurements are not the same. Once again, the water mixtures show a much shorter travel distance in all regimes, and both vertical and horizontally. The greater cross-flow is the reason for this event.

Lastly, the condition for the study of breakup phenomena are guaranteed: the drop does not suffer atomization within the boundary layer and does not show signs of significant deformation in this area; drop suffers atomization within the flow field.

5.2 Future Work

The extension of experimental data is of much importance to for the verification of present results. Not only do these appear to fall off the proposed correlations, in some cases, it is also a new set of mixtures. Using the present data in computational models can be effective for the minimization of assumption errors and maximization of the results' quality.

Maintaining the Ohnesorge number for the different mixtures is also important. This is done by varying the drops initial diameter and can have a big effect on the Weber number thresholds. Studying a more vast range of Weber numbers is also a big improvement, and can further prove the present results. Identifying the range of the Dual-Bag regime is a big addition to the present work, and to the literature itself.

Lastly, yet no less important, the identification and parametrization of the resulting secondary atomization droplets is the main difficulty in the experimental work scene. It has been done for other fluids, yet with arguable results. The new set of mixtures can provide significant advances in the study of the Aerodynamic Breakup phenomena.

Bibliography

[1] ASTM D1655, *Standard Specification for Aviation Turbine Fuels*. American Society for Testing and Materials, 2015.

[2] ASTM D7566, *Standard Specification for Aviation Turbine Fuel Containing Synthesized Hydrocarbons*. American Society for Testing and Materials, 2016.

[3] B. Pizziol, "Design and experimental characterization of an air-assisted, impinging-jets atomizer for aeronautical applications with biofuel," Ph.D. dissertation, POLITECNICO DI MILANO, Scuola di Ingegneria Industriale e dell'Informazione, 2016.

[4] C. Bai and A. Gosman, "Development of methodology for spray impingement simulation," *SAE transactions*, pp. 550–568, 1995.

[5] D. R. Guildenbecher, C. López-Rivera, and P. E. Sojka, "Secondary atomization," *Exp Fluids*, vol. 46, no. 3, pp. 371–402, jan 2009.

[6] L. P. Hsiang and G. M. Faeth, "Near-limit drop deformation and secondary breakup," *International Journal of Multiphase Flow*, vol. 18, no. 5, pp. 635–652, 1992.

[7] W. H. Chou, L. P. Hsiang, and G. M. Faeth, "Temporal properties of drop breakup in the shear breakup regime," *International Journal of Multiphase Flow*, vol. 23, no. 4, pp. 651–669, 1997.

[8] L. P. Hsiang and G. M. Faeth, "Drop properties after secondary breakup," *International Journal of Multiphase Flow*, vol. 19, no. 5, pp. 721–735, 1993.

[9] Hsiang, L. P. and Faeth, G. M., "Drop deformation and breakup due to shock wave and steady disturbances," *International Journal of Multiphase Flow*, vol. 21, no. 4, pp. 545–560, 1995.

[10] C. Arcoumanis, D. S. Whitelaw, and J. H. Whitelaw, "Breakup of droplets of newtonian and non-newtonian fluids," *Atomization and Sprays*, vol. 6, no. 3, 1996.

[11] C. Rodrigues, J. Barata, and A. Silva, "Modeling of Droplet Deformation and Breakup," *Journal of Propulsion and Power*, vol. 32, no. 3, pp. 1–9, may 2016.

[12] B. E. Gel'fand, S. A. Gubin, S. M. Kogarko, and S. P. Komar, "Singularities of the breakup of viscous liquid droplets in shock waves," *Journal of Engineering Physics*, vol. 25, no. 3, pp. 1140–1142, 1975.

[13] M. Pilch and C. A. Erdman, "Use of breakup time data and velocity history data to predict the maximum size of stable fragments for acceleration-induced breakup of a liquid drop," *International Journal of Multiphase Flow*, vol. 13, no. 6, pp. 741–757, 1987.

[14] C. M. G. Rodrigues, "Modelling of Spray-Wall Impingement," Ph.D. dissertation, University of Beira Interior, 2016.

[15] Z. Dai and G. M. Faeth, "Temporal properties of secondary drop breakup in the multimode breakup regime," *International Journal of Multiphase Flow*, vol. 27, no. 2, pp. 217–236, 2001.

[16] H. Zhao, H.-f. Liu, W.-f. Li, J.-l. Xu, H. Zhao, H.-f. Liu, W.-f. Li, and J.-l. Xu, "Morphological

classification of low viscosity drop bag breakup in a continuous air jet," *Physics of Fluids*, vol. 114103, no. 2010, 2010.

[17] H. Zhao, H.-f. Liu, X.-k. Cao, W.-f. Li, and J.-l. Xu, "International Journal of Multiphase Flow Breakup characteristics of liquid drops in bag regime by a continuous and uniform air jet flow," *International Journal of Multiphase Flow*, vol. 37, no. 5, pp. 530–534, 2011. [Online]. Available: http://dx.doi.org/10.1016/j.ijmultiphaseflow.2010.12.006

[18] X.-k. Cao, Z.-g. Sun, W.-f. Li, H.-f. Liu, and Z.-h. Yu, "A new breakup regime of liquid drops identified in a continuous and uniform jet flow," *Physics of Fluids*, vol. 057103, no. 2007, 2007.

[19] H. Zhao, H.-F. Liu, J.-L. Xu, W.-F. Li, and K.-F. Lin, "Temporal properties of secondary drop breakup in the bag-stamen breakup regime," *Physics of Fluids*, vol. 25, no. 5, p. 054102, may 2013.

[20] F.-O. Bartz, D. R. Guildenbecher, R. Schmehl, R. Koch, H.-J. Bauer, and P. E. Sojka, "Model comparison for single droplet fragmentation under varying accelerations," *ILASS - 24th European Conference on Liquid Atomization and Spray Systems*, 2011.

[21] R. Schmehl, G. Maier, S. Wittig, and Lehrstuhl, "Cfd analysis of fuel atomization, secondary droplet breakup and spray dispersion in the premix duct of a lpp combustor," in *Eighth International Conference on Liquid Atomization and Spray Systems*, Pasadena, CA, USA, 2000.

[22] F.-O. Bartz, R. Schmehl, R. Koch, and H.-J. Bauer, "An extension of dynamic droplet deformation models to secondary atomization," *ILASS – 23rd Annual Conference on Liquid Atomization and Spray Systems*□, 2010.

[23] T. Kékesi, G. Amberg, and L. P. Wittberg, "Drop deformation and breakup," *International Journal of Multiphase Flow*, vol. 66, pp. 1–10, nov 2014.

[24] S. A. Krzeczkowski, "Measurement of liquid droplet disintegration mechanisms," *International Journal of Multiphase Flow*, vol. 6, no. 3, pp. 227–239, 1980.

[25] T. G. Theofanous, G. Li, and T.-N. Dinh, "Aerobreakup in rarefied supersonic gas flows," *Journal of fluids engineering*, vol. 126, no. 4, p. 516, 2004.

[26] A. A. Ranger and J. A. Nichols, "Aerodynamics shattering of liquid drops," *AIAA Aerospace Sciences Meeting*, no. 68, 1968.

[27] G. M. Faeth, L. P. Hsiang, and P. K. Wu, "Structure and breakup properties of sprays," *International Journal of Multiphase Flow*, vol. 21, pp. 99–127, 1995.

[28] B. E. Gel'fand, "Droplet breakup phenomena in flows with velocity lag," *Prog. Energy Combust. Sci.*, vol. 22, no. 3, pp. 201–265, 1996.

[29] P. J. O'Rourke and A. A. Amsden, "The tab method for numerical calculation of spray droplet breakup," *SAE Technical Paper*, 1987.

[30] G. I. Taylor, *The shape and acceleration of a drop in a high speed air stream.* Cambridge University Press, 1963, vol. 3, no. 457–464.

[31] S. Hwang, Z. Liu, and R. D. Reitz, "Breakup mechanisms and drag coefficients of high-speed vaporizing liquid drops," *Atomization and Sprays*, vol. 6, no. 3, 1996.

[32] S. H. Park, H. J. Kim, H. K. Suh, and C. S. Lee, "Experimental and numerical analysis of spray-atomization characteristics of biodiesel fuel in various fuel and ambient temperatures conditions," *International Journal of Heat and Fluid Flow*, vol. 30, no. 5, pp. 960–970, oct 2009.

[33] E. A. Ibrahim, H. Q. Yang, and A. J. Przekwas, "Modeling of Spray Droplets Deformation and Breakup," *AIAA*, vol. 9, no. 4, pp. 651-654, 1993.

[34] J.-H. Park, Y. Yoon, and S.-S. Hwang, "Improved tab model for prediction of spray droplet deformation and breakup," *Atomization and sprays*, vol. 12, no. 4, 2002.

[35] F. X. Tanner, "Liquid jet atomization and droplet breakup modeling of non-evaporating diesel fuel sprays," *SAE transactions*, pp. 127–140, 1997.

[36] S. Kim, J. W. Hwang, and C. S. Lee, "Experiments and modeling on droplet motion and atomization of diesel and bio-diesel fuels in a cross-flowed air stream," *International Journal of Heat and Fluid Flow*, vol. 31, no. 4, pp. 667–679, 2010. [Online]. Available: http://dx.doi.org/10.1016/j.ijheatfluidflow.2010.02.001

[37] S. Tavangar, S. H. Hashemabadi, and A. Saberimoghadam, "CFD simulation for secondary breakup of coal – water slurry drops using OpenFOAM," *Fuel Processing Technology*, vol. 132, pp. 153–163, 2015. [Online]. Available: http://dx.doi.org/10.1016/j.fuproc.2014.12.037

[38] T. Kékesi, "Scenarios of drop deformation and breakup in sprays," Ph.D. dissertation, Royal Institute of Technology, Department of Mechanics, 2017.

[39] G. Strotos, I. Malgarinos, N. Nikolopoulos, M. Gavaises, K.-s. Nikas, and K. Moustris, "Determination of the aerodynamic droplet breakup boundaries based on a total force approach," *International Journal of Heat and Fluid Flow*, vol. 69, no. November 2017, pp. 164–173, 2018. [Online]. Available: https://doi.org/10.1016/j.ijheatfluidflow.2018.01.001

[40] N. Cunha, "Experimental study and of a single and droplet impinging and on dry and surface with and without a crossflow and jet," Master's thesis, University of Beira Interior, 2018.

[41] V. Brederode, *Fundamentos de aerodinâmica incompressível*. Edição do autor, 1997.

[42] R. Mehta and P. Bradshaw, "Design rules for small low speed wind tunnels," *The Aeronautical Journal (1968)*, vol. 83, no. 827, p. 443–453, 1979.

[43] T. Morel, "Comprehensive design of axisymmetric wind tunnel contractions," *Journal of Fluids Engineering*, 1975.

[44] B. S. Stratford, "The prediction of separation of the turbulent boundary layer," *National Gas Turbine Establishment, Farnborough*, no. Goldstein 1938, pp. 1–16, 1958.

[45] D. F. da Conceição Vieira, "Twin Impinging Jets Inline with a Low-Velocity Crossflow," Ph.D. dissertation, University of Beira Interior, 2017.

[46] "Drifton the science of dispersing," https://www.drifton.eu/shop/46-stainless-steel-dispensing-tips/, accessed: 2018-03-15.

[47] D. F. S. Ribeiro, "Experimental Study of a Single Droplet Impinging upon Liquid Films : Jet Fuel and Biofuel Mixtures," Master's thesis, University of Beira Interior, 2018.

[48] C. Tropea and A. L. Yarin, *Springer handbook of experimental fluid mechanics*, Springer, Ed. Springer Science and Business Media, 2007.

[49] B. Pizziol, M. Costa, M. O. Panão, and A. Silva, "Multiple impinging jet air-assisted atomization," *Experimental Thermal and Fluid Science*, vol. 96, no. March, pp. 303–310, 2018. [Online]. Available: https://doi.org/10.1016/j.expthermflusci.2018.03.019

[50] I. Ferrão, "Dynamic behaviour of a single droplet impinging onto a sloped surface," Master's thesis, University of Beira Interior, 2018.

[51] C. R. Council, *Handbook of aviation fuel properties*. The Council, 1983.

Appendix A

Publications

Carrolo, G, Silva, A. and Barata, J., Design of an Experimental Facility to Study the Aerodynamic Breakup of a Single Droplet, in: IV LAETA Young Researchers Meeting, 9-10 November 2017, Covilhã, Portugal.

Carrolo, G., Ribeiro, D., Silva, A., Barata, J., Aerodynamic Breakup of a Single Droplet due to a Crossflowed Airstream, in: AIAA Science and Technology Forum and Exposition 2019, 7-11 January 2019, San Diego, California, USA. (Extended Abstract)

Carrolo, G., Ribeiro, D., Silva, A., Barata, J., Aerodynamic Breakup of a Single Droplet due to a Crossflowed Airstream, in: AIAA Science and Technology Forum and Exposition 2019, 7-11 January 2019, San Diego, California, USA.

DESIGN OF AN EXPERIMENTAL FACILITY TO STUDY THE AERODYNAMICS BREAKUP OF A SINGLE DROPLET

Gabriel Carrolo[a*]**, Jorge Barata**[a]**, André Silva**[a]**,**
a) AeroG - LAETA, Calçada Fonte do Lameiro, 6201-001 Covilhã
* e-mail: Gabriel.c.carrolo@gmail.com

Keywords: Experimental, Aerodynamics Breakup, Droplet, Jet-Fuel.

Abstract.

The development of a spray since the early stages of liquid injection is driven by a set of parameters such as the pressure of injection, the characteristics of the injector nozzle and the properties of the surrounding environment where the droplets are inserted. The latter aspect -- in which the presence of a cross-flowing gas may be considered -- greatly influences the course of the spray evolution without the need to directly interfere with the injection system. In fact, the pressure distribution around the drop due to the relative velocity between gas and particle is responsible for the emergence of instabilities that may lead to deformation and disintegration into smaller fragments. This process is referred to as secondary atomization.

Several authors reported the existence of two stages of atomization: the primary breakup and secondary breakup. In practical applications, as e.g. direct injection engines and gas turbines, the combustion efficiency is dictated by the vaporization rate which, in turn, is influenced by the fuel spray atomization. Therefore, the comprehensive understanding of the breakup mechanisms and the characteristics of the resulting elements is essential to make it possible to develop highly efficient systems that rely on the atomization process.

The main objective in the study of the deformation and breakup mechanisms is to determine the final droplet size in order to introduce these data in spray impingement models. This goal has been proved very difficult to achieve due to the number of parameters that has a direct effect on the spray behavior. Furthermore, besides the influence of the aerodynamic forces in the deformation response, the way those forces are applied to particles also affects secondary atomization. In the present work, an experimental facility is design and built to study the deformation and breakup of a jet-fuel single droplet injected into a cross-flowed air stream in order improved our in-house developed breakup model.

Aerodynamic Breakup of a Single Droplet due to a Crossflowed Airstream

Gabriel Carrolo[1], Daniela Ribeiro[2], Jorge Barata[3], and André Silva[4]
Universidade da Beira Interior, Covilhã, 6200-001, Portugal

Extended Abstract

Since the creation of jet engine systems, pollution and combustion efficiency are closely related due to fuel atomization. The study of drop deformation and breakup came from the necessity of producing smaller droplets of fuel thus enhancing the combustion efficiency. This promotes less percentage of non-combusted fuel and a reduction of environmentally harmful molecule emissions. Several studies throughout the years have produced experimental and numerical models of the Breakup regimes for water, glycerol mixtures, diesel and bio-diesel [1]. The current work centers its results in fuel mixtures of Jet A1 and HVO (Hydro processed Vegetable Oil) bio-fuel, to search for differences in the thresholds of the various breakup regimes.

The main objective is to visualize the several breakup regimes and to establish thresholds for each breakup regime. An experimental installation was design and built to study the main parameters that influence the deformation, bag, multimode and shear breakup regimes. The use of a crossflowed air stream, high speed camera for image acquisition and a syringe pump for droplet diffusion are the main items of the experimental facility. Drop initial diameter and height above the wind tunnel are varied in order to achieve different Weber and Ohnesorge numbers, and three different mixtures are used: 100% Jet A1, 50% Jet A1/50% HVO and water, being the latter one used as a reference because of its specific and well-known properties. The reason behind the mixture choices is that the current legislation only permits the use of at least 50% of Jet A1 fuel for commercial aviation purposes even though it is rare for companies to use high percentages of HVO in the aircrafts.

With the use of a wind tunnel installation as the crossflow velocity is increased, the relative velocity of the drop is influenced and will indicate a change of regime of the secondary atomization. The creation of correlations between the airstream and the corresponding breakup mechanism is not widely demonstrated as often as the use of the drops Weber number. So, for the preliminary stages of this work the velocity of the crossflow was the main parameter that would be varied. Hsiang and Faeth [2] proposed the limits of weber number for each regime as shown in Table 1:

Table 1. Breakup regimes - Transition We for Newtonian drops with Oh < 0.1.

Deformation/Vibrational	*0 < We < 11*
Bag	*11 < We < 35*
Multimode	*35 < We < 80*
Sheet-Thinning	*80 < We < 350*
Catastrophic	*We >350*

With the Weber and Ohnesorge numbers being as follows [3]:

$$We = \frac{\rho D_0 {U_0}^2}{\sigma} \quad (1)$$

$$Oh = \frac{\mu}{\sqrt{\rho\sigma D_0}} \quad (2)$$

---

[1] Masters' Student, Aerospace Sciences Department, gabriel.c.carrolo@gmail.com.
[2] PhD Student, Aerospace Sciences Department, dani_ribeiro8@hotmail.com
[3] Full Professor, Aerospace Sciences Department, and Associate Fellow of AIAA, jbarata@ubi.pt.
[4] Assistant Professor, Aerospace Sciences Department, and Member of AIAA, andre@ubi.pt.

where ρ is the density of the droplet fluid, D_0 is the droplet diameter, V_0 is the droplet velocity, σ is the surface tension of the droplet fluid and with μ being the dynamic viscosity of the droplet fluid. Since the biggest drop diameter used is *4.02 mm* it is assured that $Oh < 0.1$, and so we the current test conditions can in fact be used to verify the transition criteria.

Although the fluids of study used in the construction of Table 1 are not Jet A1, it is a good compromise for the use of a reference for comparison. It was found that Jet A1 fuel presents the same regimes than the other fluids, but they may not occur for the same Weber numbers as water and glycerin mixtures, which may indicate some behavior fluctuations in the transition of each regime. The use of a new mixture means that the main parameters that influence the Aerodynamic Breakup are now being changed, and this change must be documented to identify the variations on the visualization and fragmentation of the parent droplet. Table 2 shows the properties of each fluid that was used in the present work (for details see [4]).

Table 2. Properties of each fluid of study.

	$\rho\ [kg.m^{-3}]$	$\sigma\ [mN/m]$	μ [Pa.s]
Water	*1000*	*71.97*	*0.001003*
50% Jet A1 – 50% HVO	*792.338*	*24.64*	*0.00179*
100% Jet A1	*798.285*	*25.37*	*0.00112*

For each regime there are 4 stages that characterize the breakup phenomena, where the first one is the same for all, being the deformation of the droplet into a disk-like shape, more specifically an oblate ellipsoid. The Bag Breakup regime presents the formation of a bag structure with a thick ring followed by the fragmentation of the bag and posterior fragmentation of the ring structure [5]. Multimode Breakup regimes differ only from the bag regimes because of the presence of a plume structure in the middle of the bag that produces larger droplets than the bag structure [2]. Shear Breakup regime occurs at higher velocities and Weber numbers and the shear forces from the surrounding flow makes the surface of the drop unstable at the edges creating sheet-like structures that then breakup into smaller droplets due to stripping of mass [6, 7].

For each of the beforementioned regimes extensive visualization and image acquisition was done for each mixture. Weber number and drop velocities were calculated and the velocities of the crossflowed airstream were mapped, Table 3 is the example of the Jet A1 data.

Table 3. Crossflow velocity thresholds for breakup regimes with Jet A1.

z [cm]	***25***
Deformation	$0 < U_c < 6.0$ *m/s*
Bag Breakup	$6.0 \leq U_c < 8.5$ *m/s*
Bag-Plume Breakup	$8.5 \leq U_c < 12.9$ *m/s*
Shear-Plume Breakup	$12.9 \leq U_c < 17.8$ *m/s*
Shear	$17.8 \leq U_c < 31$ *m/s*

Where U_c is the velocity of the crossflow and z the height from the wind tunnels upper boundary and the point at which the droplet is formed and dropped. For the case of z=*25cm* and a droplet diameter of *3.04mm*, Fig 1 to Fig 5 are a visualization of the drops trajectory and subsequent deformation phases for a droplet at several crossflow velocities. The time at which the phases occur also are represented as a timeline. It is important to refer that the drop has no initial velocity and only gravity is used to accelerate its velocity.

The variation of height means a variation of the normal velocity of the droplet at $t=0$ *ms*, which corresponds to the instant just before the drop suffers the influence of the crossflow, in Fig 1 to Fig 5. At the moment of the interaction between the flow and drop, this height variation can indicate a difference in the drops deformation, trajectory, regime and overall behavior. The drops normal velocity will be varied using at least two different conditions ($z=50$ *cm* and $z=75$ *cm*) and the regimes and variations will be visualized in order to study the beforementioned parameters.

The next step is to find the characteristic time of the onset of breakup phenomena [8, 9]. Computational models proposed seem to lack a well-defined time step for each regime and this work will be able to aid in several key features missing in the Breakup Model proposed by Rodrigues et al [10]. Finally, the mean diameter of child droplets is studied to since the surface tension of Jet A1 is much smaller than the existing fluids used in passed works [11].

Overall, the present works centers its attention in the use of a different fluid and what's the influence if the property changes in the general breakup panorama.

Acknowledgments

The present work was performed under the scope of Laboratório Associado em Energia, Transportes e Aeronáutica (LAETA) – activities and it was supported by Fundação para a Ciência e Tecnologia (FCT) through the project UID/EMS/50022/2013.

References

[1] S. Kim, J. W. Hwang and C. S. Lee, "Experiments and modeling on droplet motion and atomization of diesel and bio-diesel fuels in a cross-flowed airstream," *Journal of Heat and Fluif Flow,* vol. 31, 2010.

[2] L. P. Hsiang and G. M. Faeth, "Drop Properties After Secondary Breakup," *Journal of Multiphase Flow,* vol. 19, no. 5, pp. 721-735, 1993.

[3] C. X. Bai and D. Gosman, "Development of a methodology for spray impingement simulation," *SAE Paper 950283,* 1995.

[4] D. Ribeiro, "*Experimental Study of a Single Droplet Impinging upon Liquid Films: Jet Fuel and Biofuel Mixtures,* " Master Dissertation, University of Beira Interior (2018).

[5] W. H. Chou and G. M. Faeth, "Temporal properties of secondary drop breakup in the bag breakup regime," *Journal of Multiphase Flow,* vol. 24, pp. 889-912, 1998.

[6] J. A. Nicholls and A. A. Ranger, "Aerodynamic shattering of liquid drops," *AIAA,* 1969.

[7] D. R. Guildenbecher, C. Lopéz-Rivera and P. E. Sojka, "Secondary atomization," 22 January 2009.

[8] H. Zhao, H.-F. Liu, J.-L. Ju and W.-F. Li, "Temporal properties of secondary drop breakup in the bag-stamen regime," 3 May 2013.

[9] T. Kékesi, G. Amberg and L. P. Wittberg, "Drop deformation and breakup," *Journal of Multiphase Flow,* vol. 66, 2014.

[10] C. Rodrigues, J. Barata and A. Silva, "Modeling of Droplet Deformation and Breakup," *Journal of Propulsion and Power,* 2016.

[11] M. Jain, R. S. Prakash and G. Tomar, "Secondary breakup of a drop at moderate Weber numbers," 19 March 2015.

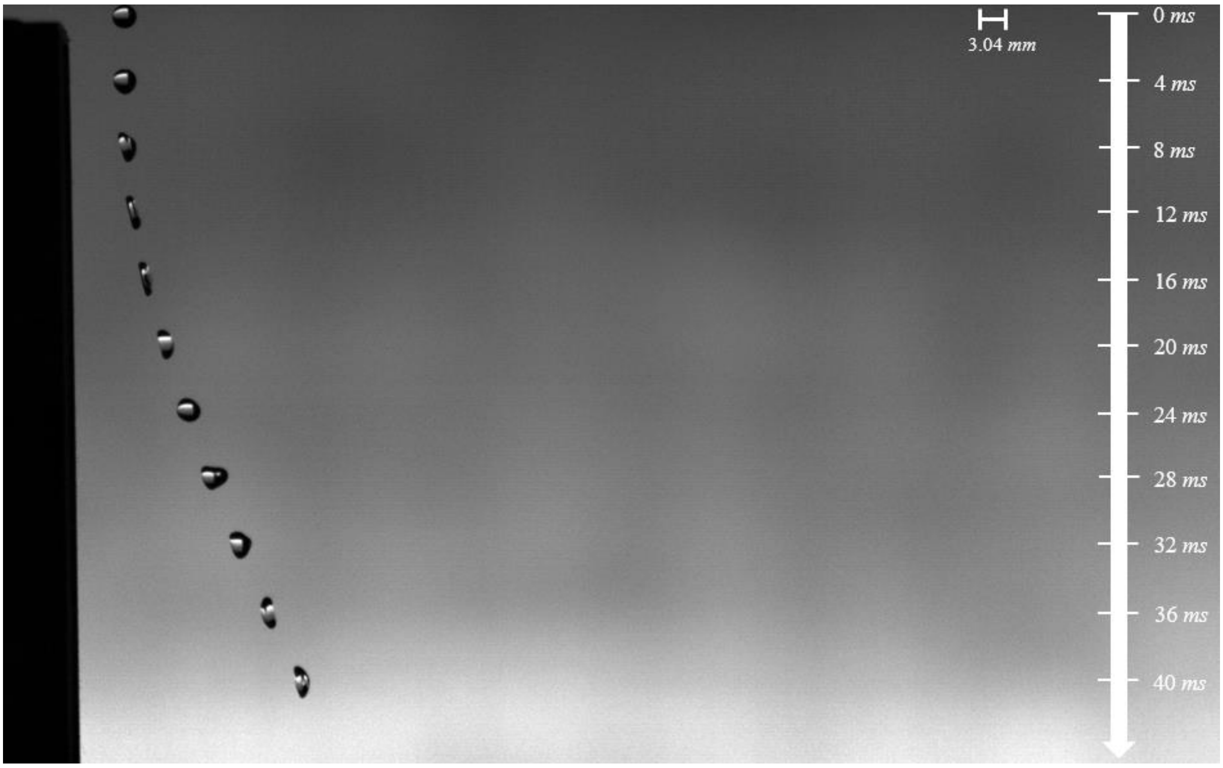

Fig 1. Visualization sequence of the deformation regime of Jet A1 fuel droplet (*D_0 = 3.04mm*; *U_c= 4 m/s*).

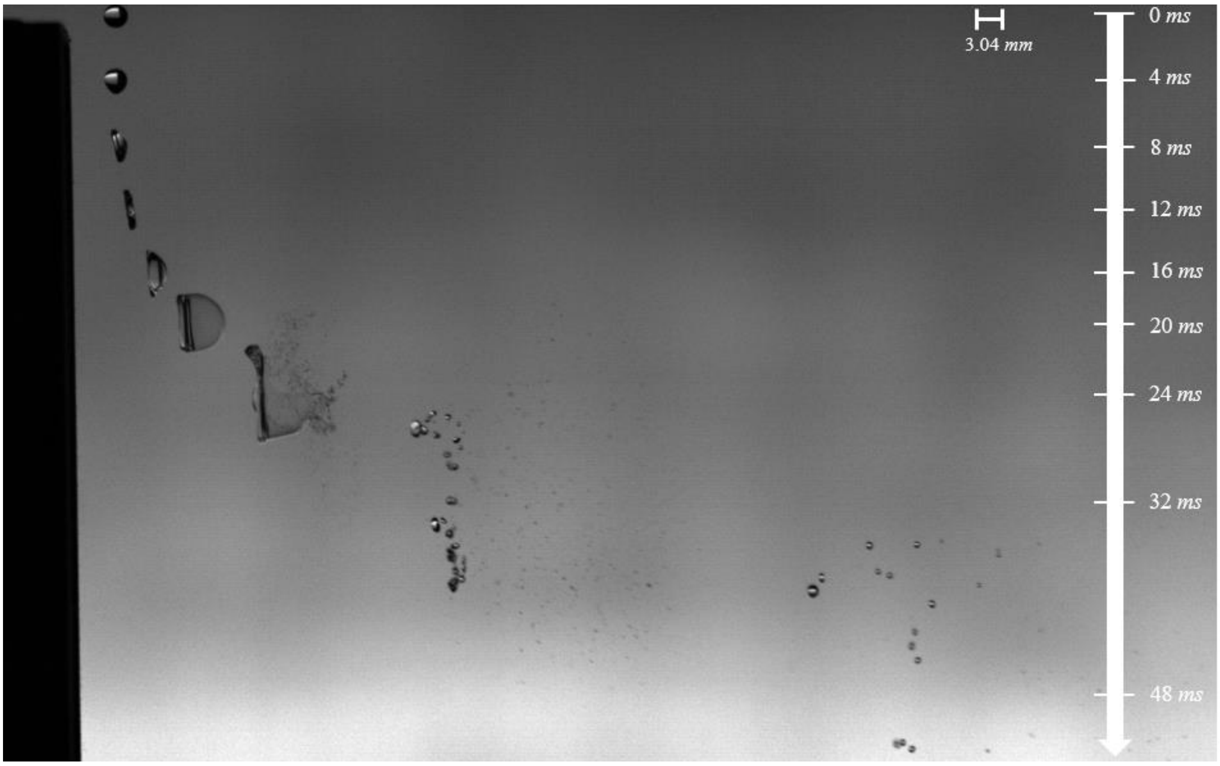

Fig 2. Visualization sequence of the Bag Breakup regime, with the respective time stamp and drop diameter ($D_0 = 3.04mm$; $U_c = 6\ m/s$).

Fig 3. Visualization sequence of the Bag-Plume (Multimode) regime, with the respective time stamp and drop diameter (*D_0 = 3.04mm*; *U_c= 8.5 m/s*).

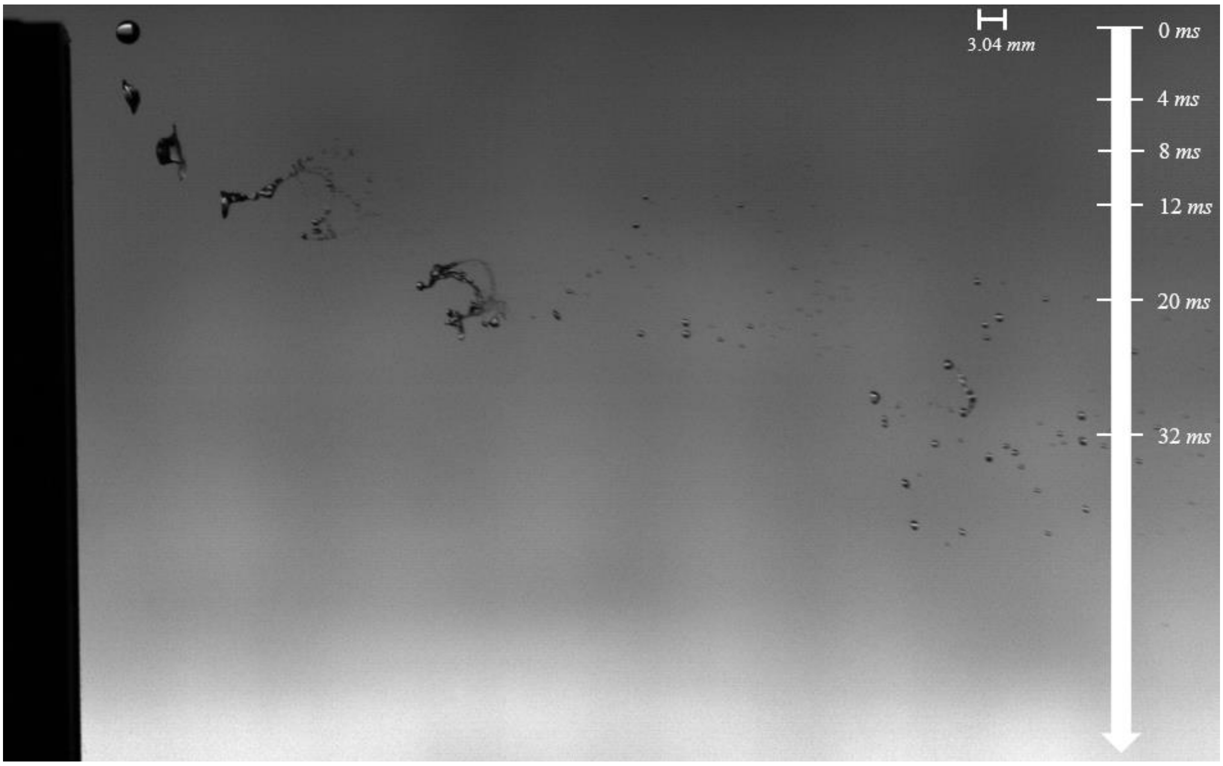

Fig 4. Visualization sequence of the Shear-Plume (Multimode) regime, with the respective time stamp and drop diameter (D_0 = *3.04mm*; U_c= *12.8 m/s*).

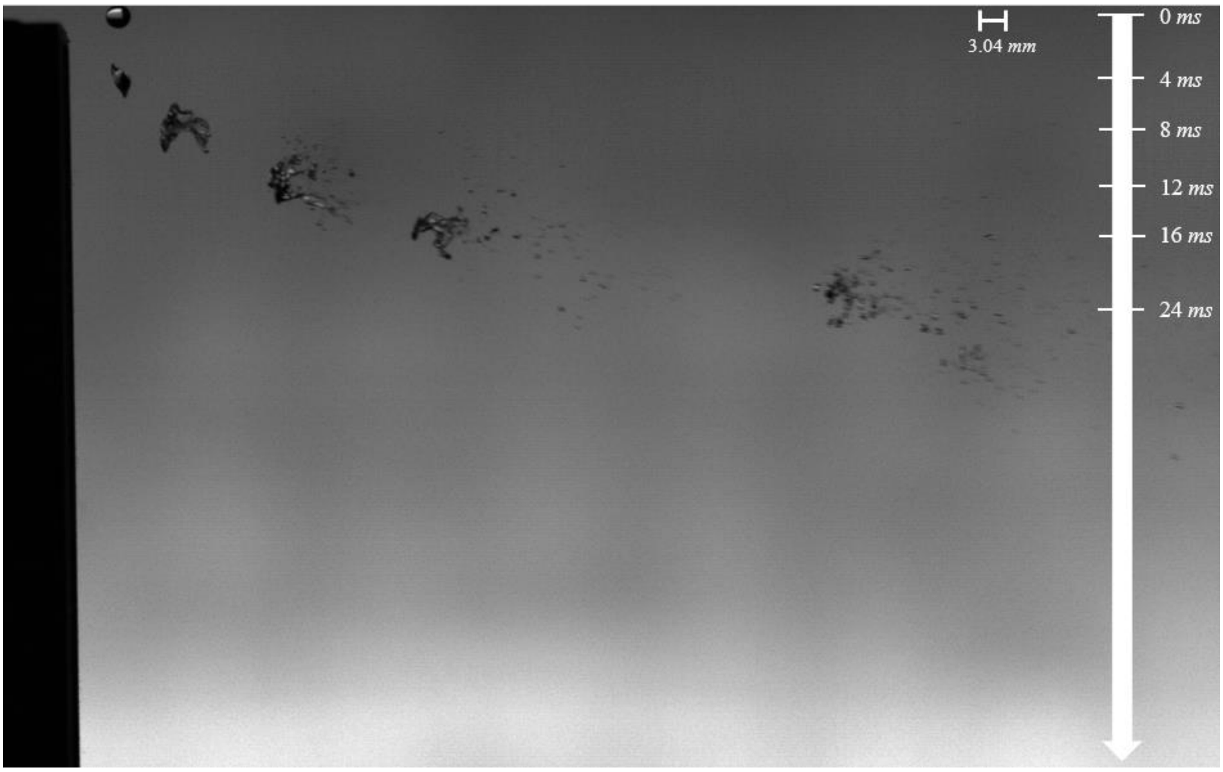

Fig 5. Visualization sequence of the Shear Breakup regime, with the respective time stamp and drop diameter (*D_0 = 3.04mm*; *U_c= 17.8 m/s*).

AIAA SciTech Forum
7-11 January 2019, San Diego, California
AIAA Scitech 2019 Forum

10.2514/6.2019-0628

Aerodynamic Breakup of a Single Droplet due to a Crossflowed Airstream

Gabriel A. C. Carrolo[*], Daniela F. S. Ribeiro[†], Jorge M. M. Barata[‡], André R. R. Silva[§]
University of Beira Interior, Covilhã, 6200-001, Portugal.

The main breakup regimes are visualized and studied with the help of a high-speed camera and a continuous jet of air, provided by a wind tunnel, is used to transition the droplet into the various stages of secondary atomization. The use of Jet Fuel and Biofuel mixtures is the focal point of this study. All the known regimes are encountered and each transitional We is calculated. The variation of We due to Oh is described, in addition to the comparison between We number thresholds and correlations existent in the literature for each regime transition. The influence of these numbers on the dimensionless characterization of time and later the maximum cross stream diameter is shown. Finally, a correlation for the temporal evolution of the drops' cross stream diameter for all regimes, assuming its deformation is not a linear function of time, is proposed.

I. Nomenclature

D_0 = initial droplet diameter
D_{max} = maximum cross stream diameter of the deformed droplet
Oh = Ohnesorge number
t = time
$t*$ = characteristic breakup time
U_0 = relative velocity between droplet and gas in the main flow direction
U_c = crossflow velocity
We = Weber number
$\mathrm{We_c}$ = critical Weber number
$\mathrm{We_t}$ = transitional Weber number for each breakup regime
Z_t = wind tunnel nozzle height
ϵ = ratio between density of liquid and gas (ρ_l/ρ_g)
μ = dynamic viscosity
ρ = density
σ = surface tension
τ = non dimensional characterization of time
τ_{ini} = non dimensional characterization of time for the initiation of breakup
τ_{tot} = non dimensional characterization of time for total breakup

II. Introduction

The study of the deformation and breakup of a droplet due to a crossflowed air stream has a wide range of engineering and industrial applications. Combustion efficiency is also known to depend on the atomization of fuel droplets. Therefore, the study of breakup mechanisms and the parameters governing them is of paramount importance for a more efficient combustion system promoting the emission of fewer exhaust gases. Albeit, the environment surrounding these mechanisms plays an important role in spray development, and the presence of a cross flowing gas mitigates the need to alter the injection system. As stated in Ref. [1], the pressure distribution around the drop, due to the interaction

---

[*] Master's Student, Aerospace Sciences Department, gabriel.c.carrolo@gmail.com
[†] PhD Student, Aerospace Sciences Department, dani _ribeiro8@gmail.com
[‡] Full Professor, Aerospace Sciences Department, and Associate Fellow of AIAA, jbarata@ubi.pt
[§] Assistant Professor, Aerospace Sciences Department, and Member of AIAA, andre@ubi.pt

between both phases, is responsible for the appearance of instabilities that may lead to disintegration. Hinze [2] firstly introduced the conditions for the breakup regimes and stated the importance of the drops' dynamic pressure, viscous and surface tension forces. Ever since, numerous authors studied these phenomena, both experimentally and numerically, identifying the underlying parameters interfering with the droplets dynamic behavior.

The objective of this work is to experimentally identify and study the droplets behavior for each breakup regime, to establish the thresholds of the governing parameters, as well as analyzing the temporal evolutions of drop deformation as a function of We and Oh. The use of a wind tunnel, a high-speed camera for image acquisition and a syringe pump for droplet diffusion are the main components that made this experiment possible. Although a fair amount of research is available for water, glycerine, diesel, and biofuel mixtures [3], this work focuses on Jet Fuel and Hydro-processed Vegetable Oil (HVO) mixtures. To the best of the authors' knowledge such work has not been conducted before for these mixtures, while water is studied as a reference fluid because of its well known and defined properties.

Current legislation only permits the use of at least 50% Jet A-1 fuel for commercial aviation purposes, even though it is rare for companies to use high percentages of HVO in aero engines. Thus, the fuel mixtures employed in the current work are 100% Jet A-1, 75% Jet A-1 - 25% HVO and 50% Jet A-1 - 50% HVO.

The use of a continuous air stream and the ability to vary its velocity enables the visualization of different regimes reported in previous studies of breakup phenomena for different mixtures than those considered here. For a Newtonian fluid, the breakup regimes are mostly influenced by Weber [Eq.(1)] and Ohnesorge [Eq. (2)] numbers. The first is a characterization of the ratio between disruptive forces to stabilizing surface tension forces, while the second is associated with the viscosity effect and representing the ratio of viscosity forces to surface tension forces [4]:

$$We = \frac{\rho_g D_0 U_0^2}{\sigma} \tag{1}$$

$$Oh = \frac{\mu}{(\rho_g D_0 \sigma)^{0.5}} \tag{2}$$

where ρ_g is the density of the gaseous phase, D_0 is the droplets' diameter, U_0 is the relative velocity between gas and droplet, σ is the drops' surface tension and μ is the dynamic viscosity. These will help to classify the breakup regimes into Bag, Multimode, and Shear breakup. Each of these is described by four stages where the first one is the same for all regimes and it is characterized by the deformation of the droplet into a disk-like structure. The Bag Breakup, as the name indicates, produces a bag-shaped structure with a relatively thick ring, followed by the fragmentation of the bag and posteriorly of the ring [5]. The Shear Regime occurs at higher gas velocities and the shear forces from the flow at the drops' edges make its surface unstable, creating a stripping of mass resembling sheet-like structures that subsequently disintegrate into smaller droplets [6, 7]. The Multimode regime is seen as a transition between bag and shear stages, where we can identify three other different sub-regimes: Bag-Plume, Shear-Plume, and Dual-Bag. Bag-plume differs from the Bag regime only by the presence of a plume of fluid within the bag formation, shear-plume and shear regimes being analogous to this description [8]. In Ref. [9] it is later observed the existence of a new Dual-Bag regime where the bag and plume are formed, the bag then disintegrates, and the plume undergoes a new bag breakup regime and further fragmentation. Table 1 illustrates the Weber number thresholds, found by several authors, that are used as a reference for this work.

While dealing with a continuous load of aerodynamic forces applied to the droplet, instead of a sudden shock wave, it is important to study the characteristic time of each phase of the regimes, understanding the different variations and search useful correlations for numerical models. Small droplets are considered, typically, Oh < 0.1, meaning the viscous forces are less of an influence, as a higher Oh means a smaller tendency towards fragmentation.

Table 1 Transition We numbers from previous publications, adapted from Ref. [10].

<table>
<tr><td>Cao et al.
Ref. [9]</td><td colspan="5"></td><td colspan="4">Dual-bag breakup</td><td colspan="5"></td></tr>
<tr><td>Dai and Faeth
Ref. [11]</td><td colspan="2"></td><td colspan="2">Bag breakup</td><td colspan="4">Bag/plume breakup</td><td colspan="4">Plume/shear breakup</td><td colspan="2"></td></tr>
<tr><td>Faeth, Hsiang et al.
Refs. [12]-[13]</td><td colspan="2"></td><td colspan="5">Bag breakup</td><td colspan="5">Multimode breakup</td><td colspan="2">Shear breakup</td></tr>
<tr><td>Pilch and Erdman
Ref. [14]</td><td></td><td colspan="9">Bag Breakup</td><td colspan="3">Bag and stamen breakup</td><td>Sheet stripping breakup</td></tr>
<tr><td>Krzeczkowski
Ref. [15]</td><td colspan="4">Bag mechanism</td><td colspan="2">Bag-Jet mechanism</td><td colspan="5">Transition mechanism</td><td colspan="3">Shear/ stripping off mechanism</td></tr>
<tr><td rowspan="2"></td><td>10</td><td>12</td><td>13</td><td>15</td><td>18</td><td>28</td><td>30</td><td>35</td><td>40</td><td>41</td><td>50</td><td>63</td><td>80</td><td>100</td></tr>
<tr><td colspan="14">Weber number</td></tr>
</table>

Table 2 Properties of the fluids used in the experimental work, as presented by Ref. [16].

Substance	ρ [kg/m^3]	$\mu \times 10^3$ [Pa.s]	$\sigma \times 10^3$ [mN/m]	D [mm]	Oh $\times 10^3$
Jet A-1 100%	798.3	1.20	25.4	3.1	4.5
Jet A-1 75% - HVO 25%	795	1.44	25.5	3.1	5.7
Jet A-1 50% - HVO 50%	792.4	1.79	24.6	3.1	7.3
H_2O	998	1.00	72.0	3	2.2

III. Experimental Setup

The experimental setup focuses on the continuous jet conditions with a single droplet inserted in the flow with an initial velocity of $U_{d_y} = 0$[m/s], thus the only force influencing the drops' movement before the two-phase interaction is that of gravity, Fig. 1. A rectangular 2D wind tunnel combined with a driver fan that forces air through a system of tubes helps to produce the desired continuous jet. The droplet diffuser, a syringe pump connected through a tube to a needle capable of dispersing a single drop at a desired rate, is mounted 25[cm] above the wind tunnel's nozzle upper boundary and approximately 1[cm] from its exit. All the drops were dispersed with the same diameter of approximately 3[mm]. The fluids of test are as mentioned before: 100% Jet A-1, 75% Jet A-1 - 25% HVO, 50% Jet A-1 - 50% HVO and Water. The fluids properties are presented in Table 2.

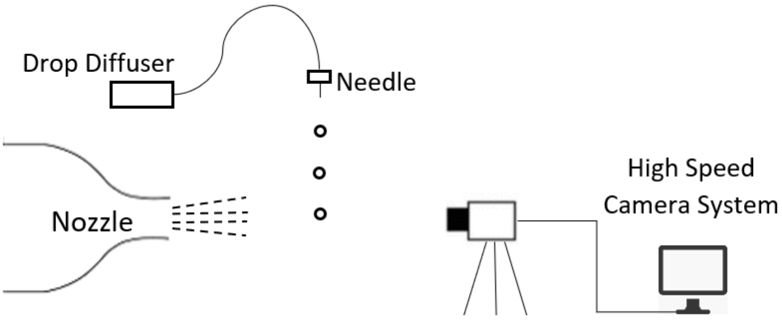

Fig. 1 Schematics of the experimental facility.

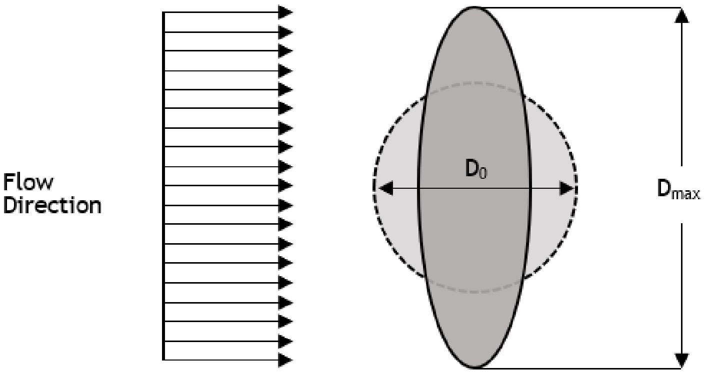

Fig. 2 Figurative representation of the droplets' deformation due to the air flow.

The need to maintain the gas flow essentially uniform is important so the droplet experiences a constant and smooth loading throughout all the phenomena. Various velocity profiles on the nozzle exit were measured and uniformity was verified, Fig. 3. Weber number ranges from $12 - 80$ and Oh < 0.1, meaning the present work is within the range of comparison to other author's results [11]. A high-speed camera (Photron FASTCAM mini UX50) was used for the image acquisition. With a resolution of 1.3[megapixel], a Macro Lens Tokina AT-X M100 AF PRO D and the help of a lighting rig behind a diffusion glass, the images were captured using a back-light technique. The images are captured at 2500[fps] with a shutter of 1/10000[s]. This resolution proved to be enough to visualize and furthermore measure the droplets in all the stages of the atomization process.

Image treatment is made with the aid of a Matlab R2018b software that processes images into binary code and enables the determination of the pixel size (113.75[μm]) and, consequently, the drops diameters. Moreover, the droplet's velocity components are also calculated in order to be able to use the relative velocity between the two phases for We calculation.

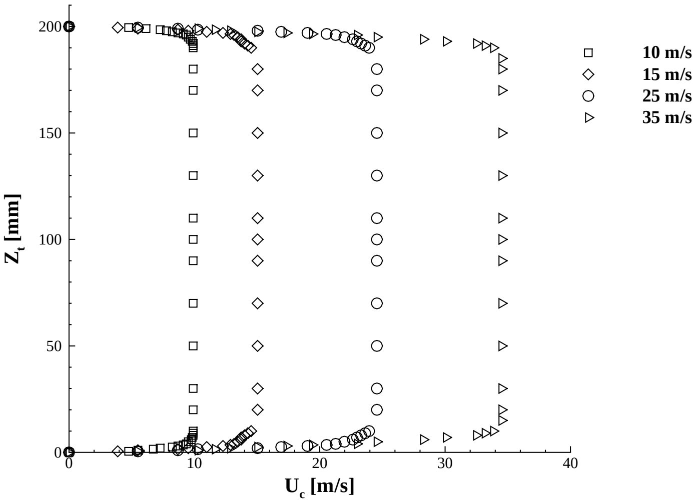

Fig. 3 Velocity profiles at the wind tunnels' nozzle exit.

The maximum cross-stream droplet diameter, D_{max}, is measured and plotted against the non-dimensional characterization of time, τ. Since the timestamps present in these kinds of work are very small, the normalization of time is of significance, not only for a better and easier understanding of the droplets time-wise evolution but also to enable the comparison between each breakup stage of all the regimes.

$$\tau = \frac{t}{t*} = \frac{tU_0}{D_0\epsilon^{0.5}} \tag{3}$$

IV. Results and Discussion

This section presents the analysis and discussion of the results obtained with special attention to the influence of the non-dimensional numbers in the drops' behavior. Firstly, the identification and visualization of each regime for the present mixtures is displayed. Afterward, the variation of Oh and its consequences regarding the different transitional We is explained. In addition, the influence of the aforementioned numbers on the time-wise evolution of initiation and total breakup times, as well as the cross stream maximum diameter, is also studied and characterized. Lastly, the evolution of the cross stream diameter is plotted against time. Dual-Bag Breakup Regime is identified, yet since only a few of the tests performed enabled the visualization of this phenomenon (for $40 < \mathrm{We} < 80$), the study of this regime is not taken into account for the present work.

A. Visualization of Breakup Stages

Figures 4-7 are a representation of the breakup phenomenon for the fluids. For all cases, there is the formation of a disk-like structure before its deformation into the various different structures that compose the regimes. There is no clear evidence of the formation of new structures and, since the droplets created by secondary atomization were not studied, in terms of size or volume, it is assumed that all the regimes are possible to be encountered and easily compared with those of previous works. The quantitative analysis of the acquired images is presented in the next sections, being this a qualitative representation of the phenomena encountered.

The literature also presents a recently identified breakup morphology called Dual-Bag. It is composed by four stages (after deformation): first bag formation, first bag breakup, core drop formation and subsequent breakup, and is said to appear at $28 < \mathrm{We} < 41$ [9]. However, in the present study, it was only identified from $\mathrm{We} \approx 40$ to 80, and it did not always occur, thus meaning the forces on the bag structures and core droplet must not be equal in all regimes. A total force approach is needed to understand the mechanisms underlying this morphology, as well as all the transitional multimode regimes.

B. Influence of We and Oh on droplet diameter

Table 3 shows the transition We between each regime, making it possible to verify a close approximation to the values presented in past works. Dai and Faeth [11] showed the multimode regime ensued between $18 < \mathrm{We} < 80$ which is, at some measure, in agreement with the results obtained for the Jet Fuel mixtures. Until this point, this regime was known to have its transition from the Bag regime at approximately We = 35. The Multimode stage still has some discrepancies in the range of We, thus the present study will follow the transition proposed by the aforementioned authors. As seen, when plotted against Oh, these values appear to fit well within the criteria proposed in the literature, with the exception of the Water experiments, Fig. 8, where green is allusive to the water experiments, black to Jet A-1 100%, blue to 75% Jet A-1 - 25% HVO and red to 50% Jet A-1 - 50% HVO. Being its diameter the same as the other mixtures, and its surface tension significantly higher, this means that there will be a need for higher flow velocities to overcome the critical Weber number, $\mathrm{We_c}$.

Table 3 Transitional Weber numbers found for each mixture in the present work.

Regime	Substance			
	Jet A-1 (100%)	Jet A-1 - HVO (75% - 25%)	Jet A-1 - HVO (50% - 50%)	H_2O
Bag	13	13	14	17
Bag-Plume	20	21	21	26
Shear-Plume	40	40	43	36
Shear	76	76	80	58

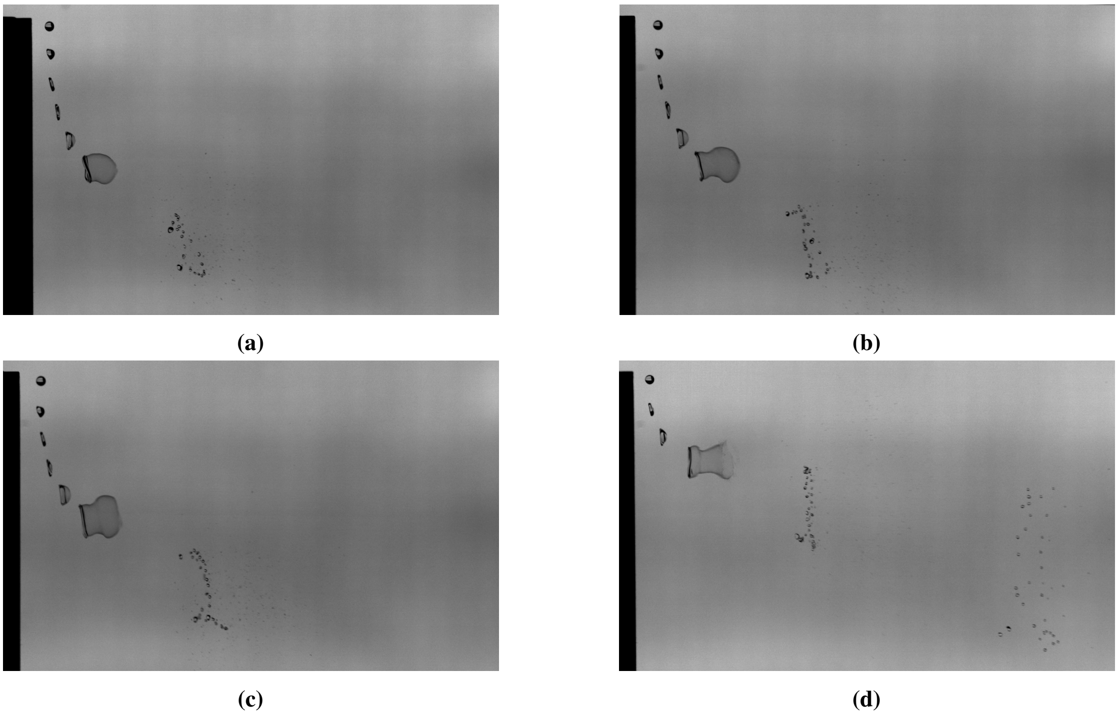

(a) (b) (c) (d)

Fig. 4 Vizualization of the Bag Breakup regime for a $D_0 \approx 3[mm]$ droplet, where: *a*) **Jet A-1** 100%; *b*) **Jet A-1** 75% **-** 25% **HVO;** *c*) **Jet A-1** 50% **-** 50% **HVO;** *d*) H_2O**.**

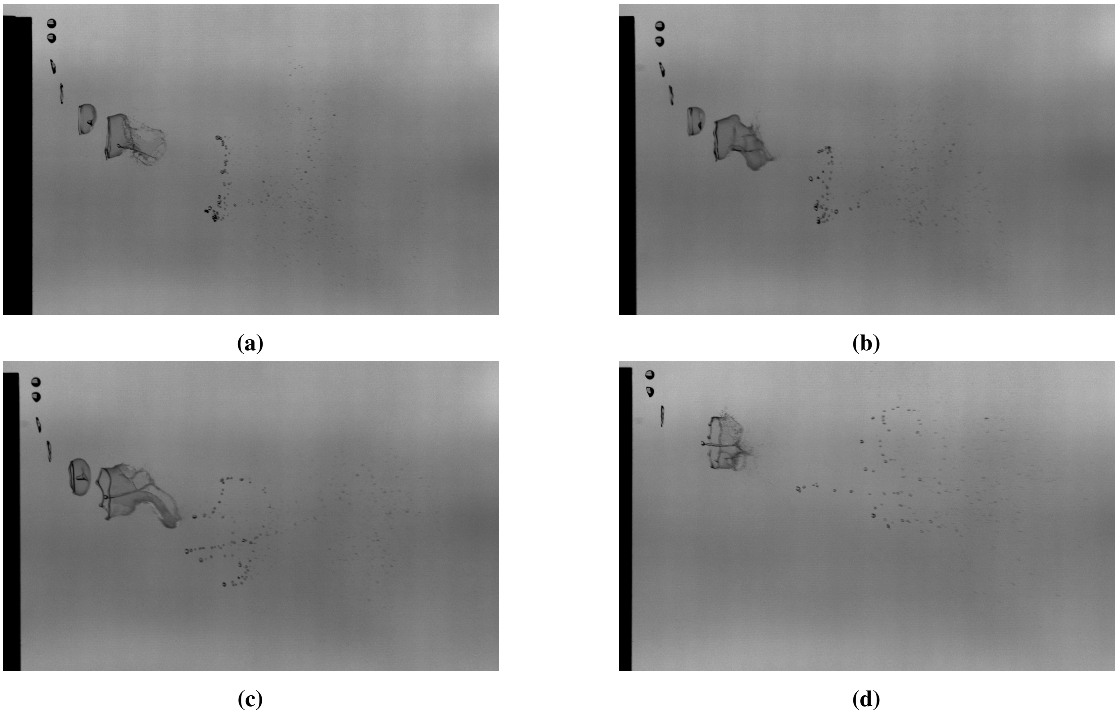

(a) (b) (c) (d)

Fig. 5 Visualization of the Bag-Plume Breakup regime for a $D_0 \approx 3[mm]$ droplet, where: *a*) **Jet A-1** 100%; *b*) **Jet A-1** 75% **-** 25% **HVO;** *c*) **Jet A-1** 50% **-** 50% **HVO;** *d*) H_2O**.**

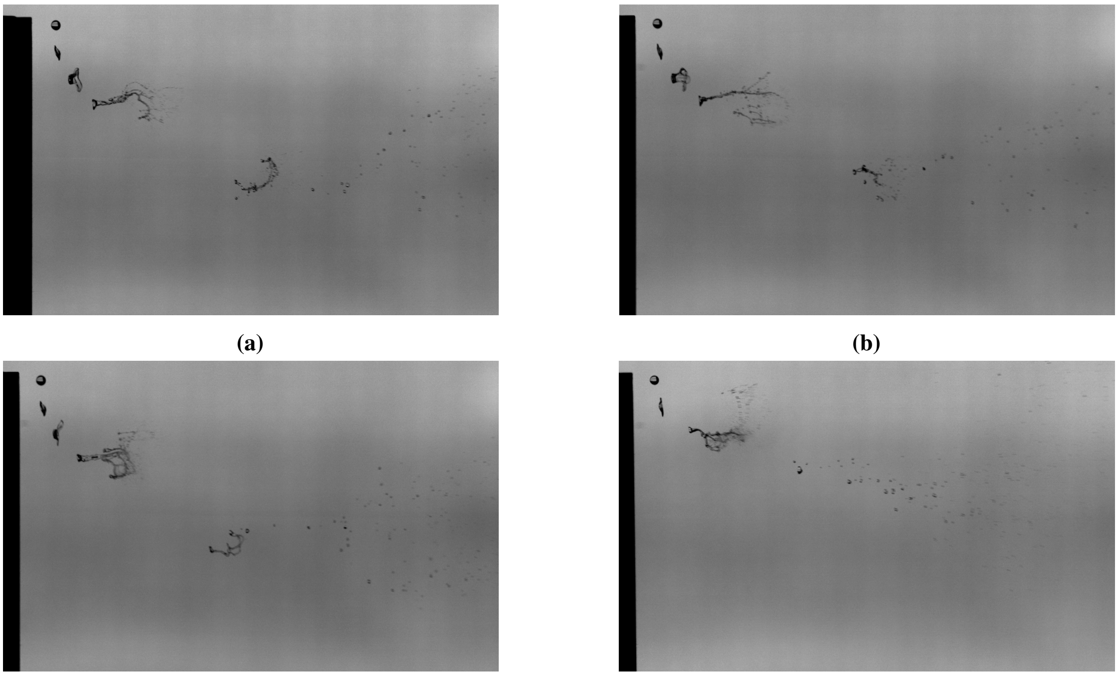

(a) (b)

(c) (d)

Fig. 6 Vizualization of the Shear-Plume Breakup regime for a $D_0 \approx 3[mm]$ droplet, where: $a)$ Jet A-1 100%; $b)$ Jet A-1 75% - 25% HVO; $c)$ Jet A-1 50% - 50% HVO; $d)$ H_2O.

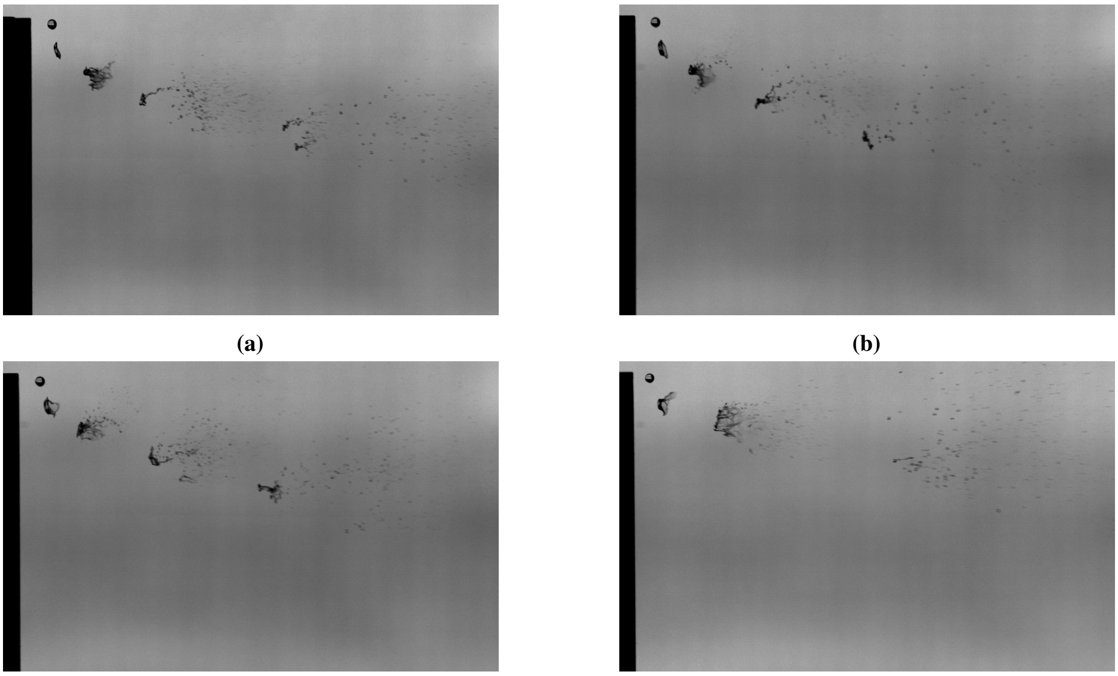

(a) (b)

(c) (d)

Fig. 7 Vizualization of the Shear Breakup regime for a $D_0 \approx 3[mm]$ droplet, where: $a)$ Jet A-1 100%; $b)$ Jet A-1 75% - 25% HVO; $c)$ Jet A-1 50% - 50% HVO; $d)$ H_2O.

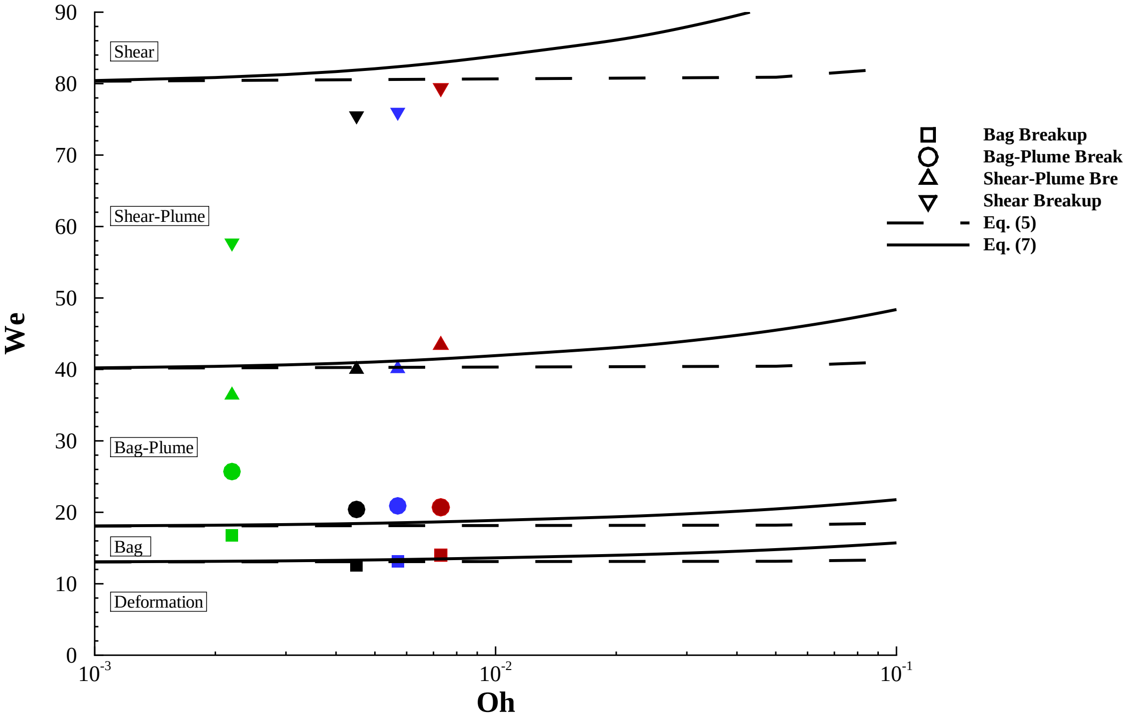

Fig. 8 Experimental data from Table 3 plotted against Eqs. (4) and (6), dashed and solid line respectively, for Oh<0.1.

The correlation between We and Oh is often plotted for the bag regime, with regard to $\mathrm{We_c}$. This is defined as the We at which the start of bag breakup regime is expected, yet for the transition between other regimes, the behavior is similar. For this, various authors proposed the correlation for the transition stages. Ref. [14] confirmed previous correlations to yield Eq. (4), whereas in Ref. [17] others are reviewed and Eq. (5) is proposed:

$$We_c = We_t(1 + 1.077Oh^{1.6}) \tag{4}$$

$$We_c = We_t(1 + 1.5Oh^{0.74}) \tag{5}$$

Similarly, the following correlation was recently proposed, Ref. [18], which is a very close approximation of Gelfand's [17] proposition for Oh < 0.1:

$$1 = \sqrt{We_t}\left(\frac{1}{We}\right)^{1/2} + 1.18\left(\frac{Oh^2}{We}\right)^{1/3} \tag{6}$$

where $\mathrm{We_t}$ is the transitional Weber number for each regime, assuming the values as Table 4. The experimental results obtained are also illustrated in Fig. 8 and compared to the curves proposed above.

Table 4 Transitional Weber number values, adapted from Ref. [11].

Regime	$\mathrm{We_t}$
Bag	13
Bag-Plume	18
Shear-Plume	40
Shear	80

Not only these parameters influence one another, but also the non-dimensional cross stream diameter, D_{max}/D_0 (Fig. 2), of the droplets at the onset of breakup. This is important because, as the drop transitions from a spherical to a disk-like shape, its drag coefficient also varies, influencing the drop deformation and breakup mechanisms. Fig. 9a illustrates the variation of D_{max}/D_0 for the different mixtures at each transitional We and compares the present experimental results with the correlations proposed by other authors [11, 12, 18].

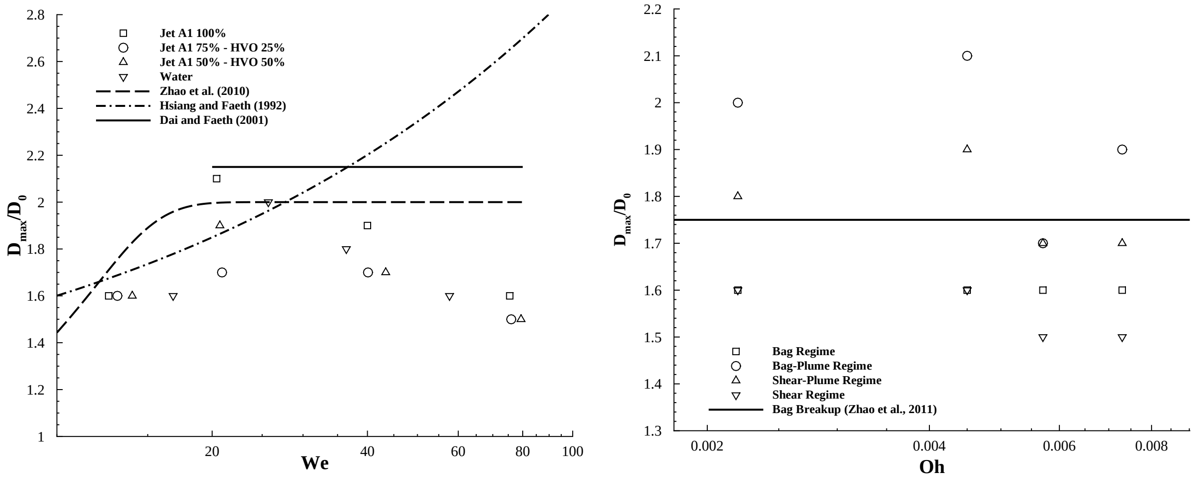

(a) **(b)**

Fig. 9 Maximum droplets' cross stream diameter due to: *a*) **We;** *b*) **Oh.**

At lower We, the experimental results seem to fit well within the curves. Since these were proposed for the bag and bag-plume regimes, it was expected to encounter some approximation with the experimental results, yet for higher, We the maximum cross stream diameter has a decaying behavior and does not fit well into the correlations. In Ref. [11] it is stated that, for $20 < We < 80$, the D_{max}/D_0 had a constant value of 2.15, which is clearly not the case of the results.

Taking into account Oh variation, Zhao et al. [18] found that D_{max}/D_0 had its variation approximately constant at 1.75 for the bag regime. As seen in Fig. 9b, for all the mixtures, the bag regime has a constant value of $D_{max}/D_0 = 1.6$, not far from the aforementioned case. Albeit, it should be of interest to individually analyze each breakup stage and consequent diameter variation, even if the results appear to fit rather well in $D_{max}/D_0 = 1.75$.

C. Influence of We and Oh on the non-dimensional characterization of time, τ

Since all the structures and regimes do not occur instantaneously, it is of importance to study the behavior of breakup initiation and total time, τ_{ini} and τ_{tot}, respectively. The first refers the time required for the droplet to demonstrate the first signs of deformation beyond the disk-like shape or demonstrate the first signs of bag formation, and the latter is the time at which all secondary atomization has ceased. Addressing regime transition criteria, Fig. 10a, the necessary time for breakup initiation appears to follow a roughly constant value, contrary to Eq. (7) that suggests a decrease in the time needed for breakup initiation, for both viscous and non-viscous droplets [14].

$$\tau = 1.9(We - 12)^{-0.25}(1 + 2.2Oh^{1.6}) \tag{7}$$

The same authors proposed the total breakup time should be described by Eq. (8), Fig. 10b. The Weber numbers present in this equation are close to those of a transition value, hinting a difference in the physics governing the breakup morphology times [7]. Although in the first two stages, the experimental values have a close behavior, with exception of the water experiments, where the shear breakup regime does not come close to the proposed equation. This case appears to demonstrate a somewhat arbitrary region, where the total breakup time depends on the size and volume of the mass stripped from the parent droplet. As these are difficult to characterize, for the present study, it was assumed that the mass stripped from the parent drop was always big enough to suffer subsequent breakup, taking more time for the overall secondary atomization to cease.

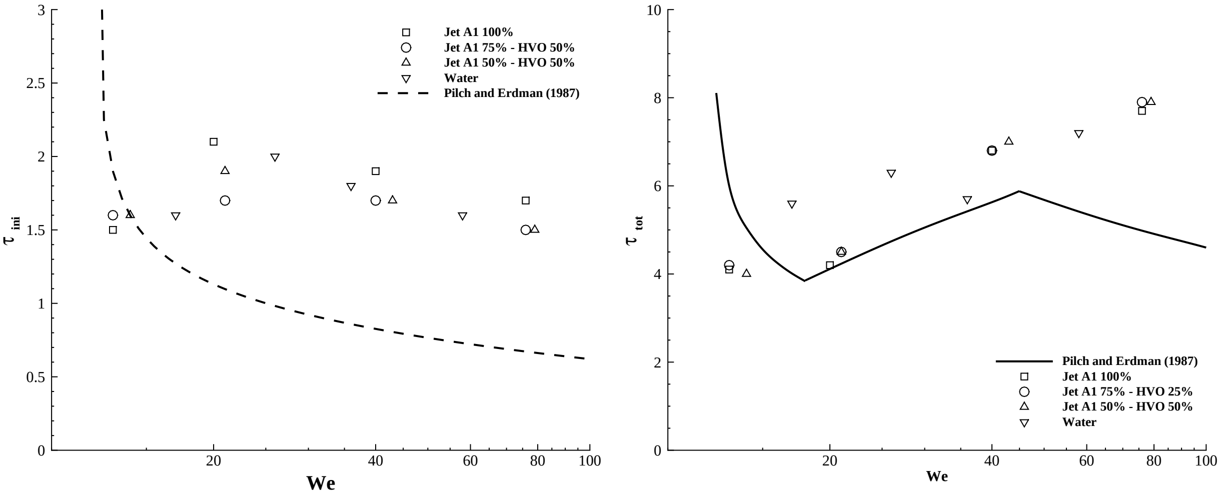

(a) **(b)**

Fig. 10 Influence of We in: *a)* τ_{ini}; *b)* τ_{tot}.

$$
\begin{aligned}
\tau &= 6(We-12)^{-0.25}, && 12 \leqslant We \leqslant 18 \\
\tau &= 2.45(We-12)^{0.25}, && 18 \leqslant We \leqslant 45 \\
\tau &= 14.1(We-12)^{-0.25}, && 45 \leqslant We \leqslant 351
\end{aligned}
\tag{8}
$$

On the other hand, the variation of time due to Oh shows some fluctuations between the mixtures. In addition to Eq. (4), other equations were considered for the initiation time and plotted in Fig. 11a. Hsiang and Faeth [12] and Gelfand et al. [17] stated the initiation time is given respectively by:

$$\tau_{ini} = \frac{1.6}{1-\left(\frac{Oh}{7}\right)} \quad We < 10^3, \quad Oh < 3.5 \tag{9}$$

$$\tau_{ini} = 1.4(1+1.5Oh^{0.74}) \quad We \approx We_c, \quad Oh < 4.0 \tag{10}$$

Figure 11a shows there is some agreement with the experimental results for the Water and Jet A-1 100% cases. For the other mixtures, the initiation time due to Oh seems to be higher, but not by a significant factor. Although, when addressing τ_{tot}, only some appear to fit well with the equations proposed by the same authors.

$$\tau_{tot} = \frac{1.6}{1-\left(\frac{Oh}{7}\right)} \quad We < 10^3, \quad Oh < 3.5 \tag{11}$$

$$\tau_{tot} = 4.5(1+1.2Oh^{0.74}) \quad We \approx We_c, \quad Oh < 0.3 \tag{12}$$

It is of importance to further expand the number of experimental results utilizing these mixtures in order to verify the existing correlations, both for We and Oh variations. However, for τ_{tot}/Oh a new study should be conducted focusing on finding the mechanisms causing total breakup time to be longer than predicted.

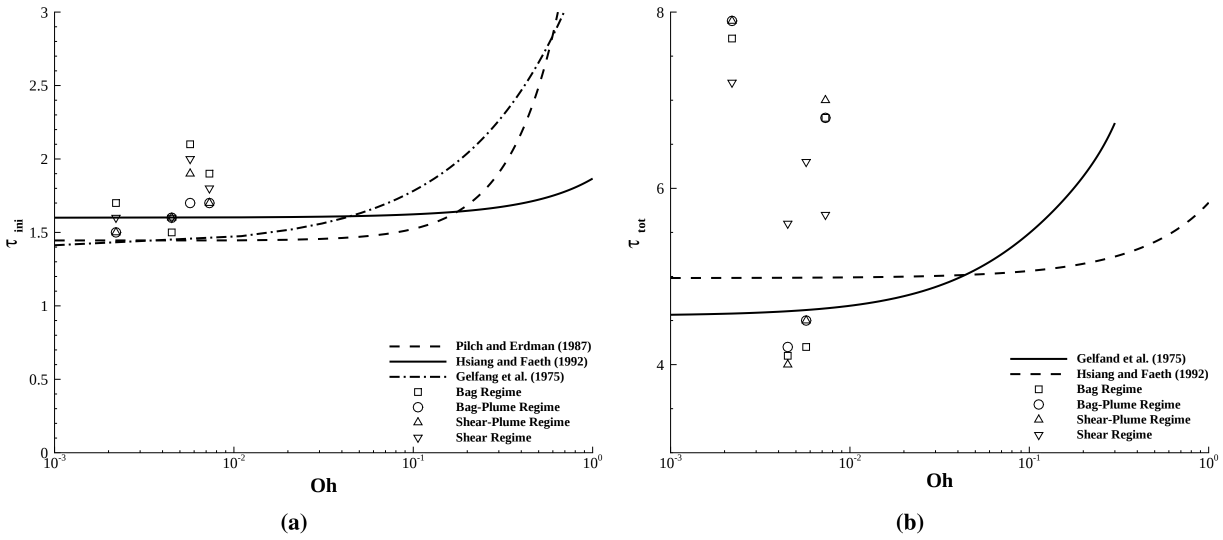

Fig. 11 Influence of Oh in: *a)* τ_{ini}; *b)* τ_{tot}.

D. Droplet diameter as a function of τ

The cross stream diameters time-wise evolution is studied until the drop reached the maximum diameter as a disk-like structure. This evolution is important because the drag coefficient changes as the droplet stretches from a sphere to a disk. As the aerodynamic loading is not constant and immediate, one should not consider the variation $\mathrm{D_{max}/D_0}$ to be linear. With this in mind, recent studies state that, for the dual-bag and bag-plume, the evolution is respectively given by [9]:

$$\begin{aligned} D_{max}/D_0 &= 1, \quad 0 < \tau < 0.3 \\ D_{max}/D_0 &= 0.59 + 1.34\tau, \quad 0.3 < \tau < 0.99 \end{aligned} \tag{13}$$

and also, Ref. [18]:

$$D_{max}/D_0 = 1 + 0.54\tau^{1.67}, \quad 0 \leqslant \tau \leqslant 1.5 \tag{14}$$

while Ref. [1] adopted a linear fit for their numerical model.

Figure 12 illustrates all the regimes and mixtures' diameter increase, and there is no clear evidence of a difference between the breakup regimes. This lead to assume that the equations mentioned above can be used for all the cases. As seen, Eq. (13) predicts a faster increase while assuming a constant value for the first instances of the two-phase interaction; Eq. (14) is a better approximation than the latter one, yet still predicts an earlier increase than that of experimental results and is unable to follow the same tendency for the intermediate stages of drop deformation. The linear equation is able to fit well to later stages of deformation, however, it agrees with neither the present experiments nor the equations. Therefore, all these results can be well expressed by Eq. (15). This expression agrees well with the experiments even in later stages of deformation as it appears to show a mean value.

$$D_{max}/D_0 = 1 + 0.3\tau^{2.35} \quad \tau < 2 \tag{15}$$

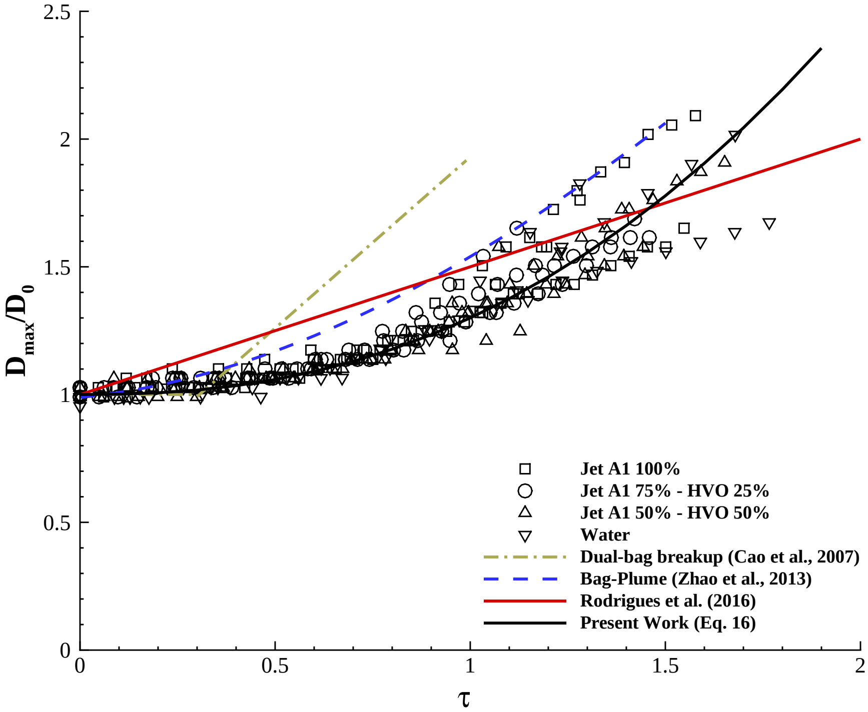

Fig. 12 Maximum cross stream diameter evolution as a function of non dimensional time.

V. Conclusion

Overall, the new mixtures enabled the visualization of the desired breakup regimes and the structures underlying each of these. Transitional We due to the variation of Oh had its values fit well with past proposed correlations, although the water experiments showed a different behavior. This has its explanation due to the physical properties since, for an even smaller drop, a substantial increase of crossflow velocity would be required to verify the first stages of the breakup phenomenon.

When taking into account the time evolution due to We and Oh, one can observe that there are still some disparities concerning the existing criteria. For the case of Fig. 10, the initiation times appear to follow a constant tendency, contrary to the decay expected from past works. Nonetheless, for the total breakup time, only the higher We regimes seem to have some different results from those expected. Though, for Fig. 11, breakup initiation fits better with the existing correlations in contrast with the total breakup times.

Finally, the cross stream diameter evolution was plotted as a function of time. There were no clear signs of different evolutions for each regime indicating the existing correlations could be used for all the breakup stages and not only individually. Furthermore, a new expression is proposed in order to well define this evolution. All the results presented in this work are of importance so that the existing numerical models can replicate the breakup phenomenon with accuracy and with a cost benefit. Since these are a new set of mixtures, it is of interest to further comprehend the mechanisms underlying the breakup of small droplets.

Acknowledgments

The present work was performed for the interinstitutional project BISI Biofuel Spray Impact in Aero-Engines under the scope of Laboratório Associado em Energia, Transportes e Aeronáutica (LAETA) activities and it was supported by Fundação para a Ciência e Tecnologia (FCT) through the project UID/EMS/50022/2013, and by Fundação Luso-Americana para o Desenvolvimento (FLAD) through the project 07/2019.

References

[1] Rodrigues, C., Barata, J., and Silva, A., "Modeling of Droplet Deformation and Breakup," *Journal of Propulsion and Power*, Vol. 32, No. 3, 2016, pp. 1–9. doi:10.2514/1.b35819.

[2] Hinze, J. O., "Fundamentals of the Hydrodynamic Mechanism of Splitting in Dispersion Processes," *A.I.Ch.E Journal*, Vol. 1, No. 3, 1955, pp. 289–295.

[3] Kim, S., Hwang, J. W., and Lee, C. S., "Experiments and modeling on droplet motion and atomization of diesel and bio-diesel fuels in a cross-flowed air stream," *International Journal of Heat and Fluid Flow*, Vol. 31, No. 4, 2010, pp. 667–679. doi:10.1016/j.ijheatfluidflow.2010.02.001, URL `http://dx.doi.org/10.1016/j.ijheatfluidflow.2010.02.001`.

[4] Bai, C., and Gosman, A., "Development of methodology for spray impingement simulation," *SAE transactions*, 1995, pp. 550–568.

[5] Chou, W. H., Hsiang, L. P., and Faeth, G. M., "Temporal properties of drop breakup in the shear breakup regime," *International Journal of Multiphase Flow*, Vol. 23, No. 4, 1997, pp. 651–669. doi:10.1016/S0301-9322(97)00006-2.

[6] Ranger, A. A., and Nichols, J. A., "Aerodynamics Shattering of Liquid Drops," *AIAA Aerospace Sciences Meeting*, , No. 68, 1968. doi:10.2514/6.1968-83.

[7] Guildenbecher, D. R., López-Rivera, C., and Sojka, P. E., "Secondary atomization," *Exp Fluids*, Vol. 46, No. 3, 2009, pp. 371–402. doi:10.1007/s00348-008-0593-2.

[8] Hsiang, L. P., and Faeth, G. M., "Drop properties after secondary breakup," *International Journal of Multiphase Flow*, Vol. 19, No. 5, 1993, pp. 721–735. doi:10.1016/0301-9322(93)90039-W.

[9] Cao, X.-k., Sun, Z.-g., Li, W.-f., Liu, H.-f., and Yu, Z.-h., "A new breakup regime of liquid drops identified in a continuous and uniform jet flow," *Physics of Fluids*, Vol. 057103, No. 2007, 2007. doi:10.1063/1.2723154.

[10] Kékesi, T., Amberg, G., and Wittberg, L. P., "Drop deformation and breakup," *International Journal of Multiphase Flow*, Vol. 66, 2014, pp. 1–10. doi:10.1016/j.ijmultiphaseflow.2014.06.006.

[11] Dai, Z., and Faeth, G. M., "Temporal properties of secondary drop breakup in the multimode breakup regime," *International Journal of Multiphase Flow*, Vol. 27, No. 2, 2001, pp. 217–236. doi:10.1016/S0301-9322(00)00015-X.

[12] Hsiang, L. P., and Faeth, G. M., "Near-limit drop deformation and secondary breakup," *International Journal of Multiphase Flow*, Vol. 18, No. 5, 1992, pp. 635–652. doi:10.1016/0301-9322(92)90036-G.

[13] Faeth, G. M., Hsiang, L. P., and Wu, P. K., "Structure and breakup properties of sprays," *International Journal of Multiphase Flow*, Vol. 21, 1995, pp. 99–127. doi:10.1016/0301-9322(95)00059-7.

[14] Pilch, M., and Erdman, C. A., "Use of breakup time data and velocity history data to predict the maximum size of stable fragments for acceleration-induced breakup of a liquid drop," *International Journal of Multiphase Flow*, Vol. 13, No. 6, 1987, pp. 741–757.

[15] Krzeczkowski, S. A., "Measurement of liquid droplet disintegration mechanisms," *International Journal of Multiphase Flow*, Vol. 6, No. 3, 1980, pp. 227–239. doi:10.1016/0301-9322(80)90013-0.

[16] Ribeiro, D. F. S., "Experimental Study of a Single Droplet Impinging upon Liquid Films : Jet Fuel and Biofuel Mixtures," Master's thesis, University of Beira Interior, 2018.

[17] Gelfand, B. E., "Droplet breakup phenomena in flows with velocity lag," *Prog. Energy Combust. Sci.*, Vol. 22, No. 3, 1996, pp. 201–265.

[18] Zhao, H., Liu, H.-f., Cao, X.-k., Li, W.-f., and Xu, J.-l., "International Journal of Multiphase Flow Breakup characteristics of liquid drops in bag regime by a continuous and uniform air jet flow," *International Journal of Multiphase Flow*, Vol. 37, No. 5, 2011, pp. 530–534. doi:10.1016/j.ijmultiphaseflow.2010.12.006, URL `http://dx.doi.org/10.1016/j.ijmultiphaseflow.2010.12.006`.